McMaster University

Doctoral Thesis

# An Optical System towards In-line Monitoring of Bacteria in Drinking Water

*Author:*
Tianyi Guo

*Supervisor:*
Dr. M. Jamal Deen

*A thesis submitted in fulfilment of the requirements*
*for the degree of Doctor of Philosophy*
*in the*

School of Biomedical Engineering

June 2016

# *Abstract*

The prevention of waterborne diseases requires rapid detection of pathogens in drinking water, with an ultimate goal of in-line monitoring in real time. Standard cultivation-based methods are too time-consuming and thus not suitable for this purpose. Many technologies were proposed to achieve this goal, such as ELISA, PCR, FISH, FTIR and flow cytometry. However, they still have limitations of non-specificity, complexity and high cost. Therefore, an optical system is proposed and developed towards the in-line monitoring of bacteria, which combines the advantages of FTIR and micro-flow cytometer for bacterial identification and precise quantification.

The in-line use requires obtaining IR spectra of bacterial cells directly in water, which is achieved using a $CaF_2$ liquid cell. The spectra of a series of bacterial samples are collected and analyzed using principal component analysis for their differentiation. A preliminary study on fabricating a $CaF_2$ concentrator is conducted, in which a novel phenomenon on stress release of silicon nitride film on $CaF_2$ substrate is discovered and studied.

To determine the concentration of bacteria in drinking water, a micro-flow cytometer is built based on a micro-fabricated device that integrates on-chip beam-shaping optics and microfluidic channels. With this micro-flow cytometer and optimized data analysis for counting particles in real time, linearity with correlation coefficient of over 0.99 is achieved for the dependences of throughput on both volumetric flow rate and concentration of sample. With a one-dimensional hydrodynamic focusing, no degradation of the counting efficiency is demonstrated when the focused sample stream expands. The high accuracy of counting makes this micro-flow cytometer a promising candidate for low concentration applications.

Counting of E. coli DH5$\alpha$ cell suspensions in phosphate buffered saline is performed using the micro-flow cytometer. Side-scattered light signals are used to count the E. coli cells. A detection efficiency of 92% is achieved when compared with the expected count from a haemocytometer. It is demonstrated that E. coli can be easily distinguished from beads of similar sizes (2–4$\mu$m) as their scattering intensities are different.

# *Acknowledgements*

I would like to thank my supervisor, Dr. M. Jamal Deen and co-supervisor, Dr. Changqing Xu, for the support and guidance. I have learned a lot from both of you during the course of this work. Your deep wisdom and broad vision benefit me not only on my academic knowledge but more on my personality that will last for all my life.

I would also like to thank Dr. Qiyin Fang, Dr. P. Ravi Selvaganapathy, Dr. Haiying Zhang, Dr. Zhiyun Li, Dr. Darek Palubiak, Dr. Yin Wei, Cong Feng, Hani B. Alhemsi, Zeng Cheng, Xiaoqing Zheng who all engaged me in constructive discussions and provided help wherever necessary during the course of this work.

I would also like to thank Dr. Tom Edge for providing bacterial samples and Dr. Martin W. Gerber for support and help on the use of the FTIR spectrometer.

I extend my deepest thanks to Dr. Benjamin R. Watts for being an amazing friend and teacher of fabrication techniques.

Finally, to my family - who have always strongly supported me on all the aspects of my life - thank you.

# Contents

# List of Figures

# List of Tables

# Abbreviations

| | |
|---|---|
| **AFM** | **A**tomic **F**orce **M**icroscopy |
| **ATR** | **A**ttenuated **T**otal **R**eflectance |
| **CFU** | **C**olony-**F**orming **U**nit |
| **CV** | **C**oefficient of **V**ariation |
| **CVA** | **C**anonical **V**ariate **A**nalysis |
| **CW** | **C**ontinuous **W**ave |
| **DNA** | **D**eoxyribo**N**ucleic **A**cid |
| **DI** | **De**ionized |
| **DPSS** | **D**iode-**P**umped **S**olid-**S**tate |
| **ECA** | **E**nterobacterial **C**ommon **A**ntigen |
| **E. coli** | **E**scherichia **coli** |
| **ELISA** | **E**nzyme-**L**inked **I**mmuno**S**orbent **A**ssay |
| **FA** | **F**actor **A**nalysis |
| **FISH** | **F**luorescence **I**n-**S**itu **H**ybridization |
| **FITC** | **F**luorescein-**I**so**T**hio**C**yanate |
| **FR** | **F**low **R**ate |
| **FSC** | **F**orward **SC**attered |
| **FTIR** | **F**ourier **T**ransform **I**nfra-**R**ed |
| **IFA** | **I**mmuno**F**luorescence **A**ssay |
| **IR** | **I**nfra**R**ed |
| **MEMS** | **M**icro-**E**lectro-**M**echanical **S**ystems |

| | |
|---|---|
| **MF** | **M**embrane **F**ilter |
| **MFC** | **M**icro-**F**low **C**ytometer |
| **MIR** | **M**iddle **I**nfra-**R**ed |
| **MOEMS** | **M**icro-**O**pto-**E**lectro-**M**echanical **S**ystems |
| **MPN** | **M**ost **P**robable **N**umber |
| **MTF** | **M**ultiple-**T**ube **F**ermentation |
| **NABSA-PCR** | **N**ucleic **A**cid **B**ased **S**equence **A**mplification **PCR** |
| **OD** | **O**ptical **D**ensity |
| **OPD** | **O**ptical **P**ath **D**ifference |
| **PBS** | **P**hosphate-**B**uffered **S**aline |
| **PCA** | **P**rinciple **C**omponent **A**nalysis |
| **PCR** | **P**olymerase **C**hain **R**eaction |
| **PDMS** | **P**oly**D**i**M**ethyl**S**iloxane |
| **PEB** | **P**ost-**E**xposure **B**ake |
| **PECVD** | **P**lasma-**E**nhanced **C**hemical **V**apor **D**eposition |
| **PI** | **P**ropidium **I**odide |
| **PL** | **P**hoto-**L**ithographic |
| **PMA-rtPCR** | **P**ropidium **M**ono**A**zide **rtPCR** |
| **PMT** | **P**hoto **M**ultiplying **T**ube |
| **PPLN** | **P**eriodically **P**oled **L**ithium **N**iobate |
| **RNA** | **R**ibo**N**ucleic **A**cid |
| **rRNA** | **r**ibosomal **RNA** |
| **rtPCR** | **r**eal-**t**ime **PCR** |
| **RT-PCR** | **R**everse **T**ranscriptase **PCR** |
| **SEM** | **S**canning **E**lectron **M**icroscope |
| **SIMCA** | **S**oft **I**ndependent **M**odeling of **C**lass **A**nalogy |
| **SNR** | **S**ignal-to-**N**oise **R**atio |
| **SSC** | **S**ide-**SC**attered |

| | |
|---|---|
| **TSB** | **T**ryptic **S**oy **B**roth |
| **UV** | **U**ltra**V**iolet |
| **WHO** | **W**orld **H**ealth **O**rganization |
| **XPS** | **X**-ray **P**hotoelectron **S**pectroscopy |
| **XRD** | **X**-**R**ay **D**iffraction |

# Chapter 1

# Introduction

This research focuses on development of an in-line system to monitor the microbial quality of drinking water using a combination of Fourier transform infrared spectroscopy and micro-flow cytometry to determine the bacterial species and concentrations.

## 1.1 Motivation

### 1.1.1 Risk of waterborne disease

Safe drinking water is significantly important for both human health and economic development. The quality of drinking water includes four major aspects, microbial, chemical, radiological, and acceptability. The microbial quality attracts unique attention from people because waterborne pathogens can be transmitted through the water distribution network and potentially lead to large-scale disease outbreaks if the water supply is contaminated by pathogenic microorganisms.

There were many reports on the outbreaks of waterborne disease. For example, one of the largest outbreak of acute watery diarrhea occurred in 1993 in Milwaukee, Wisconsin, USA, affecting approximately 400,000 people, due to the contamination of public water supply by Cryptospordium[1]. Another outbreak of waterborne illness occurred in 2000 in Walkerton, Ontario, Canada, and resulted in 7 deaths and more than 2,300 illness, which was caused by the contamination of drinking water supply by E. coli O157:H7 and Campylobacter jejuni from cattle excreta[2].

In a macroscopic view, the total number of waterborne illnesses per year in the US has been estimated at 19.5 million, including 5.4 million from municipal groundwater, 1.1 million from noncommunity groundwater and 13 million from surface water supplies[3]. Moreover, Liu et al. analyzed the global causes of child mortality from

2000 to 2010 and found that diarrhea caused 0.801 million deaths (10.5% of total deaths) in 2010, ranking as the third cause of death behind pneumonia and preterm birth complication[4]. Most of the diarrhoea were caused by diseases transmitted through unsafe water[5].

Beside the health issues, the outbreaks of waterborne diseases also lead to tremendous economic losses. For example, the outbreak of Milwaukee resulted in direct medical costs of $31.7 million and indirect productivity losses of $64.6 million, $96.2 million in total[6]. Overall, the lost productivity due to waterborne diseases was estimated to be $20 billion per year in the US[7].

In general, microbial safety of drinking water supplies remains the primary concern in both developed and developing counties according to the World Health Organization (WHO)[8].

### 1.1.2 Indicators of microbial quality

It is not practical to routinely characterize the microbial quality of drinking water by targeting all potentially waterborne pathogens including pathogenic bacteria, viruses, protozoa and helminths because there are many types of pathogens and it will be too time-consuming and labor-intensive to test all of them[8]. A more practical method is to define some pathogens as indicators that can reflect the microbial index of drinking water. Because the most common sources of these pathogens are feces from humans or animals, the total coliform bacteria and thermotolerant coliforms or E. coli are selected as the indicators although they are mostly non-pathogenic to humans except for some enterohaemorrhagic serotypes of E. coli such as O157:H7[9, 10].

Drinking water is not a natural water environment such as raw water where high concentrations of various coliforms can be found because of the discharging of treated wastewater and excretion of animals such as birds. The presence of coliform bacteria in drinking water means the potential existence of other pathogens probably due to intrusion of contaminated water into the water supplies or ineffectiveness of treatment because most coliforms are less resistive to disinfection than viruses or protozoa. Therefore, coliforms are used as the indicators of the microbial quality of drinking water.

### 1.1.3 Coliform regulations

The government of many countries issued strict regulation on the microbial quality of drinking water based on the guidelines for drinking water quality from WHO[8]. Some regulations in developed countries and one in developing country are listed in Table 1.1.

TABLE 1.1: Some regulations on the microbial quality of drinking water.

| Organization | Total bacterial count (CFU/mL) | Total coliforms (MPN/100mL or CFU/100mL) | E. coli (MPN/100mL or CFU/100mL) |
|---|---|---|---|
| WHO | - | 0 (95%) | 0 (100%) |
| US | - | 0 (95%)[a] | 0 (100%) |
| EU | - | 0 (95%) | 0 (100%) |
| Canada | - | 0 (90%)[a,b] | 0 (100%) |
| China | 100 | 0 (95%)[c] | 0 (100%) |

CFU: colony-forming unit; MPN: most probable number

WHO: World Health Organization; US: United States; EU: European Union

[a] A consecutive sample from the same site must be coliform-free.

[b] None should contain more than 10CFU/100mL.

[c] When coliform bacteria are present, further tests on E.coli or thermotolerant coliforms must be performed; when coliform bacteria are absent, no need to test E. coli or thermotolerant coliforms.

## 1.2 Standard methods

The standard methods for the examination of water and wastewater issued by different governments are similar. Thus, the standard methods of the U.S. are selected as the reference. According to the latest edition issued in 2012, the standard methods for coliform test include multiple-tube fermentation (MTF), membrane filter (MF) and enzyme substrate techniques[11].

### 1.2.1 Multiple-tube fermentation technique

The definition of coliform bacteria differs on the methods used for detection. When fermentation technique is used, the coliform group is defined as all facultative anaerobic, gram-negative, non-spore-forming, rod-shaped bacteria that ferment lactose with gas and acid formation within 48 hours at 35℃[11]. MTF technique performs fermentation tests on water samples in a series of tenfold dilutions. Its procedure includes presumptive, confirmed and completed phases. The detection of total coliform using MTF technique is outlined in Figure 1.1. The time required for each phase is 24-48, 48 and over 48 hours, respectively. The detection of thermotolerant coliform or E. coli using MTF technique is similar to that of total coliform, despite using different culture media and incubation temperature.

The MTF technique measures the number of bacteria in the unit of the most probable number (MPN), which is the statistical mean of the number of bacteria. Therefore, MTF technique can only provide a semi-quantitative enumeration of bacteria with a low precision. The enhancement of precision requires increasing the number of tubes used for the analysis, which means higher cost. Due to the low precision and long time, the MTF technique has been replaced by MF technique in many circumstances such as testing drinking water samples. However, MTF is irreplaceable when MF technique is not applicable such as for water samples of high turbidity or having large numbers of noncoliform bacteria[9].

### 1.2.2 Membrane filter technique

When the MF technique is used, the coliform group is defined as facultative anaerobic, gram-negative, non-spore-forming, rod-shaped bacteria that develop colonies with distinctive characteristics on specific media[11]. For example, typical coliform colonies on m-Endo-type agar medium have a dark-red color with a metallic surface sheen, while atypical ones are pink, dark-red, mucoid or nucleated without sheen.

The MF technique utilizes a sterile filter of 0.45$\mu$m pore size to retain bacteria. After the filtration process, the filter membrane is placed onto a selective medium to incubate the bacteria. The typical colonies formed on the membrane surface are counted and its number is divided by the volume of sample water filtered, yielding the corresponding bacterial concentration. However, the MF technique is not

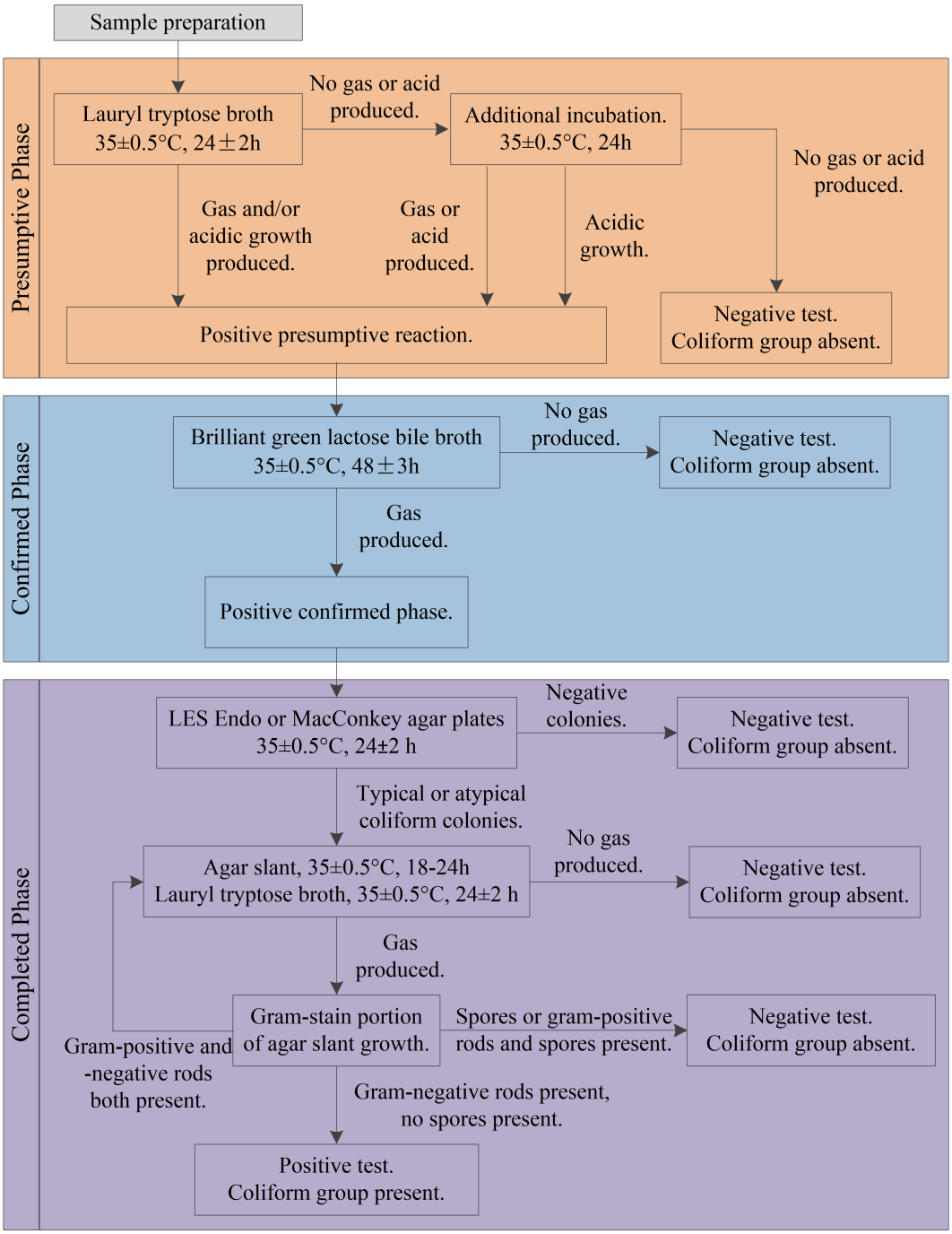


FIGURE 1.1: Schematic digram of presumptive, confirmed and completed phases for the total coliform detection using multiple-tube fermentation technique.

completely specific, because occasionally, typical sheen colonies may be produced by noncoliform bacteria and atypical may be coliforms. Therefore, a verification test should be performed on the developed colonies. As an example, take its application on total coliform. In this case, the filter is incubated for 22-24 hours at 35±0.5℃, followed by a coliform verification using lactose fermentation that needs another incubation at 35±0.5℃ for up to 48 hours, or by test reactions for cytochrome oxidase and $\beta$-galactosidase that only need 4 hours[11].

Generally, the MF technique is simpler and faster than the MTF technique. It is used in many instances of systematic examinations of drinking water that is of low turbidity and with little interferences from noncoliform bacteria.

### 1.2.3 Enzyme substrate technique

The enzyme substrate technique detects coliform bacteria by the enzymes they possess, $\beta$-D-galactosidase and $\beta$-glucuronidase. The former is common for all coliforms and the latter is specific for E. coli. Using chromogenic and fluorogenic substrates, the total coliforms and E. coli can be detected simultaneously by viewing the color change and fluorescence, as summarized in Table 1.2. The test procedure of this technique takes up to 48 hours[11].

Table 1.2: Characteristics of enzyme substrate technique for simultaneous detection of total coliforms and E. coli.

| | Total coliforms | | E. coli |
|---|---|---|---|
| Enzyme | $\beta$-D-galactosidase | | $\beta$-D-galactosidase and $\beta$-glucuronidase |
| substrate | ONPG | CPRG | MUG |
| substrate type | Chromogenic | | Fluorogenic |
| Positive | Yellow | Red or magenta | Blue fluorescence |

ONPG: ortho-nitrophenyl-$\beta$-D-galactopyranoside

CPRG: chlorophenol red-$\beta$-D-galactopyranoside

MUG: 4-methylumbelliferyl-$\beta$-D-glucuronide

## 1.3 Emerging methods

Although standard methods such as the MTF and MF can provide reliable results on the presence/absence and/or concentration of the indicator bacteria, they takes at least 2 days for the tests, which limits their uses in the prevention of waterborne disease. Therefore, many methods have emerged to realize the rapid detection and enumeration of coliform bacteria in drinking water, including immunological, polymerase chain reaction (PCR)-based, fluorescence in-situ hybridization (FISH), Fourier transform infrared (FTIR) spectroscopic and flow cytometric methods. These methods are now described.

### 1.3.1 Immunological methods

The principle of immunological methods relies on the specific binding of antibodies to antigens. An antibody is a large, Y-shaped protein produced in an immune response to pathogens such as viruses and bacteria, which are considered as "foreign" substances to the host. An antibody recognizes a specific molecule of the substance, which is called an antigen. For example, the enterobacterial common antigen (ECA) is a lipopolysaccharide linked within the outer membrane of the bacteria in the family Enterobacteriaceae[12].

There are two types of antibodies, polyclonal and monoclonal. The former are secreted by different B cell lineages of the host and thus are a mixture of immunoglobulins, each targeting a different epitope, while the latter are produced by a single cell lineage and possess monovalent affinity to the same epitope[13]. Generally, the monoclonal antibodies are more specific to the target microorganism than the polyclonal ones, and thus are recommended for the detections. With appropriate selection of the targeting antigens, immunological methods allow for detection of microorganisms at family, genus, species or serotype levels.

The antigen-antibody reaction can be visualized by several techniques, such as enzyme-linked immunosorbent assay (ELISA)[14], and immunofluorescence assay (IFA)[15, 16]. The ELISA technique utilizes enzyme-linked antibodies to bind to the antigens of the target microorganisms and then employs the color formation of the enzyme-substrate reaction as the positive result of the test. For example, targeting the ECA

by a monoclonal antibody, the members of the family Enterobacteriaceae were tested using a sandwich ELISA and 98% of the results of testing 688 water samples by this immunological method were confirmed by conventional microbiological methods. However, in this example, ELISA took about 24 hours because the detection limit of ELISA was $10^5$ cells/mL and thus a pre-enrichment culture was still needed[14].

The IFA technique allows for detection and identification of the target microorganisms at a single-cell level because fluorochrome-conjugated antibodies are used to label the targets, which are subsequently observed under a epifluorescence microscope. Zaccone et al. performed a 4-year survey on the fecal pollution in coastal waters using the IFA, which utilized fluorescein-isothiocyanate (FITC)-conjugated antibodies of enteropathogenic strains of E. coli, demonstrating high-specificity detection with a lower limit of 1 cell/mL[15]. Furthermore, to solve the problem of IFA on non-specificity between live and dead cells, Caruso et al. modified this IFA procedure by performing an additional labeling with propidium iodide (PI) that only penetrates cells with damaged membranes and demonstrated the distinction of dead cells within the total enteropathogenic E. coli population[16].

Compared with conventional cultivation-based methods for bacterial detection, the immunological methods are more rapid and simpler, but their accuracy relies mainly on the specificity of the antibody used[17]. Although monoclonal antibodies posses higher specificity than polyclonal ones, they still have the problem of cross-reactivity with other bacterial strains because an epitope can be present in more than one antigenic agent[9]. Therefore, more investigations are needed on application of immunological methods for the detection of bacteria in drinking water.

### 1.3.2 PCR-based methods

PCR replicates a specific DNA fragment of the target microorganism by thermal cycling, which results in exponential amplification of the DNA fragment. For example, about 1 million copies can be produced after 20 cycles. Due to this high amplification, PCR-based methods allow for highly sensitive detection of bacteria, even down to the single cell level. In addition, the DNA fragment to be replicated can be selected using oligonucleotide primer sets, such as lacZ[18–21] and uidA[19, 20, 22, 23] genes that encode for the enzymes $\beta$-galactosidase and $\beta$-D-glucuronidase, respectively.

In addition to its high sensitivity and specificity, the PCR procedure is also faster than conventional methods based on cultivation. Therefore, the PCR-based methods have attracted extensive researches for various applications, which have been well reviewed recently[9, 24, 25]. Several variations of standard PCR have been developed, including real-time PCR (rtPCR), reverse transcriptase PCR (RT-PCR), nucleic acid based sequence amplification PCR (NABSA-PCR) and propidium monoazide rtPCR (PMA-rtPCR). The rtPCR utilizes fluorescence to monitor the amplification in each cycle to realize detection in real time. RT-PCR amplifies the DNA fragment that is first transcribed from a target messenger RNA, and NABSA-PCR enables selective amplification of a RNA fragment without interference for background DNA. PMA-PCR uses a cell membrane-impermeable dye to distinguish viable from dead cells. The main advantages and limitations of these PCR-based methods are summarized in Table 1.3. Because of these limitations, the use of PCR-based methods is not mature enough for use in monitoring bacteria in drinking water. Therefore, more research efforts should be continued[25].

### 1.3.3 FISH-based methods

The FISH-based methods detect and identify the target microorganism using fluorochrome linked oligonucleotide probes that are built from and complementary to the DNA or RNA sequences of the target[33]. Generally, a FISH procedure includes 4 steps: 1) cell fixation; 2) application of gene probes and incubation for hybridization; 3) washing to remove unbound probes; 4) fluorescence detection by epifluorescence microscopy or flow/solid-phase cytometry.

The specificity of FISH relies on the selected nucleic acids sequences that the probes match and the sensitivity depends on the number of target molecules and the brightness of the fluorochrome used. Because ribosomal RNA (rRNA) sequences were used for the phylogenetic classification of microorganisms, rRNA probes had been well developed at different levels from domain to subspecies[34]. In addition, the fluorescence intensity is proportional to the number of fluorescent probes bonded to the target molecules. The large number of ribosomes per cell ($10^3 - 10^5$ per cell[34]) allows for hybridization of abundant probes in one cell, generating high intensity fluorescence that eases the optical detection.

TABLE 1.3: Summary of the main advantages and limitations observed in PCR-based methods for microbiological water quality monitoring[24, 26–32]. (Reprinted from Reference 25 with permission from Elsevier.)

| Method | Advantages | Limitations |
|---|---|---|
| Standard PCR | - Higher sensitivity and specificity when compared to culture-based methods<br>- Possibility of multiplex-PCR for multiple pathogen detection<br>- Detects viable but non-culturable cells<br>- Simultaneous detection of different targets within the same species is possible (multiplex-PCR) | - Post-PCR confirmation step needed (electrophoresis)<br>- Non-quantitative<br>- No distinction between viable and dead cells (detects both)<br>- Inhibition of the amplification when environmental samples are analyzed due to the presence of contaminants (e.g. organic, inorganic and biomass content)<br>- Low nucleic acid concentration causes frequent variability on the results, which leads to tube-to-tube variability |
| RT-PCR | - Distinguishes viable from dead cells | - Complexity of the procedures<br>- Short half-life of RNA<br>- Technical expertize is necessary<br>- Environmental samples can inhibit the detection |
| rtPCR | - Faster than conventional PCR<br>- High level of sensitivity and specificity<br>- Real-time detection<br>- Quantification of the target in the sample is possible (qrtPCR) | - Inhibition of the amplification when environmental samples are analyzed due to the presence of contaminants<br>- No distinction between viable and dead cells (detects both) |
| NASBA-rtPCR | - Distinguish viable from dead cells<br>- No interference from background DNA | - The same as in RT-PCR |
| PMA-rtPCR | - Distinguish viable from dead cells and from free DNA<br>- Simple to perform | - Possible inhibition from high solid content samples (further research is required)<br>- Use of an extremely toxic compound (e.g. propidium monoazide) |

For the application of FISH to detect coliform bacteria and E. coli, several oligonucleotide probes were used. These probes are listed in Table 1.4. Because the total coliforms defined by regulations include bacteria in phylogenetically different genera, but microorganisms classified by the rRNA sequences are based on the phylogenetic relationship, it is impossible to use one probe to detect the total coliforms and thus the probes are designed to target bacteria in the Enterobacteriaceae family[9].

TABLE 1.4: Oligonucleotide probes used for identification of Enterobacteriaceae and E. coli in the environment. (Adapted from Reference 9 with permission from Elsevier.)

| Probe | Probe sequence (5'-3') | rRNA target position | Specificity | Ref. |
|---|---|---|---|---|
| ENTERO | CATGAATCACAA AGTGGTAAGCGCC | 16S, 1458-1482 | Enterobacteriaceae | 35 |
| ENT1 | CCGCTTGCTCTC GCGAG | 16S, 1273-1289 | Enterobacteriaceae | 36 |
| EC1531 | CACCGTAGTGCT CGTCATCA | 23S, 1531-1550 | E. coli | 37 |
| COLINSITU | GAGACTCAAGAT TGCCAGTATCAG | 16S, 637-660 | E. coli | 38, 39 |
| ECOLI | GCAAAGGTATTA ACTTTACTCCC | 16S, 453-475 | E. coli | 39–41 |
| PNA probe | GCAAAGCAGCAA GCTC | 16S, 71-86 | E. coli | 42 |

Although FISH can provide high specificity at a cellular level, it still has some limitations for the bacterial monitoring in drinking water, where the low nutrient environment makes bacterial cells suffer from starvation. In addition, the number of rRNA content of the bacterial cells is positively related to the growth rate[34], which is limited under starvation conditions. Therefore, the number of rRNA targets of bacterial cells in drinking water is small, resulting in weak fluorescence signals.

Several techniques were used to enhance the FISH fluorescence intensity for starved cells. Lebaron et al. used a tyramide signal amplification system with biotinylated

oligonucleotide probes and streptavidin-horseradish peroxidase and achieved a 7- to 12-fold amplification of the fluorescence signal[43]. Baudart and Lebaron utilized rRNA helper sequences to enhance the fluorescence intensity of the detection of E.coli using the ECOLI and COLINSITU probes[39]. The helper sequences are gene fragment adjacent to the probes, which are not labeled with fluorochromes. The fluorescence signal was too weak to be detected when the E. coli cells were labeled by the COLINSITU probes without the helper, but it was enhanced to be sufficient for detection by solid-phase cytometry after the helper was applied. In addition, the fluorescence intensity was doubled for the ECOLI probe when its helper is applied.

### 1.3.4 FTIR spectroscopic method

The infrared spectra of microorganisms have specific fingerprints that can be used to detect, differentiate and identify the microorganism[44]. In the early years of FTIR before 1980, the IR spectra of microorganisms were measured using dispersive spectrometers. However, its weak performance limited the use of IR spectroscopy in the analyses of microorganisms[45–50]. Then, with the advancement of modern computer and fast Fourier transformation, interferometric spectrometers emerged as a powerful tool for rapid detection and analysis of microorganisms because they can obtain the spectrum of a sample in seconds, which is much faster than with dispersive spectrometers[51–53].

A typical FTIR spectrum from a sample of bacterial cells is shown in Figure 1.2, including 5 spectral windows ($w_1$ to $w_5$) relating to the biological and chemical properties of bacterial cells, as summarized in Table 1.5[53]. These spectral windows are also used for differentiation and identification of the microorganism.

There are three main methods to obtain the IR spectrum of a bacterial cells sample using a FTIR spectrometer. They are transmission, diffuse reflectance and attenuated total reflectance (ATR).

The transmission method utilizes IR-transparent materials to obtain the IR spectra of samples. The bacterial cells are either placed onto a IR-transparent substrate such as a zinc selenide (ZnSe) crystal or mixed with potassium bromide (KBr) powder. The cells on the substrate are then dried naturally or with laminar flow of air, forming

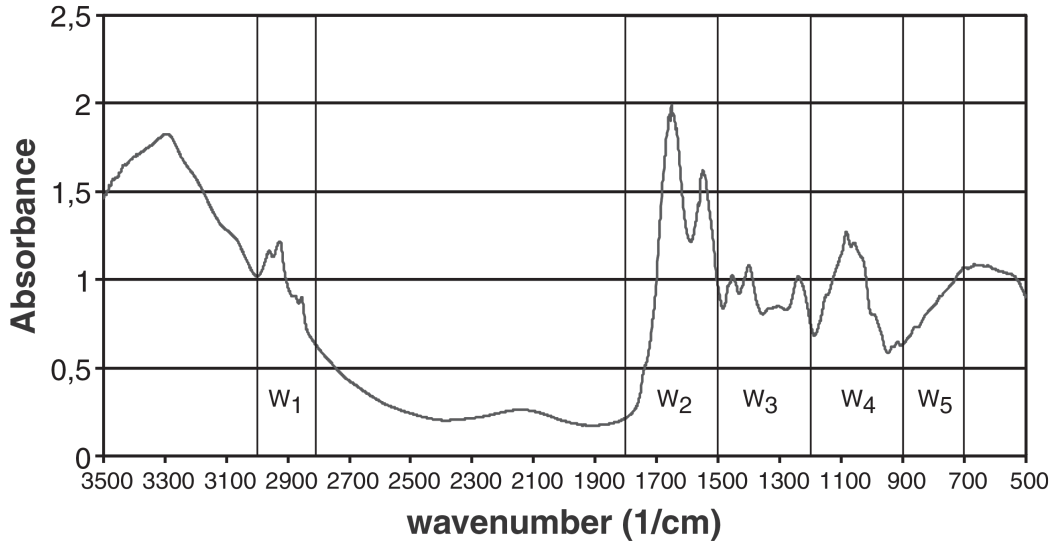


FIGURE 1.2: Representative FTIR spectrum (3500 to 500$cm^{-1}$) from a bacterial cells sample. Reprinted from Reference [53] with permission from Elsevier.

TABLE 1.5: Assignment of the five windows in microbial IR spectra[53].

| Spectral window ($cm^{-1}$) | Corresponding vibration modes |
|---|---|
| w1 (3000-2800) | C-H stretching vibrations of CH, $CH_2$ and $CH_3$ in the functional groups of membrane fatty acids and of amino acid side-chains |
| w2 (1800-1500) | C=O stretching vibrations of amides linked to proteins<br>N-H deformation of amides linked to proteins<br>>C=O stretching vibrations of the ester groups in lipids;<br>>C=O, >C=N, >C=C< stretching of the DNA or RNA bases |
| w3 (1500-1200) | $>CH_2$ and $-CH_3$ bending modes |
| w4 (1200-900) | symmetric stretching vibration of $PO_2^-$ groups in nucleic acids<br>C-O-C and C-O-P stretching of carbohydrates and polysaccharides in the cell wall |
| w5 (900-700) | aromatic ring vibrations of aromatic aminoacids |

a relatively homogeneous film. The mixture of cells and KBr powder is compressed into a disc with a diameter of about 1 cm and a thickness of 3-5 mm for the FTIR transmission measurement.

The diffuse reflection method measures the light signal scattered from the sample; thus it does not require the use of IR-transparent materials and manipulation of the sample. For example, it is difficult to remove the bacterial cells on a filtration membrane and transfer them to an IR-transparent substrate if the transmission FTIR method is adopted. However, the diffuse reflectance spectrum is determined not only by the absorbance of the sample but also by the reflectance features that relates to the scattering cross-sections of the sample, which increases the complexity of spectral analysis. This is the reason why diffuse reflection FTIR is rarely adopted for measuring the IR spectra of cells. In Table 1.6, a summary of the use of FTIR for bacterial studies in recent years indicates that transmission and ATR methods are mostly adopted, and diffuse reflection method is rarely used.

The FTIR-ATR utilizes a totally reflecting IR beam inside an IR-transparent crystal with higher refractive index than its surroundings to achieve interactions between the IR light and the sample at multiple locations. Here, evanescent fields exist at the interface between the crystal and the sample and a portion of IR light energy is absorbed by the sample. The number of absorption locations is determined by the length-to-height ratio and the absorption coefficient of the crystal. As seen in Table 1.6, the ATR method is preferred by many researchers because it simplifies the sample preparation steps. For example, bacterial cells retained on the surface of the filtration membrane can be directly placed against onto the surface of the ATR crystal for the spectral measurement[54, 55].

Another key feature of the ATR method is the simplicity of its use for in-situ monitoring of bacteria in real time. For example, Schmitt and Flemming designed a flow cell based on a ATR crystal and monitored the formation and growth of biofilm for over 20 days in a bypass of the drinking water system, as shown in Figure 1.3[56].

Bacteria cells are a extreme complex of chemical compositions including nucleic acids, proteins, cytoplasms, cell membrane and wall, and their spectra look similar to each other. It is difficult to intuitively distinguish different strains from their spectra and

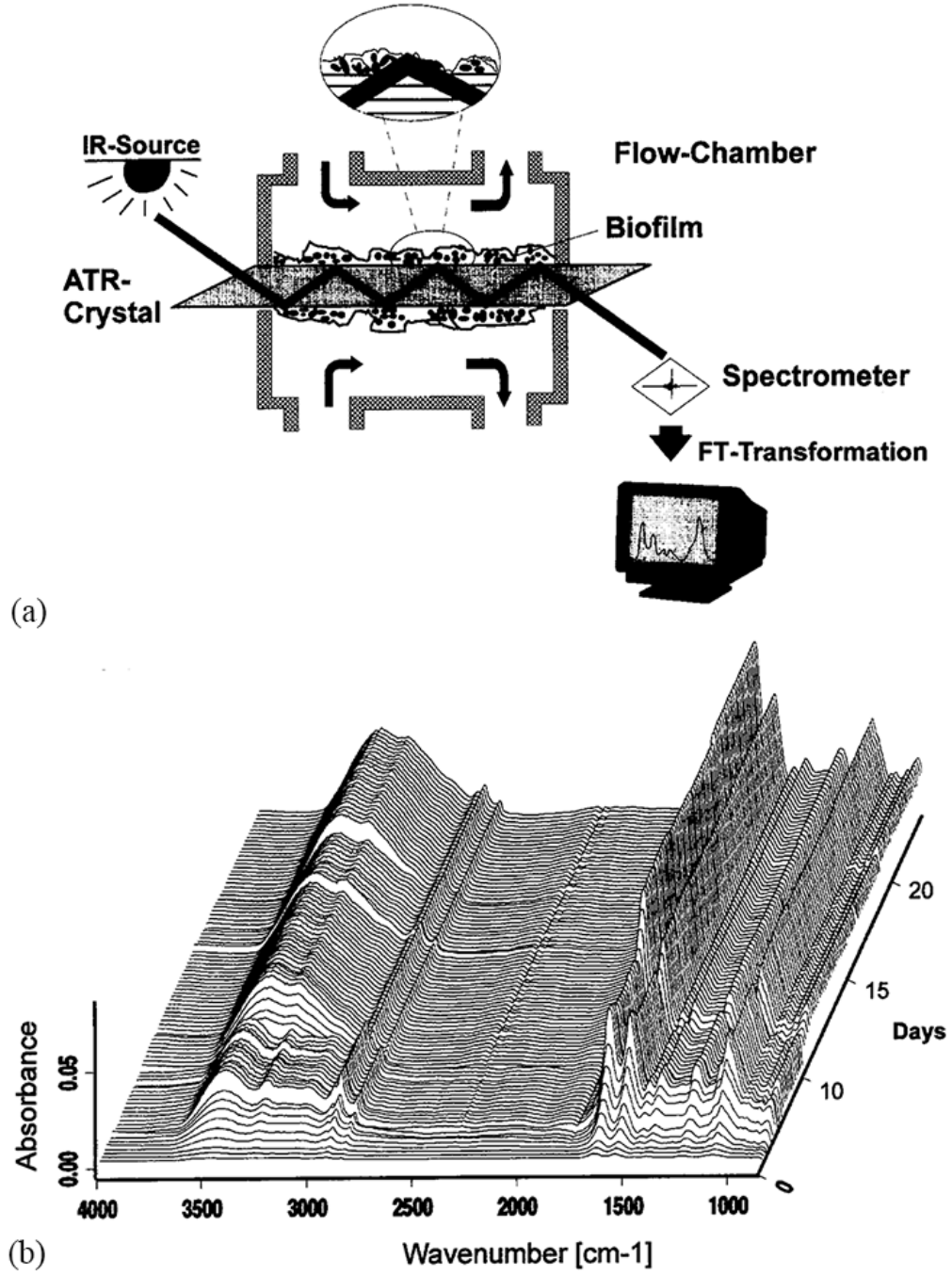


FIGURE 1.3: (a) Schematic depiction of the design of biofilm investigation with an ATR cell; (b) Time-dependent development of FTIR spectra in an ATR cell during adhesion and biofilm growth in a bypass of a drinking water system. Reprinted from Reference [56] with permission from Elsevier.

thus mathematical analyses are essential to recognize the spectra. The commonly used analysis methods include principal component analysis (PCA), factor analysis (FA), canonical variate analysis (CVA), and soft independent modeling of class analogy (SIMCA), as summarized in Table 1.6.

Although FTIR spectroscopy features relative simplicity on sample preparation and rapidity on spectral measurements, the reproducibility of FTIR relies on the stringent of sample preparation protocol. Samples with concentrations less than $10^4$ CFU/mL may not produce adequate IR signals. This limits its application for the monitoring of bacteria in drinking water where the concentration of microorganisms is ultra-low[65]. Therefore, concentrating procedures must be performed to increase the cell concentration prior to using the FTIR spectroscopy for the detection, differentiation and identification of bacteria in drinking water.

### 1.3.5 Flow cytometric method

Flow cytometry is a promising method for waterborne pathogen monitoring because it features simultaneous detection of multi-color fluorescence and scattered light from single cells at high throughput[72]. It can be used to measure multiple parameters of cells, including cell size, granularity and fluorescently marked constituents. In addition, the high throughput analysis at rates of $10^2 - 10^5$cells/s in typical applications (sample concentration $> 10^5$cells/mL) such as blood cell analysis, also enables its applications for rare cell detection such as waterborne bacteria with a low throughput for low concentration samples flowing at typical velocities of about 1m/s.

Figure 1.4 shows a schematic representation of a conventional flow cytometer[73]. Particles in the sample flow is hydrodynamically focused with a small diameter into the center of flow channel, passing through the light beam one by one. The intersection between the flow channel and light beam is called the interrogation region. Each particle is interrogated by the light beam, producing forward scattered (FSC) and side scattered (SSC) light, as well as fluorescence signals if fluorochrome is linked to the particles or autofluorescence exists. A light barrier is placed at the front of the FSC detector to avoid direct illumination from the laser. SSC and fluorescence light signals are collected in a direction perpendicular to the light beam and separated by

Table 1.6: Summary of the bacterial studies using FTIR spectroscopy.

| Aim | Spectral range used ($cm^{-1}$) | FTIR technique | Analysis method | Ref. |
|---|---|---|---|---|
| In situ monitoring of an E. coli fermentation | 1900 - 650 | DiComp probe ATR | | [57] |
| Discrimination of cyanobacterial strains | 1800 - 800 | FTIR microscope | PCA, SIMCA, KNN | [58] |
| Real-time multianalyte monitoring of fermentations | 1500 - 900 | DiComp probe ATR | | [59] |
| Interactions of selenium species with bacterial cells | 1550 - 850 | Transmission | HCA, PCA | [60] |
| Rapid discrimination of Alicyclobacillus strains | 1500 - 900 | ZnSe ATR | PCA, SIMCA | [61] |
| Light-induced reactions of E. cili DNA photolyase | 1800 - 1100 | Transmission | | [62] |
| Rapid detection and identification of Pseudomonas aeruginosa and E. coli | 1800 - 900 | Diamond ATR | PCA, SIMCA | [63] |
| Detection and identification of E. coli O157:H7 and Alicyclobacillus strains | 1800 - 900 | Diamond ATR | PCA, SIMCA | [64] |
| Differentiate E. coli O157:H7 from other bacteria | 1800 - 850 | ZnSe ATR | PCA, SIMCA | [65] |
| Discrimination of Staphylococcus aureus strains from different species of Staphylococcus | 1800 - 800 | Transmission | Mahalanobis distance | [66] |
| Photocatalytic degradation of pathogenic bacteria with $AgI/TiO_2$ under visible light irradiation | 4000 - 2500<br>1900 - 900 | Transmission | | [67] |
| On-line monitoring of nine different E. coli cultures | 1800 - 800 | DiComp probe ATR | library-based matching | [68] |
| Effect of chlorine-induced bacterial injury | 1800 - 900 | Diamond ATR | PCA | [69] |
| Investigate biological effect of an ultra-strong static magnetic field on E. coli and Staphylococcus aureus | 3100 - 700 | Transmission | Cluster analysis | [70] |
| Detection of E. coli O157:H7 from ground beef | 1600 - 750 | FTIR microscopy | PLSR, CVA | [71] |
| Quantitative analysis of E. coli K-12 internalized in baby spinach | 2800 - 1300 | ATR | CVA | [54] |
| Study the survival and injury of E. coli, Campylobacter jejuni and P. aeruginosa under cold stress in low nutrient media | 1800 - 900 | Diamond ATR | PCA, SIMCA | [55] |

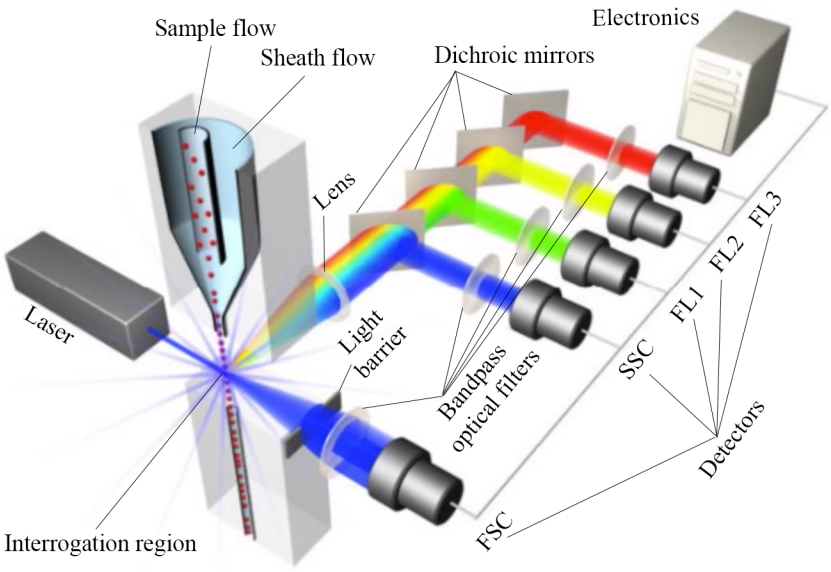


FIGURE 1.4: Schematic representation of a conventional flow cytometer. Reprinted from Reference [73].

a series of dichroic mirrors with different cut-off wavelengths. All the light signals are detected synchronously and analyzed by a computer.

Flow cytometry has been used for rapid detection of pathogenic E. coli [74, 75], enumeration of total bacteria [76–80], assessment of bacterial viability [81] and determination of bacterial growth phase [82] but with staining of the cells or their constituents with fluorescent tags. Although this approach increases the speed of detection, it still uses expensive flow cytometers and additional sample preparation steps which limits their on-site use [83].

Micro-flow cytometers (MFCs) based on micro-fabricated fluidic devices provide considerable opportunities to overcome the limitation of high operating cost because the amount of reagents needed by a microfluidic device is dramatically reduced [84]. Furthermore, integration of optical components such as waveguides, buried fibers or lenses [85] into the microfluidic devices replaces the bulk lens system and aligns optical paths automatically, thus increasing portability, shock-resistance and reliability [86–89]. Compared with conventional flow cytometers that utilize 3D hydrodynamic sample centering and 3D light focusing in free space to ensure good interaction between excitation light beam and interrogated particles, most micro-flow cytometers

suffer from the planar structures that only allow for 2D sample centering and 2D light focusing, resulting in a reduced detection efficiency of the particles or cells.

Using 3D optics in free space for excitation light focusing, but 2D sample centering by electrokinetics in microfluidic channels, a detection efficiency of 98% for 0.93 $\mu$m fluorescently labeled beads and 94% for E. coli labeled with a fluorescein-conjugated antibody at low throughputs was achieved [84, 90]. Using 2D sample centering by hydrodynamics, detection efficiencies above 89% for both 1 $\mu$m fluorescently labeled beads and E. coli were resolved [91]. Further improvements using a 3D sample centering by a multi-channel hydrodynamic focusing led to a detection efficiency of 97% for fluorescent latex beads [92].

However, micro-flow cytometers still require the labeling process of the target microorganisms, for example, using the fluorochrome-conjugated antibodies, which limits its use on the in-line monitoring of bacteria in drinking water. Improvements must be conducted on the current micro-flow cytometers to overcome these limitations.

In addition, there are some other methods reported, but not included in this work, such as biological field effect transistor [93] and Raman spectroscopy [94–96].

## 1.4 Proposed method

In the previous sections, many technologies have been reviewed on the perspective of potential for on-line monitoring of bacteria in drinking water. Standard methods can provide accurate estimations on both the species of bacterial strains and their concentrations, but need long time of analysis. Emerging methods can realized rapid detection of microorganisms, but still have some limitations. Therefore, a novel method is proposed to overcome these limitations and fulfill the goal of in-line monitoring in real time.

The proposed system is illustrated in Figure 1.5. This system is based on the combination of FTIR spectroscopic and micro-flow cytometric methods. The former can provide information for bacterial differentiation and identification and the latter measures the total concentration of all the bacteria present in the sample. Then, the concentration of each bacterial strain can be calculated from the results of FTIR and

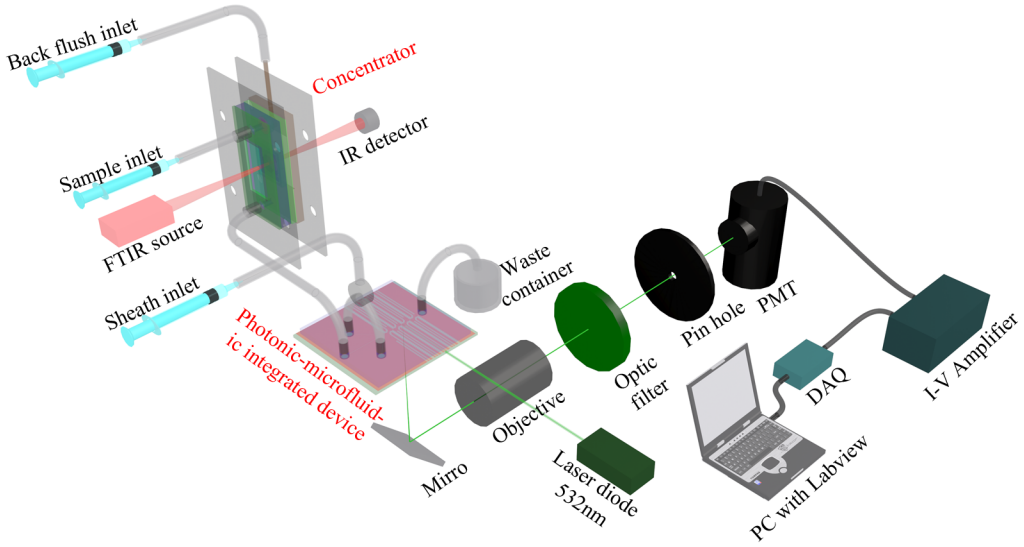


FIGURE 1.5: Proposed system towards in-line detection of bacteria in drinking water.

MFC measurements. For on-line use, there is little sample preparation that can be integrated into the system. Therefore, the IR spectra of bacterial cells have to obtained directly in water and thus a $CaF_2$ concentrator is designed to facilitate the FTIR measurements. Moreover, a micro-flow cytometer based on a photonic-microfluidic integrated device is developed and used for bacterial cell counting.

## 1.5 Research contribution and dissertation organization

This research work contributes to the detection, differentiation, identification and quantification of bacterial cells in drinking water, and it can be used to rapidly estimate the microbiological water quality. This information is needed for the prevention of the spreading of waterborne illnesses through the water distribution network and thus to protect human health.

Researches in this work include direct FTIR measurement in water, fabrication of $CaF_2$ device and discovery of a novel stress release process of $SiNx/CaF_2$ film/substrate system. It also includes the optimization of the fabrication procedure of a photonic-microfluidic integrated device that acts as the core device of a micro-flow cytometer and characterization of the MFC as well as counting E. coli cells using the fabricated MFC.

In Chapter 2, a description of the details on performing FTIR measurements of bacterial cells directly in a water environment and the analysis method for bacterial differentiation. A preliminary study on the fabrication of $CaF_2$ concentrator is also conducted. A novel phenomenon on the stress release of silicon nitride films on $CaF_2$ substrate was discovered and studied.

In Chapter 3, the structure of the photonic-microfluidic integrated device, fabrication procedures and their improvements as well the systematic setup of the micro-flow cytometer based on this device including optical alignment and coupling, on-chip beam shaping and SSC collection and detection are presented.

Characterization of the MFC built using standard microspheres and simulations on the one-dimensional hydrodynamic focusing are presented in Chapter 4. Although only 1D focusing is adopted, we demonstrate that there is almost no degradation in the absolute counting efficiency when the focused sample stream expands from 2.5 to 12.5$\mu$m with increased sample-to-sheath flow rate ratio because of the improved data analysis method. In addition, the 1D hydrodynamic focusing of particles is simulated using COMSOL to trace the movement trajectories of particles in the channel, obtaining the relationship of the width of focused sample stream of particles on the sample to sheath flow rate ratio. A complete performance characterization of the micro-flow cytometer is provided with its throughput versus both sample flow rate and sample concentration with good linearity for both.

The capability of detecting E. coli cells using the MFC is given in Chapter 5. A discussion of the results, highlighting the system performance through testing with micro-beads, counting E. coli and separation of E. coli from background noise due to similar sized particles is provided. Then, to put our work in perspective, we tabulate the key performance measures of similar micro-flow cytometers and ours.

Finally, in Chapter 6, a summary of the main achievements of this work and suggestions on the research in future are provided.

# Chapter 2

# Direct Acquisition of Infrared Spectra of Bacteria in Water

The first objective of the proposed system is the rapid detection, differentiation and identification of the bacteria present in drinking or source water with an ultimate goal of continuous monitoring of bacterial level automatically. Fourier transform infrared (FTIR) spectroscopy is selected to fulfill this objective due to its technical advancement in the past 25 years and the improved speed of spectral analysis. However, direct acquisition of IR spectra of bacteria in water is challenging because water is a strong absorber in mid-IR range. Also, FTIR with attenuated total reflection (ATR) technique is not suitable for in-line measurements on mixture of different species of bacteria because it only measures the superficial layer of bacteria attached onto the ATR crystal, although it can eliminate the influence of water. Therefore, transmission FTIR is adopted and improved for the direct acquisition of IR spectra of bacteria in a water environment. In this chapter, first, FTIR spectroscopy is briefly introduced. Then, the IR spectra of common bacteria in drinking water are obtained, based on which their differentiation is performed using spectral decomposition and principal component analysis. Finally, a preliminary study is carried out on concentrating bacteria in the flow cell. A novel phenomenon on silicon nitride films on calcium fluoride substrate was discovered during the fabrication of the concentrator.

## 2.1 FTIR spectroscopy

The IR light spectrum can be divided into three regions based on the light wavelength or wavenumber, near-IR (0.7–2.5$\mu$m or 14000–4000$cm^{-1}$), mid-IR (2.5–25$\mu$m or 4000–400$cm^{-1}$) and far-IR (25–100$\mu$m or 400–10$cm^{-1}$). By convention, wavenumber is commonly used in IR spectroscopy. Because the primary vibrational energies of most organic molecules are low and their corresponding wavelengths lie in the

mid-IR region, mid-IR spectroscopy is commonly used to analyze the composition of organic complexes such as proteins, fatty acids, carbohydrates, nucleic acids and lipopolysaccharides.

### 2.1.1 FTIR Principle

An IR spectrum of a sample usually refers to its absorbance versus wavenumber in certain region, which measures the amount of light absorbed by the sample. The absorbance spectrum of a sample can be calculated by equation (2.1), in which the left side is the definition of absorbance and the right is derived from Beer's Law.

$$A = log_{10}(I_0/I) = \varepsilon lc \tag{2.1}$$

In (2.1), $A$ denotes the absorbance of a sample; $I_0$ and $I$ denote the intensity of the background and sample spectrum, respectively; $\varepsilon$ stands for the absorptivity of the sample, $l$ for the path length, and $c$ for the concentration of the sample. Note that $A, I_0, I, \varepsilon$ are dependent on wavelength or wavenumber.

In practice, broadband MIR sources are usually adopted because tunable MIR lasers are extremely expensive and their wavelength tuning range cannot fully cover the MIR range. To measure the spectrum of background or a sample under illumination of a broadband MIR source, Fourier transform method is utilized to simplify and speed up the detection of MIR light. Otherwise, a spectrometer will be needed to separate light of different wavelengths in space and then light intensity at each wavelength is measured, which requires a much longer detection time than using the Fourier transform method.

In FTIR spectroscopy with a Michelson interferometer, the Fourier transformation is performed between the optical path difference (OPD) of an interferometer and the wavenumber, as shown in equation (2.2).

$$I(k) = \int_{-L}^{L} I(\delta) e^{-2\pi i k \delta} d\delta, L \gg \lambda_{max}, \tag{2.2}$$

where $k$ stands for wavenumber, $I(k)$ for intensity spectrum in wavenumber, $\delta$ for the OPD, $I(\delta)$ for the measured intensity at different $\delta$, $L$ for the maximum of $\delta$ that

can be achieved in the interferometer, $\lambda_{max}$ is the maximum wavelength of the MIR source. $L \gg \lambda_{max}$ is an approximation of $L \to \infty$.

For each FTIR measurement, two scans are needed at least, one for the background interferogram and the other for the sample interferogram, i.e., $I_0(\delta)$ and $I(\delta)$. Then, $I_0(k)$ and $I(k)$ can be calculated by the Fourier transformation and thus absorbance spectrum of the sample can be determined. However, multiple scans are needed to achieve an interferogram with a good signal-to-noise ratio (SNR) by averaging the interferograms obtained in all scans. The SNR is proportional to the square root of the number of scans (N)[97], as shown by equation (2.3). For example, the SNR of a measurement with 16 scans will be 4 times to the SNR of that with only 1 scan.

$$SNR \propto N^{1/2}. \tag{2.3}$$

The resolution of a FTIR spectrometer determines the capability of the spectrometer to distinguish peaks that are close together, which is inversely proportional to the maximum OPD of the interferometer, $L$, as shown by equation (2.4). Therefore, high resolution will be denoted by a small number and low resolutions by large numbers. For example, if a sample has two peaks at 1400 $cm^{-1}$ and 1401 $cm^{-1}$ and they are well separated in the measured spectrum, it means the resolution used is 1 $cm^{-1}$, which is considered as "high resolution". On the other hand, if only peaks with 32 $cm^{-1}$ apart or larger can be resolved in the spectrum, the resolution of the spectrometer will be 32 $cm^{-1}$, which is called "low resolution".

$$Resolution \propto 1/L. \tag{2.4}$$

High resolution scans can provide more information on the sample spectrum, but are also noisier than low resolution scans. Therefore, there exists a trade-off between the SNR and resolution to achieve best characteristic spectrum of a sample. The optimal resolution relies on the physical state of the sample. Considering a gas sample, its molecules are well separated and the interactions between any two molecules can be ignored, so its absorbance spectrum is only determined by the vibrational modes of its molecule, exhibiting sharp peaks in the spectrum. Hence, high resolution is required

to resolve them, usually 2 $cm^{-1}$ or higher. On the other hand, molecules in solids or liquids are close to each other and the interactions between neighboring molecules cannot be ignored, which broaden the sharp peaks observed in a gas spectrum. The IR peaks of solids or liquids are usually 10 $cm^{-1}$ wide or more. Therefore, a resolution of 8 or 4 $cm^{-1}$ will be enough to measure the spectra of solids and liquids[97].

### 2.1.2 System setup

The instrument used to measure IR spectrum is a VERTEX 80v vacuum FTIR spectrometer from Bruker Corporation. Its optical diagram is shown schematically in Figure 2.1. Light beam emitted from the MIR source is focused by a concave mirror, then filtered by an aperture and collimated by another concave mirror. The light beam is divided into two beams by a beamsplitter, one reflected to the fixed mirror and the other transmitted to a moving mirror. Both beams are reflected by the mirrors and recombine at the beamsplitter, forming an interfered beam that enters the sample compartment through a KBr window and passes through the sample. The transmitted beam is focused onto a detector by a concave mirror. The light intensity is then digitized and recorded by electronic components in the instrument.

A helium-neon (He-Ne) laser emitting red light at 15797.71$cm^{-1}$ is also used to precisely measure the OPD of the interferometer during scans. The laser beam follows the MIR light through the interferometer and is detected by the laser detector before entering the sample compartment. The interferogram of a laser is a cosine wave with an OPD period of 0.633$\mu$m. Its maxima can be used as triggers for the MIR detector to sample the signal intensity data. After shifting the zero OPD to the centerburst of MIR interferogram, one scan is completed.

To eliminate the influence of the carbon dioxide and water vapor in the atmosphere, the spectrometer is evacuated to less than 5 Pa. The resolution and $N$ are set to 1 $cm^{-1}$ and 128, respectively. With these settings spectra of bacteria in water with good SNR and resolution of fine peaks are obtained.

### 2.1.3 Sample preparation

The bacterial strains used in this work are listed in Table 2.1. Each strain is streaked onto a trypticase soy agar plate and cultured overnight at 37℃. Then, the bacteria

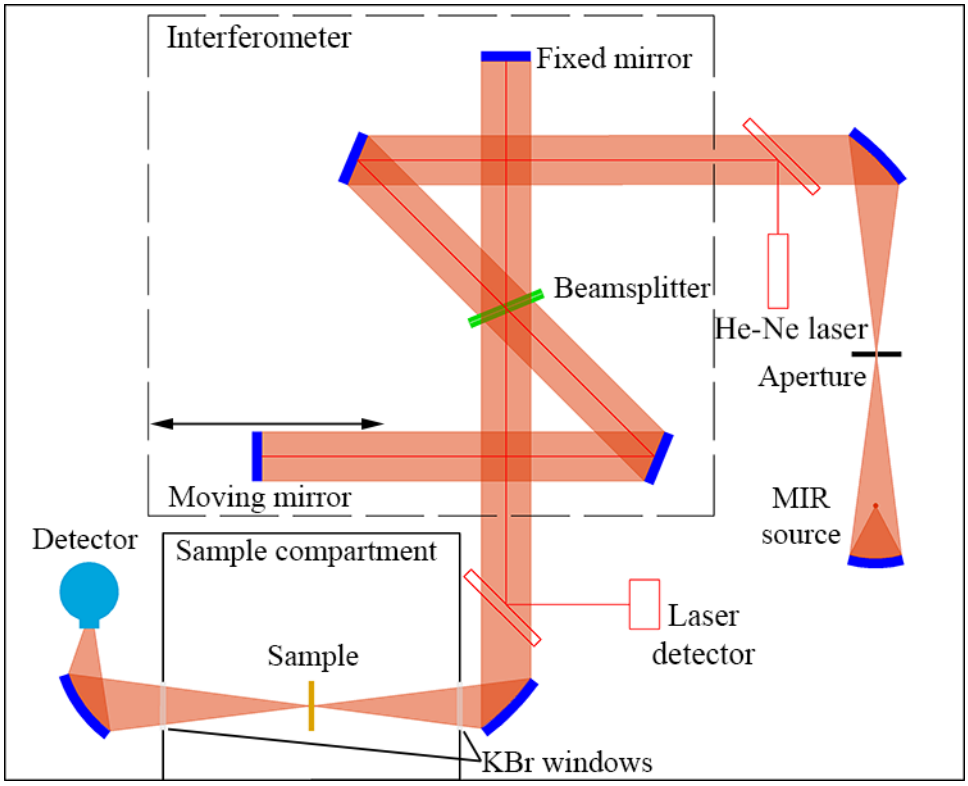


FIGURE 2.1: Optical diagram of the VERTEX 80v FTIR spectrometer.

in an isolated colony are picked up and inoculated into sterilized tryptic soy broth (TSB) to culture overnight at 37℃. The cultured bacterial suspension is washed with phosphate-buffered saline (PBS) using a centrifuge, which pellets the bacterial cells so that the supernatant can be discarded and cells can be re-suspended in PBS. The washing procedure is repeated 3 times to ensure complete removal of the culture media, in which the nutrients contribute to the absorbance spectrum of the bacterial sample. The concentration of bacterial suspension is evaluated by measuring its optical density at 600nm ($OD_{600}$) using a spectrophotometer. The concentration of all the strains is on the order of $10^{10}$cells/mL.

The bacterial sample is injected into a liquid cell of FTIR spectrometer, which is purchased from REFLEX Analytical Corporation (Ridgewood, New Jersey, USA). Figure 2.2 shows the exploded view of the liquid cell, which is primarily comprised of two calcium fluoride ($CaF_2$) windows (drilled and undrilled) separated by a hollow

TABLE 2.1: The list of bacterial strains used in this work.

| No. | Species | Strain |
|---|---|---|
| 1 | Escherichia coli | K-12 MG1655 |
| 2 | Escherichia coli | K-12 HS2210 |
| 3 | Aeromonas jandaei | ATCC 49568 |
| 4 | Aeromonas media | ATCC BBA-229 |
| 5 | Enterococcus casseliflavus | ATCC 700327 |
| 6 | Enterococcus durans | ATCC 11576 |
| 7 | Enterococcus gallinarum | ATCC 700425 |
| 8 | Enterococcus hirae | ATCC 8043 |
| 9 | Enterococcus sccharolyticus | ATCC 43076 |

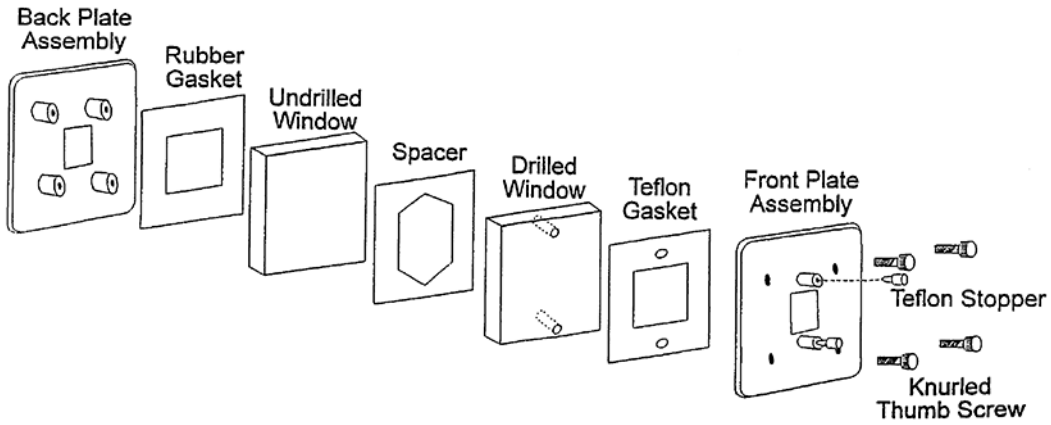


FIGURE 2.2: Exploded view of the flow cell of FTIR spectroscopy for bacterial samples.

gasket spacer with a thickness of 25$\mu$m. $CaF_2$ is selected because it has a transparent range of 0.15–10$\mu$m (equivalent to 66667–1000$cm^{-1}$) and is insoluble in water.

## 2.2 IR spectra of bacteria in water

Water is a strong absorber in the MIR range. However, it still has spectral windows where the spectrum of bacteria cells suspended in water can be measured as long as the optical path length in the suspension is short enough, for example, less than 30$\mu$m. Figure 2.3 presents transmittance spectrum of double distilled water sample in a $CaF_2$ liquid cell. It is obvious that there exist two windows in 3000–1700$cm^{-1}$ and 1600–1000$cm^{-1}$ ranges, respectively. The latter is selected to measure the bacterial suspension in water because the "fingerprint region" of bacteria is located between

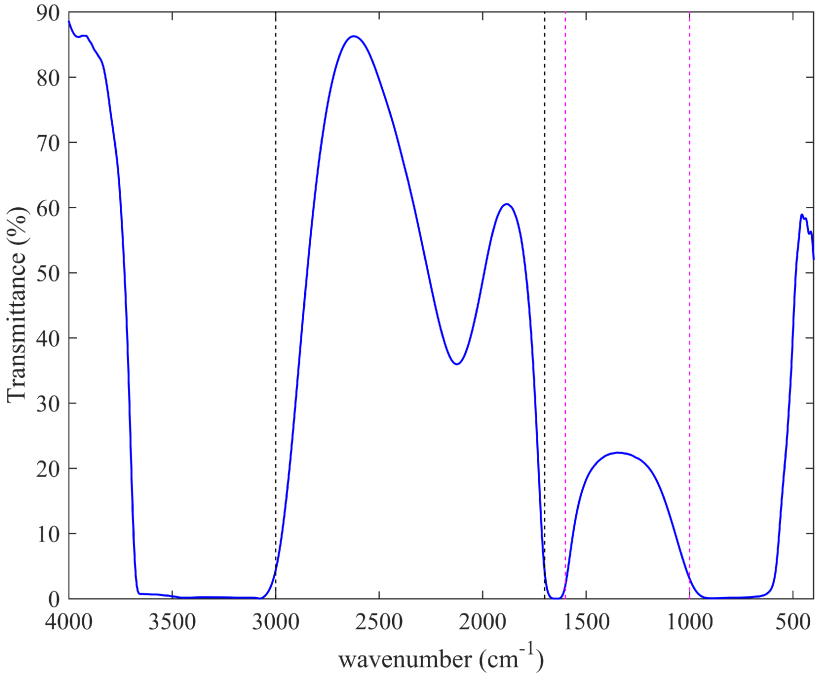


FIGURE 2.3: Transmittance spectrum of double distilled water sample in a $CaF_2$ liquid cell defining a 25$\mu$m path length.

1300 and 900 $cm^{-1}$, which corresponds to the absorptions of proteins, nucleic acids, cell membrane and cell wall components[58, 64].

All spectra of the strains listed in Table 2.1 are plotted in the window range, as shown in Figure 2.4. All spectra are adjusted to the same peak height at 1085 $cm^{-1}$ for intuitive comparisons, which corresponds to the absorption of P=O symmetrical stretch of the phosphodiester backbone of nucleic acids. The assignment of major spectral peaks in the bacterial spectra is shown in Table 2.2.

## 2.3 Spectral differentiation of bacterial species

As shown in Figure 2.4, all spectra look similar and thus it is difficult to differentiate them directly from their spectra. Therefore, we need to determine what features can be used for their differentiation. This can be achieved by many methods such as clustering or classification. Principle component analysis (PCA) is adopted because it transforms the high-dimension space into a low-dimension space, in which the

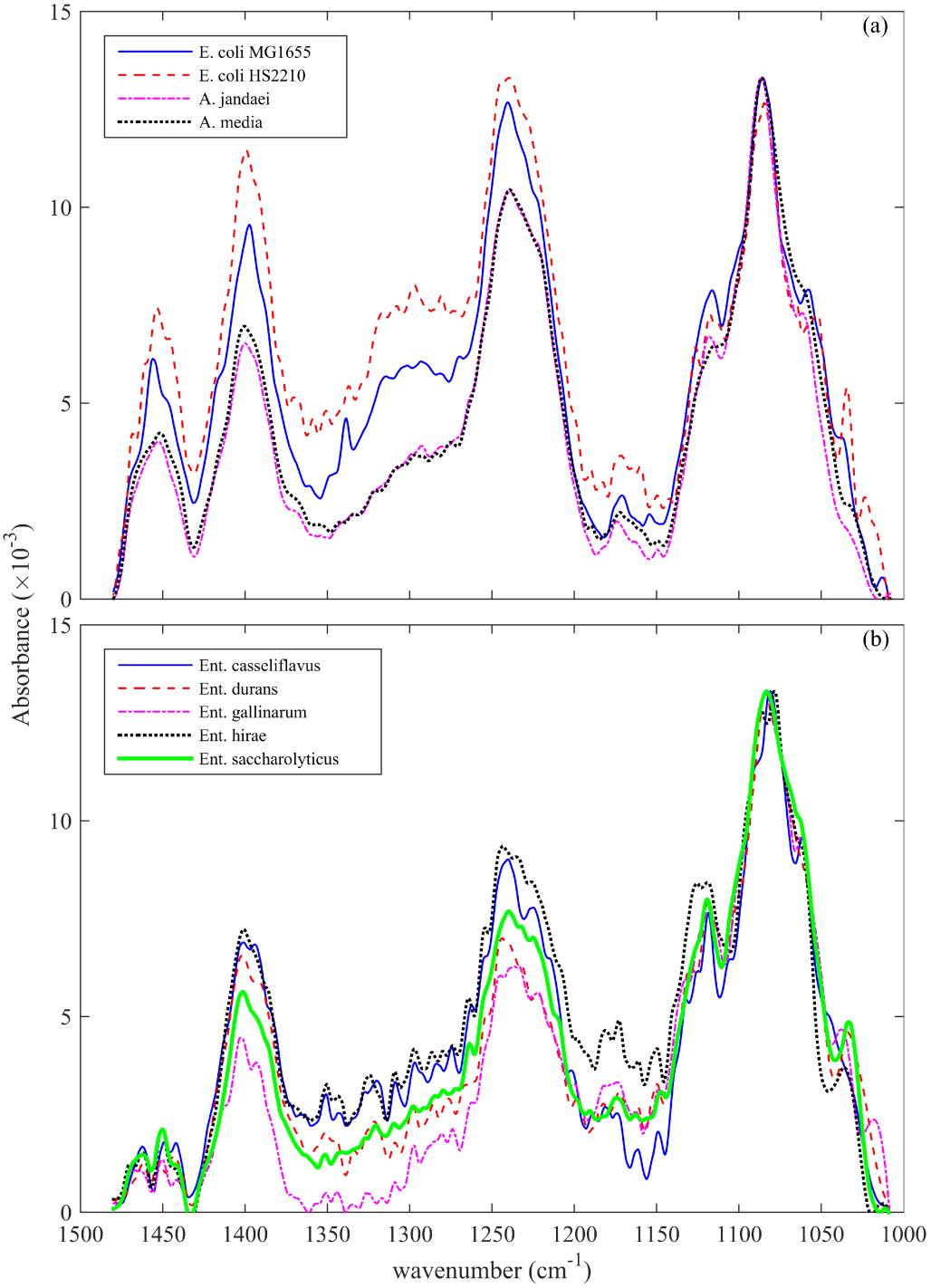


FIGURE 2.4: IR spectra of the bacterial samples measured directly in water. (a) is for the strains of E. coli MG1655 and HS2210, Aeromonas jandaei and media; (b) is for the strains of Enterococcus casseliflavus, durans, gallinarum, hirae, and saccharolyticus.

TABLE 2.2: Assignment of major spectral peaks in the bacterial spectra.

| Wavenumber ($cm^{-1}$) | Assignment |
|---|---|
| ~1455 | asymmetric deformation of $CH_3$ and $CH_2$ of proteins |
| ~1400 | symmetric deformation of $CH_3$ and $CH_2$ of proteins<br>symmetric stretch of C–O of $COO^-$ groups |
| ~1242 | asymmetric stretch of P=O in the nucleic acid backbones |
| ~1080 | symmetric stretch of P=O in the nucleic acid backbones |
| 1200-900 | stretching vibrations of C-O-C of polysaccharides |

largest variances between each other are sought. Commonly, two-dimensional or three-dimensional space is selected for visualization.

### 2.3.1 Spectrum decomposition

In each spectrum, the peak position, height and width are the key information relating to the molecules of the sample. But usually, many peaks exist and overlap with each other, so each spectrum is decomposed into multiple single peaks using curve fitting with Gaussian functions as shown in Equation (2.5). The fitting is performed iteratively with increasing order $n$ until the coefficient of determination ($R^2$) reaches 0.9999 (four nines).

$$y = \sum_{i=1}^{n} a_i e^{-(\frac{x-b_i}{c_i})^2} \tag{2.5}$$

All the spectra of bacteria are processed in the same way and one example of the curve fitting is shown using the spectrum of E. coli MG1655 in Figure 2.5. The absolute residues of zero shown prove the goodness of fitting.

### 2.3.2 Principle component analysis of spectra

The PCA is performed on the second derivative of all the IR spectra of bacteria listed in Table 2.1 using customized Matlab codes (shown in Appendix C). Each bacterium was measured 8 times, so there were 72 spectra in total. The algorithm used for PCA is singular value decomposition of the matrix comprised of all the spectra. The scores of the first 3 principal components are plotted in Figure 2.6(a),

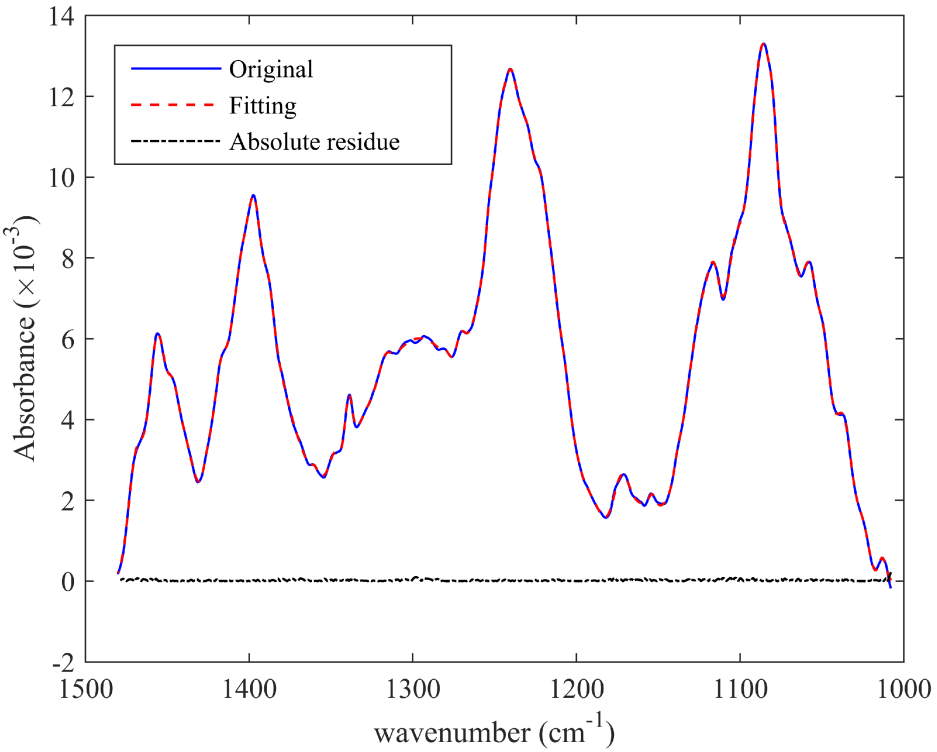


FIGURE 2.5: Curve fitting for the IR spectrum of E. coli MG1655 using multiple Gaussian functions.

from which the clustering of spectra from different species is seen. The scores 1 and 2 in Figure 2.6(b) demonstrate that the species of E. coli is separated from that of aeromonas and enterococcus. And the further differentiation between aeromonas and enterococcus is achieved based on the score 3, as shown in Figure 2.6(c) and (d).

## 2.4 Preliminary study on $CaF_2$ concentrator

In the FTIR spectrometer, the beam diameter of the MIR light passing through the $CaF_2$ cuvette is about 1mm, which means that the interaction volume between the light beam and sample is about 20nL. Meanwhile, the concentration of bacteria is on the order of $10^{10}$cells/mL, so the number of bacterial cells inside the interaction volume is about $2 \times 10^5$cells. However, the concentration of bacteria is usually less than $10^3$cells/mL in drinking water even when it is contaminated. Therefore, a concentrator is needed to filter about 200mL of raw water sample and to transfer the bacterial cells in the interaction volume for FTIR measurements.

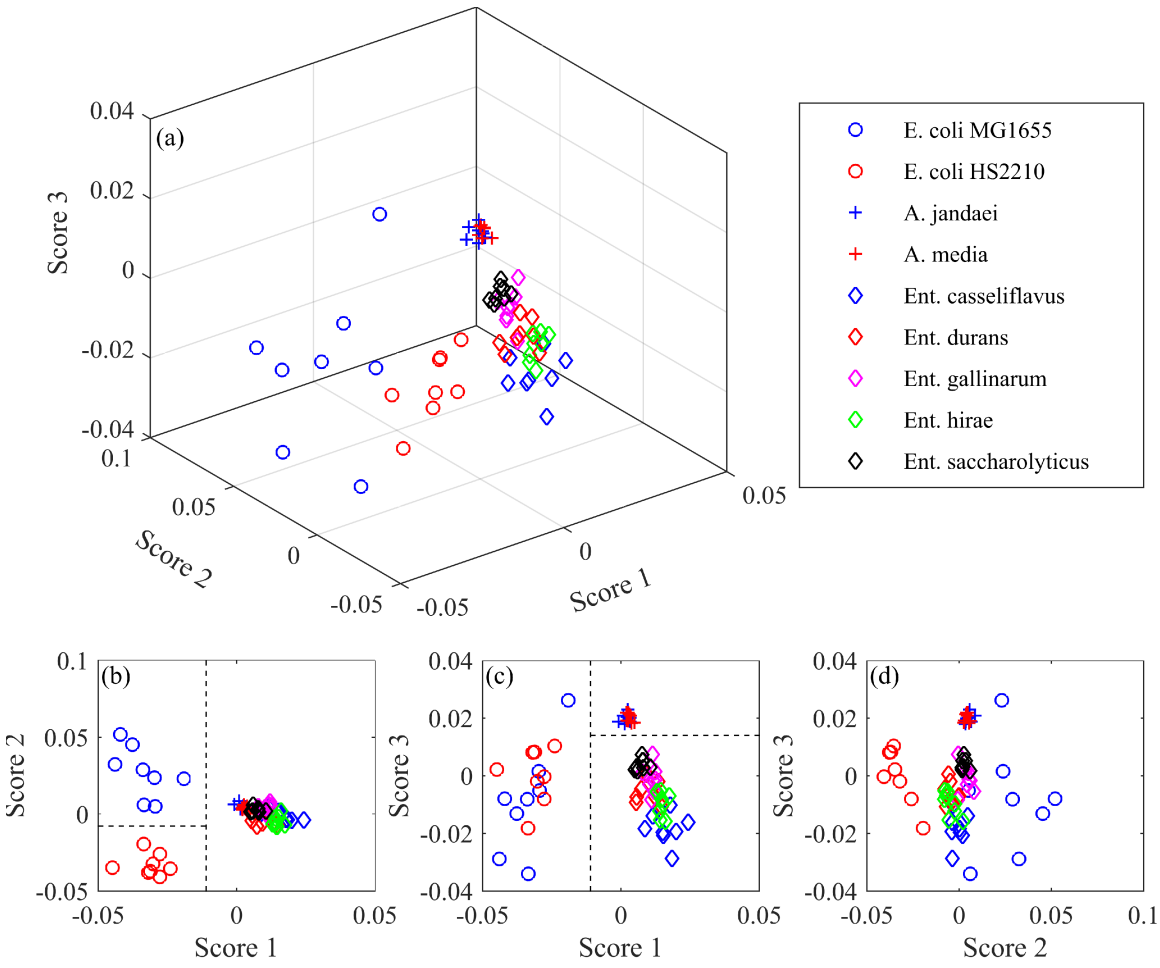


FIGURE 2.6: Principal component analysis of the IR spectra of bacteria listed in Table 2.1.

There are two ways to realize the concentration of bacterial cells. First, filtration is performed directly in the interaction volume and thus there is no needed to transfer cells, which requires that the filtration component is integrated in the interaction volume. This can be achieved by fabricating micro-structures in the $CaF_2$ using etching methods. Second, the filtration component is separate from the interaction volume, where the concentrated bacterial cells will then be transferred.

$CaF_2$ is selected among a series of MIR-transparent materials such as KBr and ZnSe because of its insolubility and non-toxicity. Both methods are tried to fabricated this $CaF_2$ concentrator.

### 2.4.1 Wet etching of $CaF_2$

$CaF_2$ is a compound crystalline in a cubic structure with a space group of Fm3m and the lattice constants of its unit cell are 5.462Å and 4Å for $a$ and $z$, respectively. It is insoluble in water or organic solutions, but slightly soluble in acids. Figure 2.7 shows the etching pits of (100) $CaF_2$ in HCl acid with different mask openings of (a) $2.5\mu m \times 2.5\mu m$, (b) $4.5\mu m \times 5.5\mu m$, (c) $4.5\mu m \times 7.5\mu m$ and (d) $8.5\mu m \times 8.5\mu m$. The edges of these pits are aligned with the crystalline orientation [110], demonstrating the anisotropic etching process of $CaF_2$ in HCl acid.

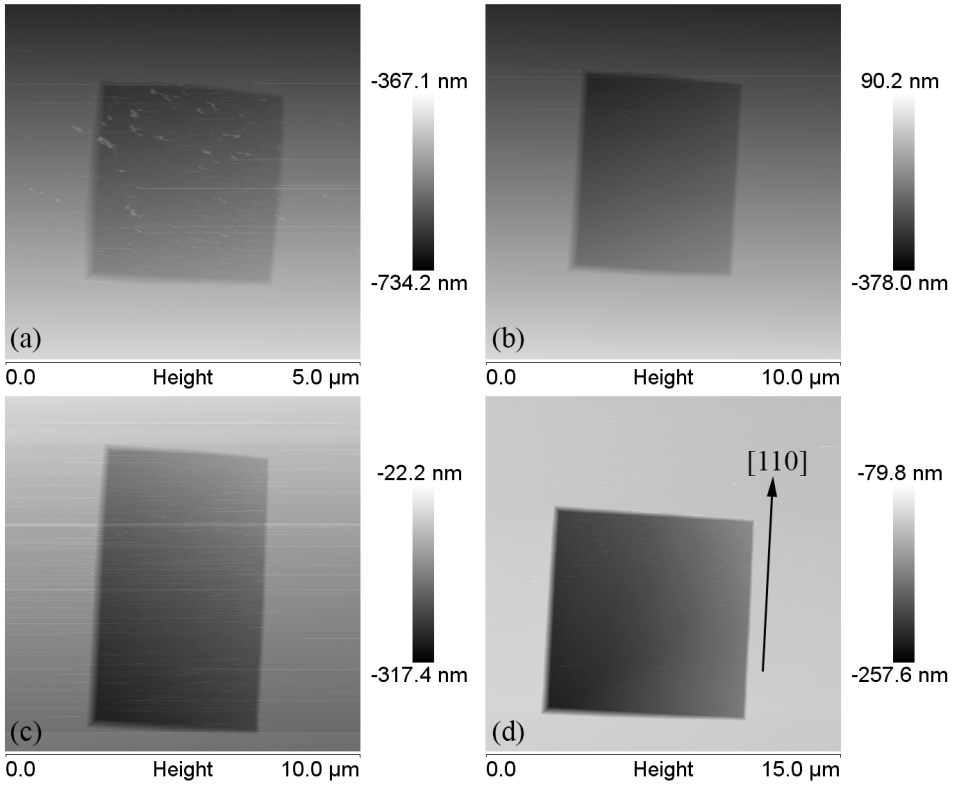


FIGURE 2.7: Etching pits of (100) $CaF_2$ in HCl acid with different mask openings of (a) $2.5\mu m \times 2.5\mu m$, (b) $4.5\mu m \times 5.5\mu m$, (c) $4.5\mu m \times 7.5\mu m$ and (d) $8.5\mu m \times 8.5\mu m$.

Note that all the etching depths in Figure 2.7 are less than 200 nm, which is not enough for the micro-structure. Therefore, longer time is needed to achieve deeper etching. However, it was found that long time etching would ruin $CaF_2$ crystal. Figure 2.8 presents two photos of a (100) $CaF_2$ crystal before and after etching. The

reason for this etching failure is because the etching speed at sites with crystalline defects such as dislocation is much faster than the regular etching speed[98].

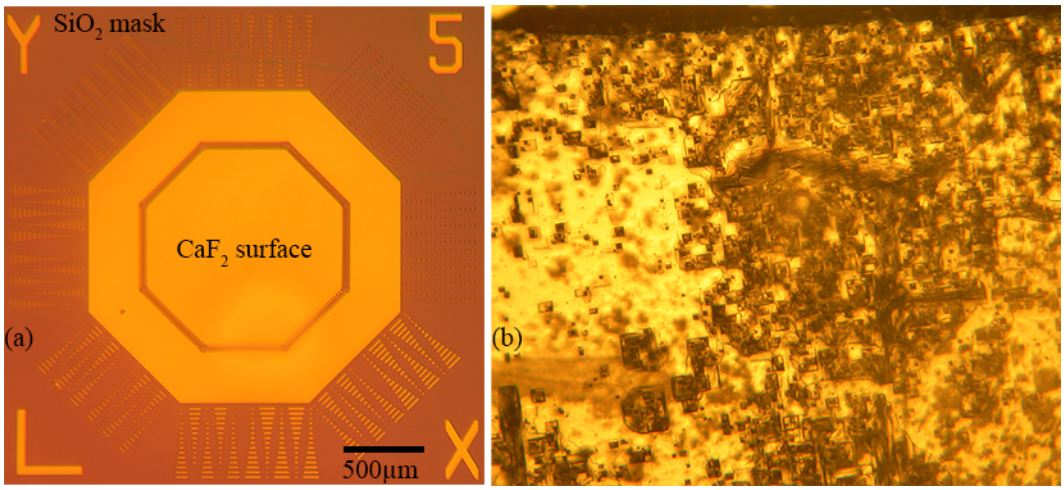


FIGURE 2.8: (a) $SiO_2$ etching mask pattern on $CaF_2$; (b) photo the $CaF_2$ surface afer etching in HCl acid for 1 hour.

### 2.4.2 Integration of $CaF_2$ with filtration membrane

The second method to fabricate the concentrator is to integrate a separate filtration component with the $CaF_2$ crystal. Figures 2.9(a) and (b) present the 3D model and photo of a concentrating device that integrates a $CaF_2$ crystal and a filter membrane in polydimethylsiloxane (PDMS). The $CaF_2$ crystal is surrounded by PDMS with openings on both of the top and bottom surfaces. Microfluidic channels with a width of 100$\mu$m and a height of 25$\mu$m connect the filter membrane (hydrophilic polycarbonate with a diameter of 13mm and 0.2$\mu$m pores), which is placed underneath the channels. The fabricated concentrating device is then assembled with another $CaF_2$ plate with drilled holes and a backflush plate, as presented by the exploded view in Figure 2.9(c). All the components are aligned and secured by screws through the four holes in the top and bottom plates.

The functionality of the fabricated concentrator is tested using 1$\mu$m-diameter fluorescent polystyrene beads. Figure 2.10(a) presents a photo of the concentrator after filtering a bead suspension ($1 \times 10^6$ beads/mL) for 10 minutes at a flow rate of 1mL/min. The detailed view in Figure 2.10(b) proves that all the beads are blocked by the membrane.

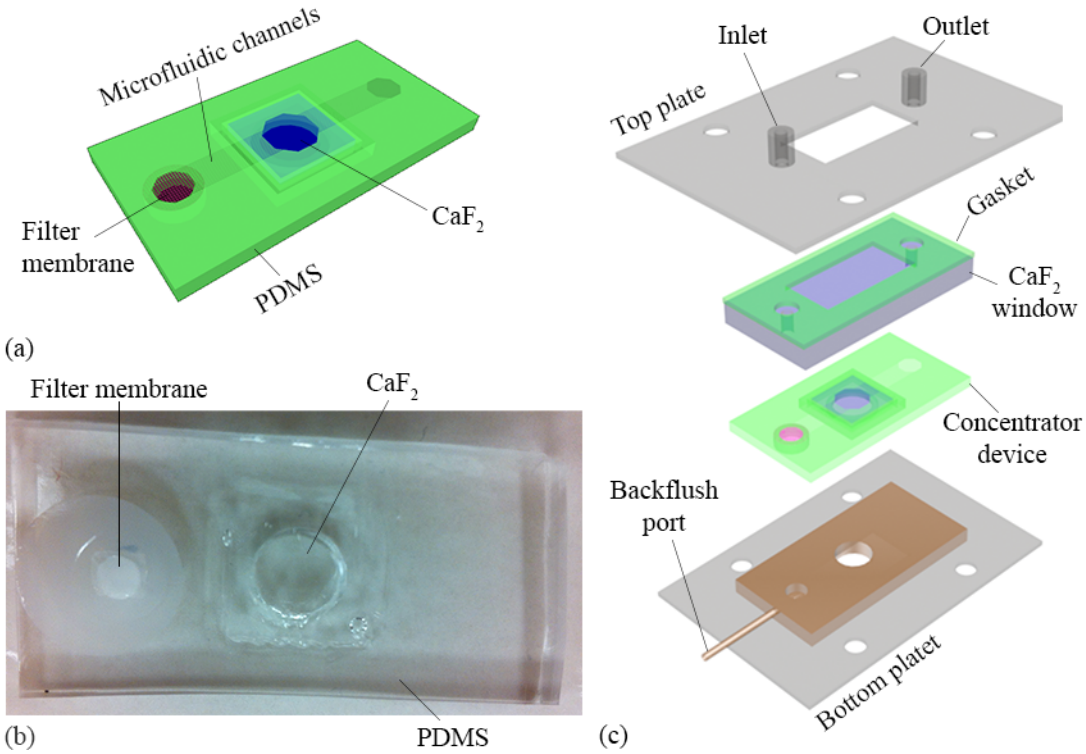


FIGURE 2.9: (a) 3D model of the concentrating device integrating a $CaF_2$ crystal and a filter membrane within PDMS; (b) photo of the fabricated concentrating device; (c) exploded view of the concentrator.

Only a preliminary study has been conducted on the design, fabrication and performance test and more efforts should be put to this aspect in future. However, a novel phenomenon is discovered during the micro-structure fabrication on $CaF_2$ crystals, as detailed in the next Section[99].

## 2.5 Ultra-slow stress release in silicon nitride films on $CaF_2$

Thin films coated onto substrates by sputtering or vapor deposition often suffer from high residual stress, either compressive or tensile, which usually causes film buckling or cracking. In most cases, biaxial compressive stresses exist in the film, one of which causes the buckling with finite width and height, while the other perpendicular stress cause the buckling propagation in a sinusoidal manner, called the telephone

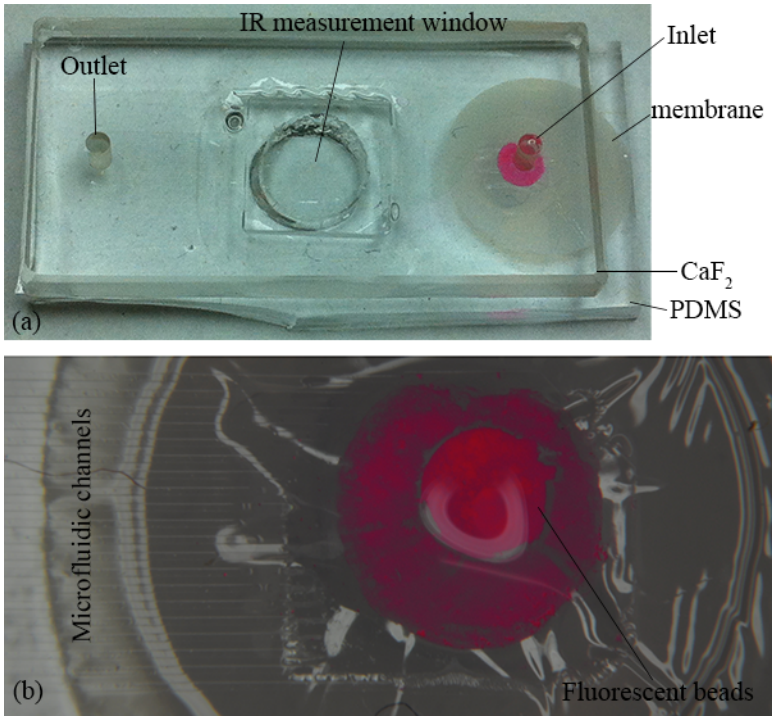


FIGURE 2.10: (a) Filtration test of the concentrator using 1$\mu$m-diameter fluorescent beads; (b) detailed view of the membrane after the filtration.

cord mode[100]. These buckling morphologies formed in thin films to release internal compressive stresses were observed in many film/substrate combinations, including carbon/quartz glass and carbon/Si[100–106], boron/glass[101], TiC/quartz[107], permalloy/Si and permalloy/glass[108], bcc stainless steel/fcc stainless steel[109] and aluminum/glass[110]. The buckling was generally considered as a film failure and undesirable, but its profile can be used to determine the mechanical properties of the film such as Young's modulus[101–104, 107], because the buckling formation requires appropriate combination of the internal film stress and interface adhesion force; otherwise the film will either adhere to or fully delaminate from the substrate. Note all these film/substrate systems mentioned above were stiff films on rigid substrates.

Recently, many researchers focused on the stiff films on compliant substrates, for example, gold film on polydimethylsiloxane (PDMS), because they can form ordered structures spontaneously[111–113] and some novel applications such as phase grating, nanochannels for protein concentration or smart adhesion[114–116]. The films capitalize on the large elastic modulus mismatch between the film and substrate to obtain

wrinkling of the substrate surface and consequently wrinkling of the stiff film. However, in stiff films on rigid substrates, ordered patterns forming spontaneously have not been reported before, although the formation of wavy buckling can be controlled by artificially introducing low adhesion areas on the substrate by lithographically patterning[100] or laser beam scanning[110].

A new film/substrate combination, silicon nitride ($SiN_x$)/calcium fluoride ($CaF_2$), is investigated to further reveal the influence of the rigid substrate on the formation of the telephone cord buckles. In addition, the study on the film instability of $SiN_x$ on $CaF_2$ will be beneficial for fabrication of novel $CaF_2$ based devices. $CaF_2$ has an optical transmission range of 150-9000nm, from ultraviolet (UV) to middle infrared (MIR). Together with its insolubility in water, it is a promising material to make devices allowing simultaneous spectral analyses of aqueous samples in multiple regions, for example, quantitative determination of cell concentration in the visible range and qualitative identification by IR spectroscopy [117–120]. These applications requires $CaF_2$ based devices with microstructures such as microfluidic channels for fluid handling or micro pillar arrays for dielectrophoretic concentrating microbes in water[121–123], which requires that the dielectric thin films act as a protective layer or an etching mask. For this application $SiN_x$ film is a good choice as it has been widely used in micro-opto-electro-mechanical systems (MOEMS) and micro-electro-mechanical systems (MEMS). Therefore, $SiN_x$ thin films are coated onto $CaF_2$ substrates by plasma-enhanced chemical vapor deposition (PECVD) and the buckling formation processes are studied.

### 2.5.1 Deposition of silicon nitride films on $CaF_2$

$CaF_2$ crystal substrates of (100) and (111) orientations and $10\times10mm^2$ area, 1.0mm-thick and surface roughness of less than 2.5nm were purchased from MTI Corporation. $SiN_x$ films with thicknesses in the range of 50–200nm were deposited on (100) and (111) $CaF_2$ substrates by PECVD at 300℃ with a deposition rate of 8.33nm/min by the following reaction:

$$3SiH_4(g) + 4NH_3(g) \longrightarrow Si_3N_4(s) + 12H_2(g). \tag{2.6}$$

The reactant gas flow rates were 7.15 standard cubic centimeters per minute (sccm) for silane ($SiH_4$) and 900 sccm for ammonium ($NH_3$). The chamber pressure was stabilized to 87 Pa during the reaction and 50W power of a 13.56 MHz radio frequency (RF) source used to ionize the reactant gas molecules.

### 2.5.2 Observation of buckling formation and propagation

#### 2.5.2.1 Microscopic observation

Immediately after removing the $CaF_2$ substrates with 100nm $SiN_x$ films from the PECVD chamber, they were observed under a microscope, as shown in Figure 2.11, (a) and (b) for $SiN_x$ on (100) $CaF_2$, and (c) and (d) for (111) $CaF_2$. Note that Figure 2.11 (b) and (d) are magnified view of the regions indicated by the rectangles in (a) and (c), respectively. Wrinkles formed initially at the edges of both (100) and (111) $CaF_2$ substrates and telephone cord buckles propagated along defined directions in the inner periphery of the wrinkled area. These views show that the stress releasing process is initiated from the substrate edges where the periodical crystalline structure of $CaF_2$ ends and it develops along defined orientations of $CaF_2$ substrate, not randomly.

The crystal orientations of the horizontal and vertical edges (x and y directions in Figure 2.11 of (100) $CaF_2$ are $[01\bar{1}]$ and [011], respectively, but are $[\bar{1}10]$ and $[\bar{1}\bar{1}2]$ for (111) $CaF_2$. On the (100) $CaF_2$ substrate, the two orientations along which the telephone cord buckles propagate are at $\pm45°$angle with respect to x axis, indicating that the buckles propagate at orientations of [010] and [001]. Angles of $\pm60°$show that the buckles propagate at orientations of $[\bar{1}01]$ and $[01\bar{1}]$ on the (111) $CaF_2$ substrate.These buckle propagating directions indicates that the stress of $SiN_x$ film on (100) $CaF_2$ is biaxial along [001] and [010] and that for (111) $CaF_2$ is triaxial along $[\bar{1}10]$, $[\bar{1}2\bar{1}]$ and $[2\bar{1}\bar{1}]$, which means the film stress is related to the crystalline structure of the substrate although the film is not grown epitaxially because PECVD $SiN_x$ films were mostly amorphous or polycrystalline at low deposition temperatures[124].

#### 2.5.2.2 Buckle profiling

The front-end of a telephone cord buckle in Figure 2.11(b) was profiled by using Atomic Force Microscopy (AFM), shown in Figure 2.12(a), which shows the buckling

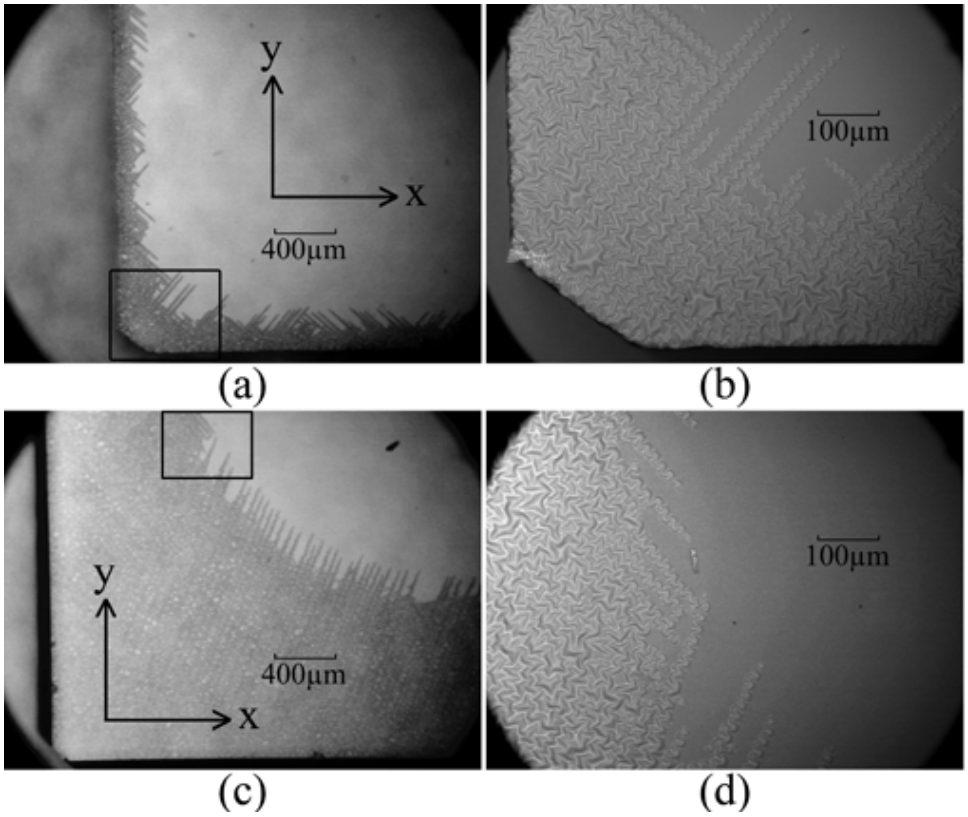


FIGURE 2.11: (a) Microscopic views of 100nm-thick $SiN_x$ film deposited by PECVD on (100) $CaF_2$ (a, b) and (111) $CaF_2$ (c, d). Photos were taken immediately after removing the $CaF_2$ substrates from the PECVD chamber. (b) and (d) are magnified views of the regions indicated by the rectangles in (a) and (c), respectively.

height of about 800nm. Because the thickness of the $SiN_x$ film is 100nm, much less than the buckling height, we believe the buckled film is detached from the substrate. The formation of buckles during stress releasing implies that $SiN_x$ films are compressively stressed on $CaF_2$ crystals. Figure 2.12(b) shows the dimensions of the buckling width, 2b=18μm, and the undulating wavelength, l =17.3μm, of the telephone cord buckle, yielding a l/2b of 0.961, which is in agreement with previous calculations in Ref 1. The half-width, b0, associated with the onset of buckling is calculated to be 1.2μm and the stress is estimated to be 1GPa using the model in Ref. 1 with Young's modulus of 150GPa and Poisson's ratio of 0.3 for the $SiN_x$ film[125].

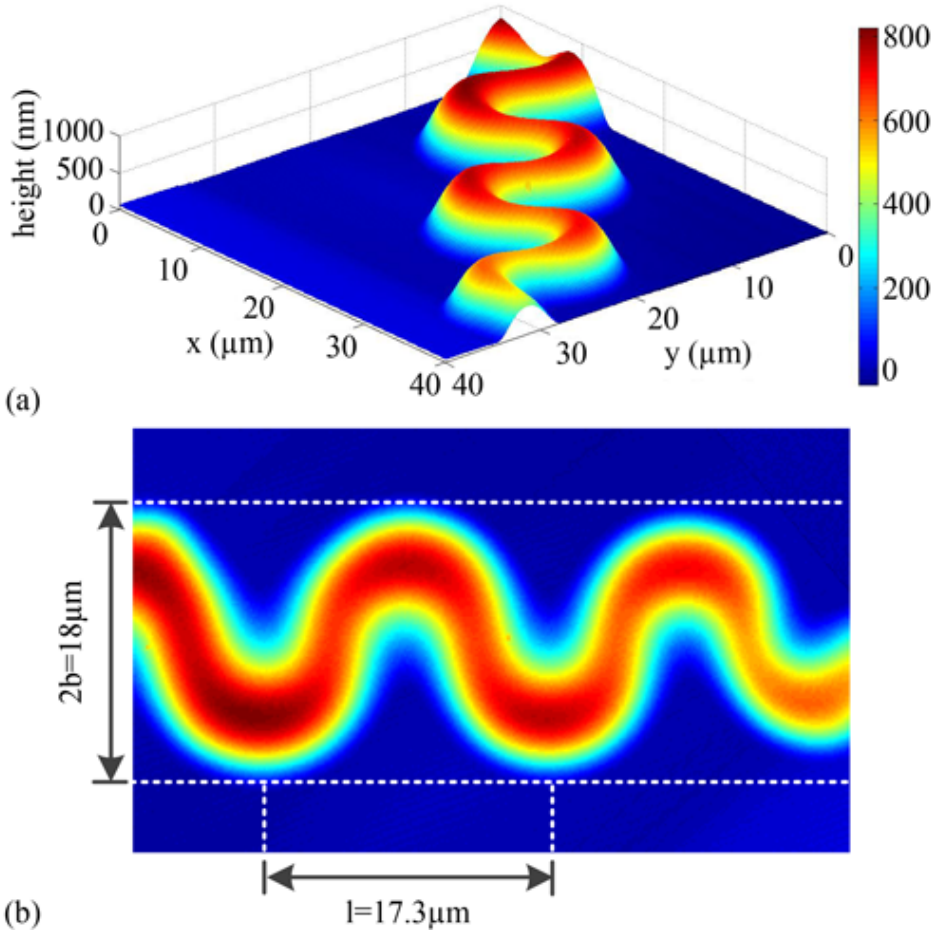


FIGURE 2.12: (a) Three-dimension profiling of the front-end of a telephone cord buckle by AFM; (b) Measurements of the buckling width, 2b=18$\mu$m, and the undulating wavelength, l=17.3$\mu$m.

#### 2.5.2.3 Macroscopic observation

The complete processes of stress release were recorded macroscopically by taking photos of 100nm $SiN_x$ films on both (100) and (111) $CaF_2$ substrates at different times, as shown in Figure 2.13, (a)-(d) for (100) $CaF_2$ and (e)-(h) for (111) $CaF_2$, (a) and (e) for the time right after removing both $CaF_2$ substrates from the PECVD chamber, (b) and (f), (c) and (g), (d) and (h) for 1.5 hours, 28 hours, 67 hours afterwards, respectively. The upper left corner of (100) $CaF_2$ crystal was covered by a Silicon wafer during the deposition of $SiN_x$ in the PECVD chamber, resulting in no $SiN_x$ on the corner. Stress release indicated by the wrinkled areas starts from the

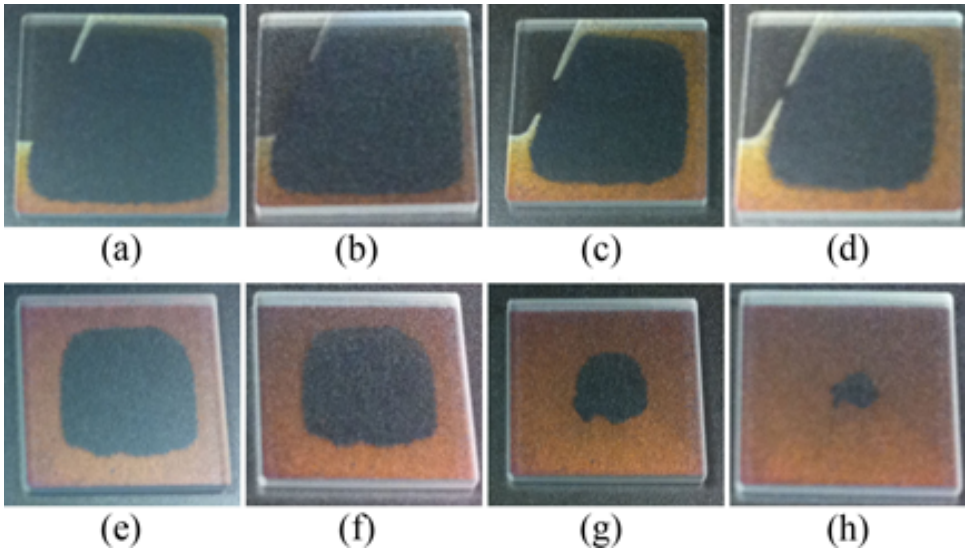


FIGURE 2.13: Photos of 100nm-thick $SiN_x$ films deposited on (100) (a-d) and (111) (e-h) $CaF_2$ substrates by PECVD at different time after removing them from the PECVD chamber. (a, e) time = 0; (b, f) time = 1.5 hour; (c, g) time = 28 hour; (d, h) time = 67 hour.

substrate edges except for the corner, further proving that stress release is initiated from the discontinuity of the periodical crystalline structure of the substrates.

#### 2.5.2.4 Buckle propagation

The stress releasing processes of 100nm $SiN_x$ films on both (100) and (111) $CaF_2$ substrates were observed by recording 30 minutes videos under a microscope, in which 4 frames at the time of 0, 10, 20 and 30 minutes are shown in Figure 2.14, (a-d) for (100) $CaF_2$ and (e-h) for (111) $CaF_2$, (a) and (e) for the time right after removing $CaF_2$ crystals from the PECVD chamber, (b) and (f), (c) and (g), (d) and (h) for 10, 20, 30 minutes afterwards, respectively. We can see that the telephone cord buckles are growing along certain orientations described above.

In addition, the growth of the telephone cord buckles of $SiN_x$ on (111) $CaF_2$ is faster than on (100) $CaF_2$, because the largest interplanar spacing of (111) $CaF_2$ is smaller than that of (100) $CaF_2$ and thus the lattice mismatch of $SiN_x$ on (111) $CaF_2$ is larger, resulting in larger internal compressive stress on (111) $CaF_2$. And the growing velocity decays with time for $SiN_x$ on both (100) and (111) $CaF_2$. The initial stress releasing velocity of $SiN_x$ was defined by the average propagation velocity in the first

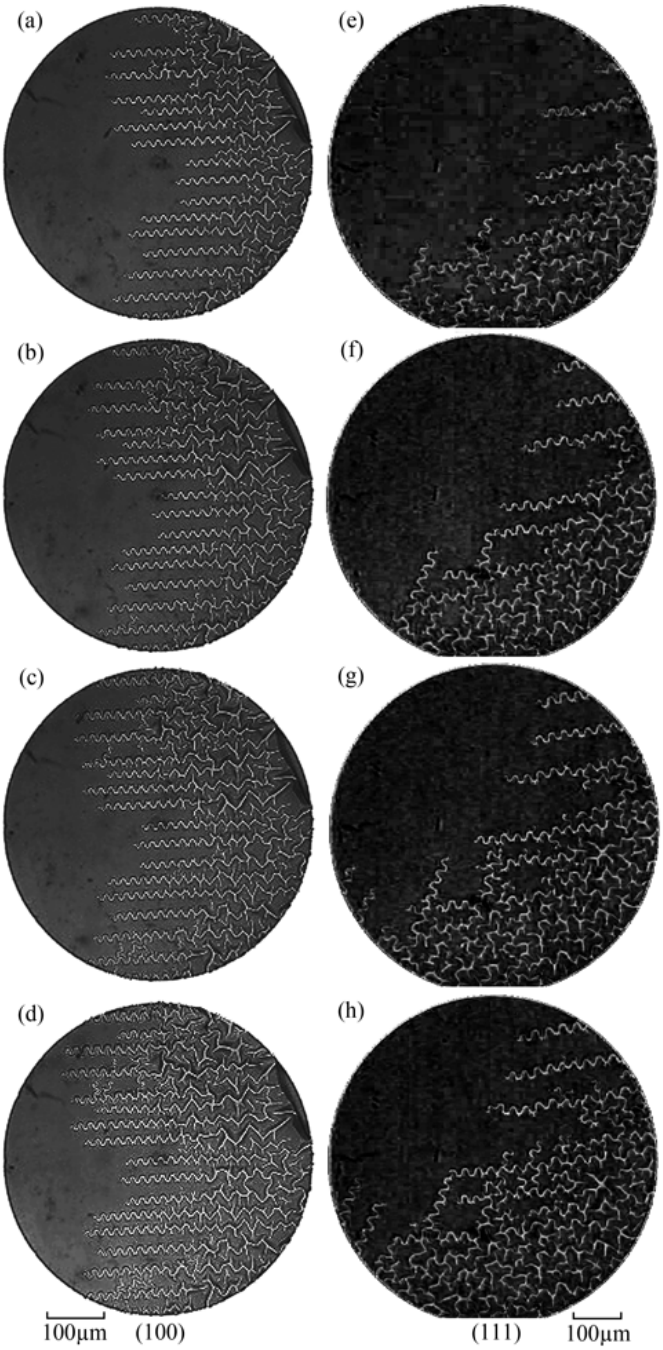


FIGURE 2.14: Growth of the telephone cord buckles during the stress releasing processes of 100nm $SiN_x$ films deposited by PECVD on (100) $CaF_2$ (a-d) and (111) $CaF_2$ (e-h). (a, e): time = 0; (b, f): time = 10 minutes; (c, g): time = 20 minutes; (d, h): time = 30 minutes.

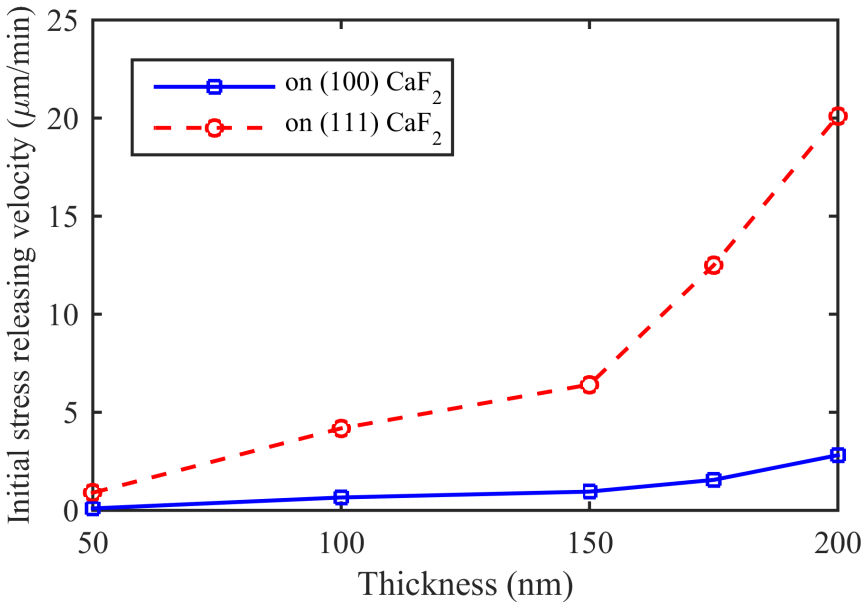


FIGURE 2.15: Dependence of initial stress releasing velocity of $SiN_x$ film on (100) $CaF_2$ (square symbol) and (111) $CaF_2$ (circle symbol) on film thickness.

30min after removing $SiN_x$ on $CaF_2$ from the PECVD chamber and was measured by the recorded video for different thicknesses of $SiN_x$, 50-200nm, shown in Figure 2.15. For the same thickness of $SiN_x$ film, the stress release on (111) $CaF_2$ is faster than on (100) $CaF_2$ because the film on (111) $CaF_2$ exhibits a larger stress that drives the growth of buckles. Their initial stress releasing velocities increase with the film thickness, because thicker $SiN_x$ film provides larger stress to drive the buckles growing faster.

### 2.5.3 Characterization of silicon nitride

The $SiN_x$ films on $CaF_2$ substrates are characterized by X-ray diffraction (XRD) crystallography and X-ray photoelectron spectroscopy (XPS).

#### 2.5.3.1 XRD analysis

Silicon nitride deposited at low temperatures (<400℃) are usually considered to be amorphous, however, it may also show certain crystallinity on a short range, such as polycrystalline[124]. Therefore, X-ray diffraction spectra of $SiN_x$ films on (100) and

(111) $CaF_2$ are measured to determine the crystallinity of PECVD $SiN_x$, as shown in Figure 2.16.

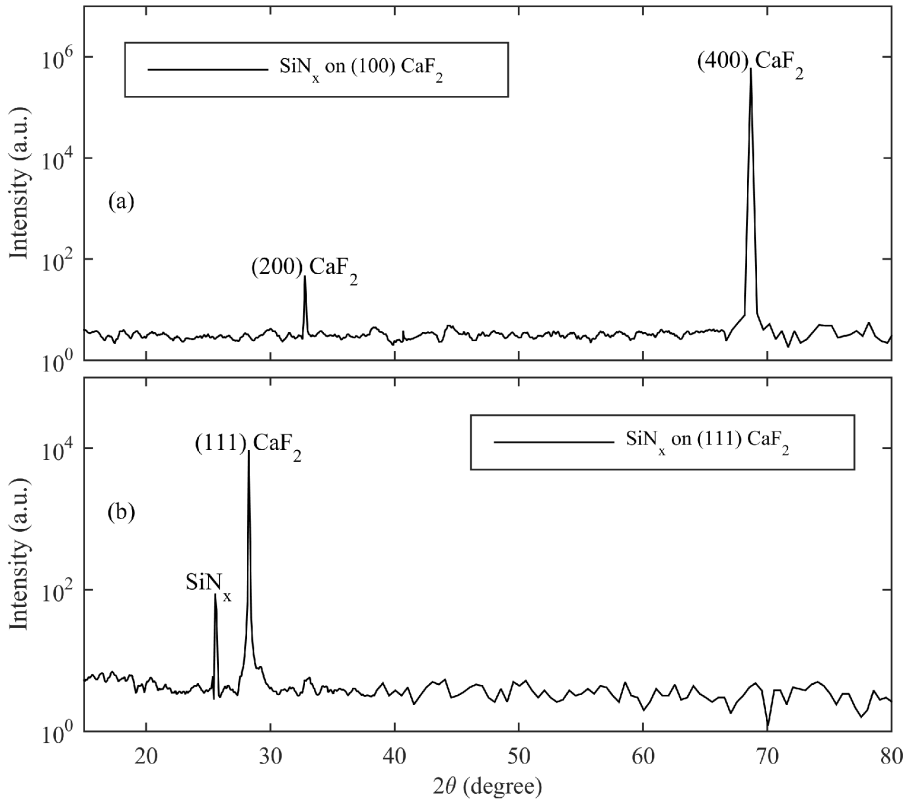


FIGURE 2.16: XRD spectra of silicon nitride films on (100) $CaF_2$ (a) and (111) $CaF_2$ (b).

Recalling the Bragg's law,

$$2d\sin\theta = n\lambda \tag{2.7}$$

where $d$ is the interplanar distance of lattice planes, $\theta$ is the angle between incident X-ray and the sample surface, $n$ is the order of diffraction and is a positive integer, $\lambda$ is the wavelength of X-ray ($\lambda$=1.54056Å). Because $CaF_2$ has a cubic crystal structure with a lattice constant, a, of 5.462Å, the interplanar distance of (hkl) planes will be

$$d = \frac{a}{\sqrt{h^2 + k^2 + l^2}} \tag{2.8}$$

For the simplicity of analysis, the order of diffraction is fixed at 1 (i.e., $n = 1$), so we get

$$h^2 + k^2 + l^2 = (\frac{2a \sin\theta}{\lambda})^2 \tag{2.9}$$

and the calculation of the Bragg planes corresponding to the peaks shown in Figure 2.16 and virtual $2\theta$ for the Bragg planes (100) and (110) are summarized in Table 2.3. Apparently, the $2\theta$ of peak 1 is far away from the $2\theta$ corresponding to (100) and (110) plans of the $CaF_2$ substrate, which means it can only arise from the $SiN_x$ film. This peak also indicates the films are polycrystalline, exhibiting short range crystallinity.

TABLE 2.3: Calculation of the Bragg planes corresponding to the peaks shown in Figure 2.16 and virtual $2\theta$ for the Bragg planes (100) and (110).

| peak | $2\theta$ (°) | $h^2 + k^2 + l^2$ | Bragg plane |
|---|---|---|---|
| 1 | 25.56 | 2.46 | — |
| 2 | 28.26 | 3.00 | (111) |
| 3 | 32.78 | 4.00 | (200) |
| 4 | 68.68 | 16.00 | (400) |
| | 16.21 | 1.00 | (100) |
| | 23.01 | 2.00 | (110) |

#### 2.5.3.2 Origin of film stress

Regarding physical origins of the stress generated in the $SiN_x$ films, two generic mechanisms had been proposed before, 1) surface stress mechanism[126–128] and 2) flux-driven incorporation of excess atoms in grain boundaries [128, 129]. We prefer to recall the former because it involves the contribution from substrate. For the 100nm $SiN_x$ films on $CaF_2$ substrate, the stress can be evaluated by equation (2.10)[129].

$$\sigma(h) = \sigma_0 - (f_1 + f_2)(\frac{1}{h_{cont}} - \frac{1}{h}) \tag{2.10}$$

where $\sigma(h)$ is the stress of film with thickness of $h$, $\sigma_0$ is the net tensile stress when the film has just become fully continuous, $f_1$ is the surface stress associated with the free surface of the $SiN_x$ film, i.e., the top surface, $f_2$ is the interfacial surface stress

associated the $SiN_x/CaF_2$ interface. In this model, $f_1$ and $f_2$ were assumed to be isotropic surface stresses for the simplicity of analysis. However, it is not the case for the $SiN_x/CaF_2$, where at least $f_2$ has relationship to the crystallographic structure of the $CaF_2$ substrate, which results in the biaxial stress for $SiN_x$ film on (100) $CaF_2$ and triaxial stress for $SiN_x$ film on (111) $CaF_2$, and thus the buckle propagating directions aligned with the crystallographic orientations of the $CaF_2$ substrate.

#### 2.5.3.3 XPS analysis

The buckling of $SiN_x$ films starts immediately when they were removed from the vacuum chamber and exposed to the atmosphere for films kept in vacuum for different time periods. There exists the possibility that air reacts with the film and the change of atomic ratio of $SiN_x$ initializes the formation and growth of buckles. To investigate this possibility, the stressed and stress-released films were characterized by X-ray photoelectron spectroscopy (XPS) performed on a 100nm-thick $SiN_x$ film on (100) $CaF_2$ crystal. Using a focused argon ion beam etching, XPS spectra of stressed $SiN_x$ in the center of $CaF_2$ (Figure 2.17a) and stress-released $SiN_x$ near the edges of $CaF_2$ (Figure 2.17b) were obtained at different depths from the film's top surface. In the spectra for the film's top surface, peaks corresponding to oxygen are found because of the natural oxidization of $SiN_x$ by the oxygen in air. But they disappear in the following spectra after the argon ion beam etching, indicating no oxygen exists inside $SiN_x$ films. Therefore, the spectra except for the top surface spectrum can be used to determine the atomic ratio of nitrogen and silicon, that is x in $SiN_x$.

The X-ray photoelectron counts of the peaks of N and Si atoms in the spectra except for the top surface spectrum are summarized in Table 2.4. The atomic ratio, x, of $SiN_x$ film of stressed $SiN_x$ and stress-released $SiN_x$ are $0.691\pm0.025$ and $0.698\pm0.047$, respectively. The small difference of x between stressed and stress-released $SiN_x$ demonstrates that the stress release process is a complete physical change, not a chemical change involving reaction with air.

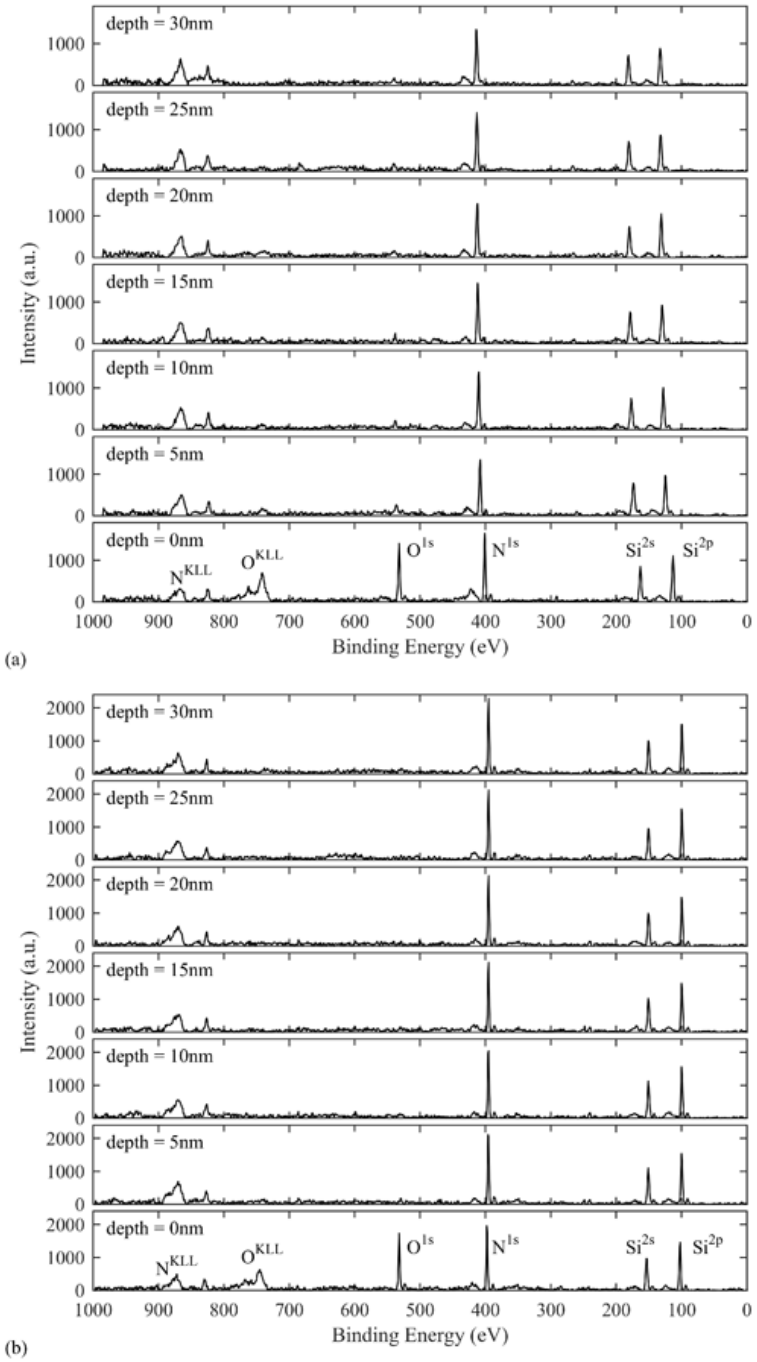


FIGURE 2.17: Depth profile of XPS spectra of 100nm Silicon nitride film on (100) $CaF_2$ by PECVD. (a) stressed area in the center of $CaF_2$ crystal; (b) stress-released area near the edge of $CaF_2$ crystal.

TABLE 2.4: Atomic ratio of stressed $SiN_x$, $x_1$, and stress-released $SiN_x$, $x_2$, calculated based on XPS analysis at different depth, d, from the surface, and their mean values, $\mu$, and standard deviation, $\sigma$.

| depth (nm) | $x_1$ (stressed) | $x_2$ (stress-released) |
|---|---|---|
| 5 | 0.664 | 0.694 |
| 10 | 0.670 | 0.757 |
| 15 | 0.734 | 0.656 |
| 20 | 0.688 | 0.682 |
| 25 | 0.692 | 0.646 |
| 30 | 0.697 | 0.753 |
| $\mu$ | 0.691 | 0.698 |
| $\sigma$ | 0.025 | 0.047 |

# Chapter 3

# A Micro-Flow Cytometer

The second objective of this thesis is to determine the concentration of bacteria in water samples to be tested, which is implemented using a micro-flow cytometer (MFC) based on a photonic-microfluidic integrated device. In this chapter, the structure, function and fabrication procedure of the device are described. In addition, some key procedures that dominate the device performance are optimized. Finally, the system setup of the MFC is elaborated in detail, including light source and optical coupling, on-chip beam shaping, scattered light collection and detection.

## 3.1 A photonic-microfluidic integrated device

A photonic-microfluidic integrated device incorporates microfluidic channels, optical lens system and waveguides together in one chip, which functions as the core part of the MFC. Figure 3.1 shows a three-dimensional model of a photonic-microfluidic integrated device and a finished device.

The structure of the device is shown by its top and front views in Figure 3.2. The device consists of four layers, Pyrex glass substrate, 30$\mu$m-thick SU-8 photoresist layer, PDMS covering layer and glass pads layer. The SU-8 photoresist layer is photolithographically patterned as a functionality layer and sealed by a PDMS covering layer with holes aligned with all inlets and outlet of the functionality layer, forming 50$\mu$m-wide microfluidic channels from the sample and sheath flow inlets to the outlet. It also forms optical waveguides with the SU-8 photoresist as core, Pyrex glass (bottom), PDMS (top) and air (both sides) as claddings. Glass pads with drilled holes are bonded to PDMS layer, which are used to fix and seal the inlet and outlet metal pins that are inserted into the PDMS holes to make fluid connections between the device and external components.

Figure 3.3 shows a detailed view of the functionality layer in the area indicated by the rectangle in Figure 3.2(a). Sidewalls of curved patterns where SU-8 photoresist

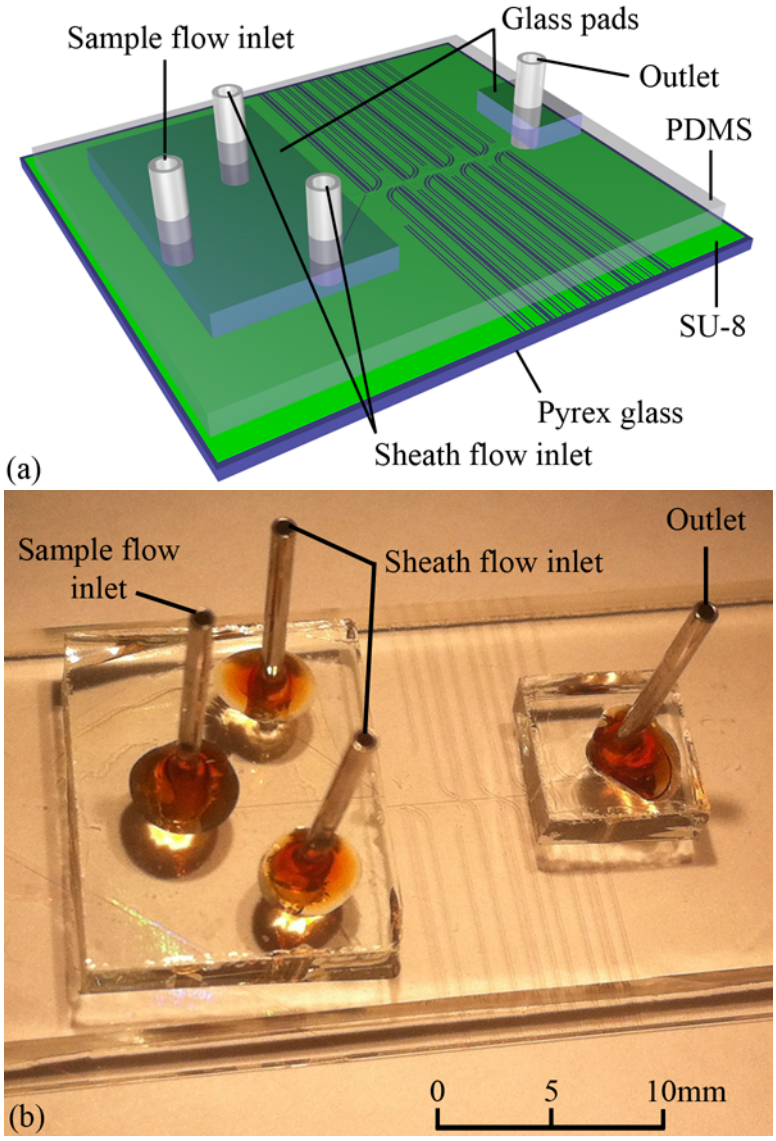


FIGURE 3.1: (a) Three dimensional model of the photonic-microfluidic integrated device; (b) photo of a finished device.

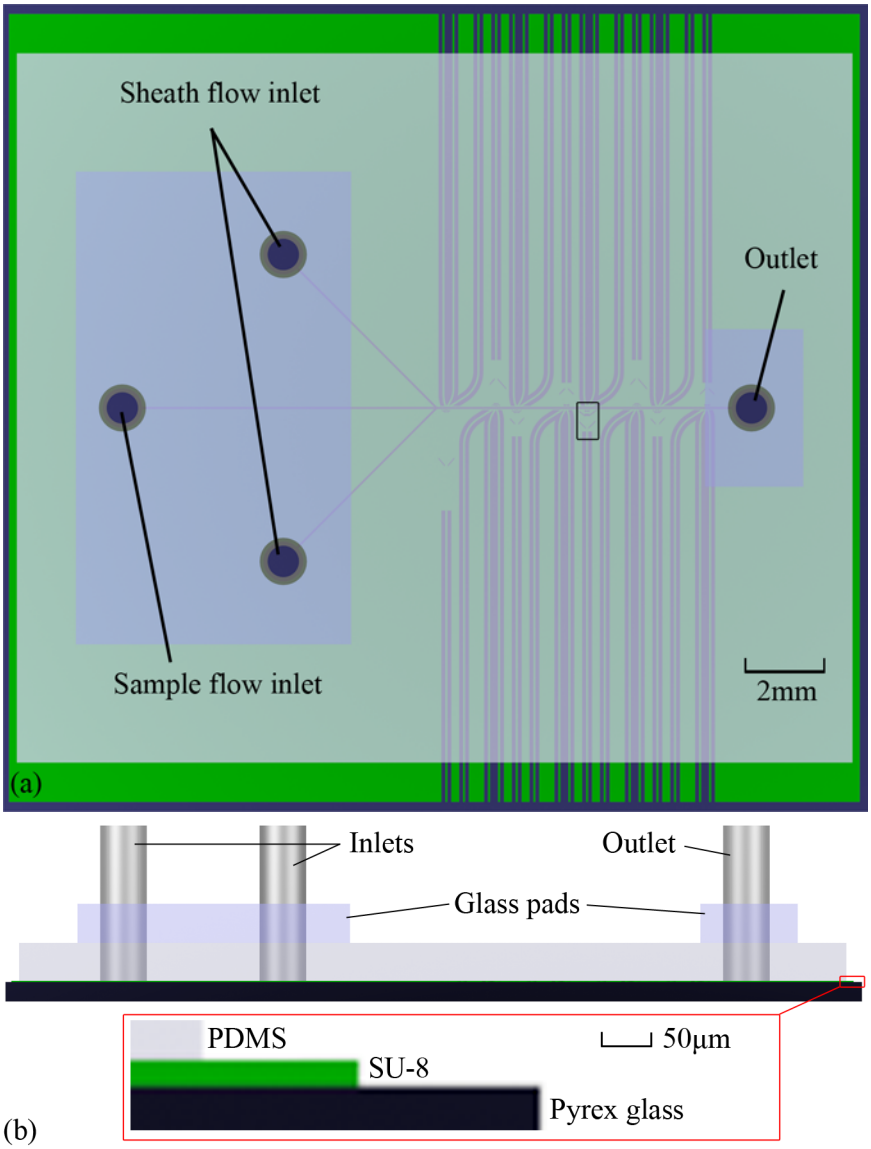


FIGURE 3.2: The top view (a) and front view (b) of the photonic-microfluidic integrated device.

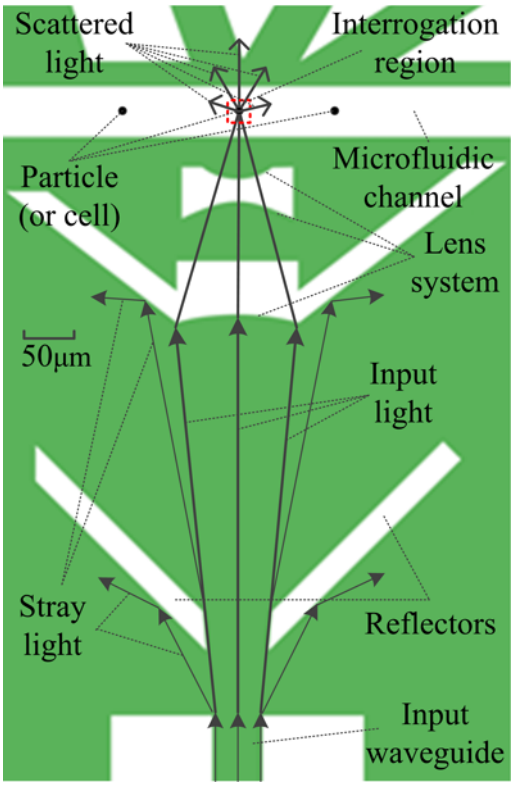


FIGURE 3.3: Magnified view of the area indicated by the rectangle in Figure 3.2(a), showing the optical components and interrogation region in the photonic-microfluidic integrated device.

is removed act as a lens system, focusing the light from the input waveguide to the center of microfluidic channel where particles or bacteria will be interrogated, hence this is termed the interrogation region. Two pairs of reflectors are put on both sides of the input light beam to prevent stray light from entering the interrogation region. Otherwise, such stray light will increase the background noise of the MFC.

## 3.2 Device fabrication

According to the structure of the device, the fabrication process is detailed from the bottom to the top: 1) fabrication of the SU-8 device, 2) device sealing and 3) device packaging.

### 3.2.1 Materials and Equipment

The main materials used to fabricate the device include:

1. Pyrex glass wafers. 4-inch wafers purchased from UniversityWafer (Boston, USA).

2. Epoxy photoresists and developers. SU-8 2035, 3035 photoresists and their developers were purchased from MicroChem Technologies Inc (Newton, USA). SU-8 2025 photoresist is used to form the device layer with functionality structures, while SU-8 3035 serves as an intermediate layer to enhance adhesion between the substrate and the device layer.

3. Positive photoresist. MICROPOSIT S1818 photoresist was purchased from Shipley (Rohm and Haas) (Marlborough, USA), which is used to protect the surface of the SU-8 device layer from damaging during dicing the wafer into parts.

4. Ethanol, isopropyl alcohol and acetone, purchased from a local chemical store at McMaster University.

5. Piranha solution, a mixture of 3:1 concentrated sulfuric acid to 30% hydrogen peroxide solution.

Most equipment used for the device fabrication are provided by the facility of Centre for Emerging Device Technologies (CEDT) at McMaster University, including:

1. Fume hoods for use of volatile solutions such as acetone, ethanol and photoresist developer.

2. Wet bench for wet etch and de-ionized (DI) water rinse.

3. Hotplate and ovens for wafer and photoresist baking.

4. Spinner for coating photoresist films onto substrates.

5. Mask aligner for ultraviolet (UV) light exposure of photoresist.

6. Microscope for inspection on the device quality.

7. Plasma cleaner with nitrogen for surface treatment of PDMS for device sealing.

8. Dicing saw for cutting finished wafers into individual devices.

### 3.2.2 Fabrication of SU-8 device

Multiple SU-8 devices are fabricated by photolithographic (PL) patterning of SU-8 photoresist on a Pyrex glass wafer. The finished wafer is then diced into individual devices using a dicing saw. The fabrication procedure is illustrated in Figure 3.4, including:

1. Wafer preparation.
2. Intermediate layer formation using SU-8 3035 photoresist.
3. Functionality layer formation using SU-8 2035 photoresist.
4. Wafer encapsulation and dicing.

A detailed description of the fabrication procedure is provided in the Appendix A.

### 3.2.3 Device sealing

The SU-8 devices are sealed with PDMS cover slips with through vias aligned with the reservoirs on the device through a reaction between epoxy and amine groups[130].

1. PDMS cover slip preparation.
   (a) PDMS pouring and setting. Mixture of the monomer and curing agent solutions in a ratio of 10:1 is poured into a polystyrene Petri dish and left to set at the room temperature for 24 hours.
   (b) PDMS curing bake. The PDMS is removed from the Petri dish and transferred onto a clean silicon wafer and then placed into an oven at 110℃ for 1 hour for curing.
   (c) PDMS cover slip cutting. The cured PDMS is cut into appropriate dimensions that fit to the size of the SU-8 devices.
   (d) PDMS cover slip punching. PDMS cover slips are punched manually with 0.75mm-diameter holes aligned with all inlets and outlets of the SU-8 device.

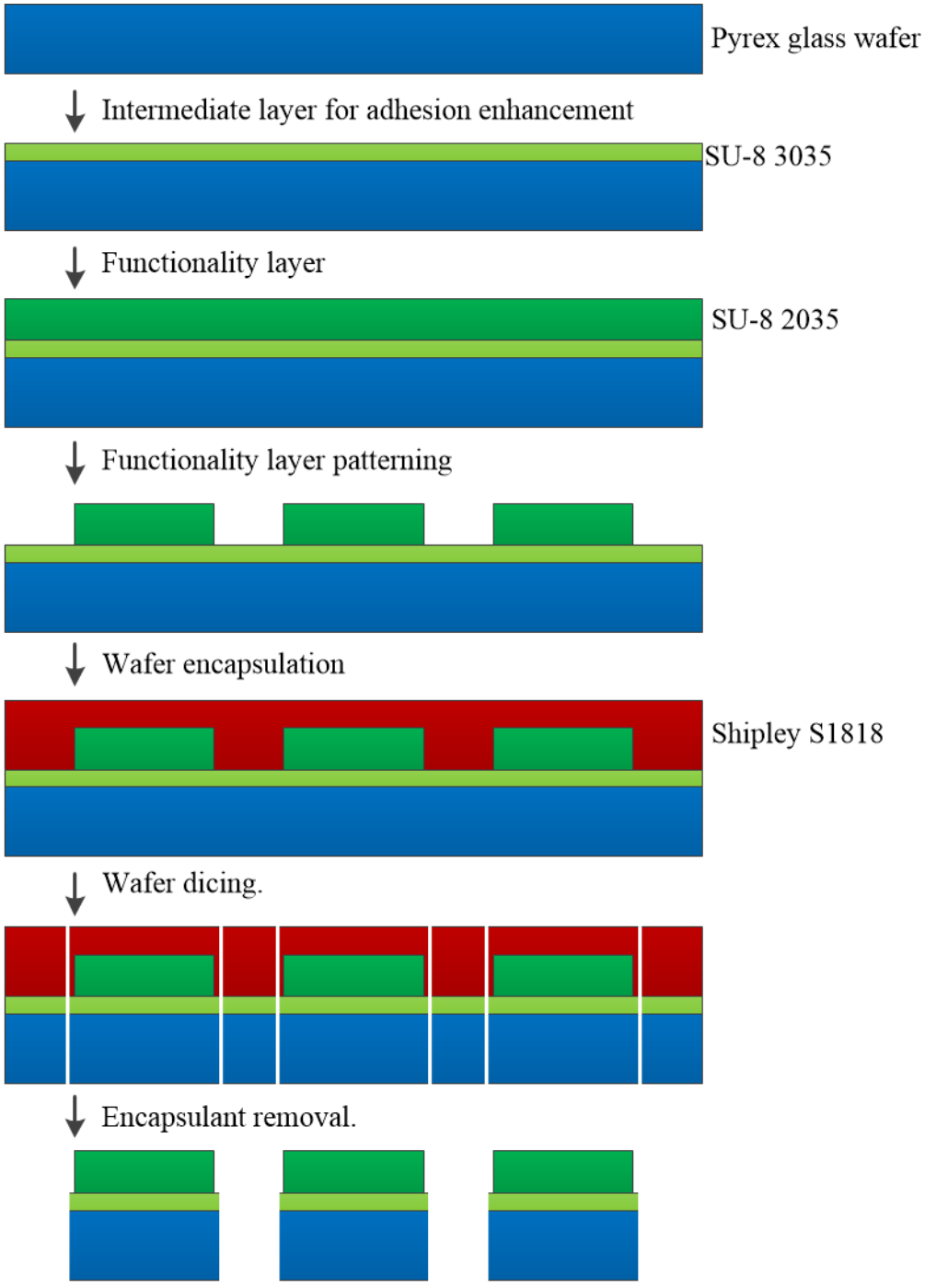


FIGURE 3.4: Fabrication procedure of the SU-8 devices.

(e) PDMS hard baking. The prepared PDMS cover slips are put into an oven at 150℃ for 24 hours to ensure complete crosslinking of monomors.

(f) Nitrogen plasma treatment. The baked PDMS cover slips are placed into a plasma ashing equipment, which is vacuumed to 3–5Pa and then purged with nitrogen of >99.99% purity. After the vacuuming and purging for 10 cycles, the chamber pressure is stabilized to 30–50Pa for the plasma generation. The power used is 100W with <10W reflection. The plasma treatment duration is 4 minutes.

2. SU-8 device surface modification.

   (a) Device preparation. The finished SU-8 devices are placed into an oven, which is vacuumed to about 1000Pa and then purged with pure nitrogen to achieve a pressure of 50000Pa. The devices are kept in the nitrogen environment for 21 hours.

   (b) Device baking. The temperature of the oven is set to 65℃ and the devices are kept in this environment for 5 hours.

3. PDMS/SU-8 bonding. Nitrogen plasma treated PDMS cover slips are placed onto the SU-8 device with PDMS holes in alignment with reservoirs on the device.

4. Bonding activation. The SU-8 devices covered by PDMS slips are placed into an oven at 100℃ to activate and drive the bonding reaction. Pressure is applied to the device to ensure a intact contact between PDMS and SU-8.

### 3.2.4 Device packaging

1. Glass pad drilling. Glass pads are drilled with holes aligned to the PDMS holes using a drill bit of 1.1mm diameter and then cut into dimensions fitting to the PDMS cover slip.

2. Glass pad bonding. Both the glass pads and PDMS top surface are treated with oxygen plasma for 2 minutes. The RF power and chamber pressure for the plasma generation is 100W and 50Pa, respectively. Then glass pads are

immediately placed onto the PDMS surface with alignment of holes in the glass pads and the PDMS slips. Devices are kept in an oven at 100℃ for 1 hour to drive the bonding.

3. Pin insertion and fixing. Hollow metal pins of 22 gauge (i.e., inner diameter of 0.603mm and outer diameter of 0.908mm) are inserted into the PDMS holes. Devices are placed into an oven at 120℃ for 30 minutes. Then epoxy is applied to the pins to fill the void between PDMS, glass hole and pin.

## 3.3 Improvements on fabrication procedure

### 3.3.1 Photolithographic procedure of SU-8 device

The performance of the photonic-microfluidic integrated device relies primarily on the PL quality of SU-8 functionality layer, such as smoothness and verticality of sidewalls of all the integrated components. The thickness of SU-8 2035 layer used in all this work is 30$\mu$m. The mask used for the PL procedure to fabricate SU-8 devices is shown in Figure 3.5, in which (a), (d) and (f) are devices of 20° incident angle, while (b), (c) and (e) are in normal incidence. The mask details are included in Appendix B.

SU-8 2035 is a epoxy based, negative photoresist and sensitive to conventional UV (350–400 nm) radiation. The PL procedure of SU-8 2035 has been detailed in the step 4 of subsection 3.2.2. A strong acid produces in the SU-8 photoresist exposed to UV radiation during the UV exposure step and the epoxy cross-linking is catalyzed by the acid produced and driven thermally during the post-exposure bake (PEB) step. After developing, the exposed SU-8 photoresist remains while the unexposed is dissolved by the SU-8 developer. Therefore, SU-8 photoresist covered by the solid patterns in the mask will be removed, forming microfluidic channels, reservoirs, optical lenses and waveguides. To ensure good quality of the components fabricated, the UV exposure dosage and PEB procedure have to be optimized to achieve smooth and vertical sidewalls. By performing a series of experiments on PL procedure with different UV exposures and PEB profiles, an optimized condition is found, which is $170mJ/cm^2$ for the 30µm-thick SU-8 2035 photoresist layer and a PEB profile of heating up in 1 hour from room temperature to 90℃ and cooling down in 3 hours. The fabricated SU-8 device under the optimized condition is shown in the Figure 3.6.

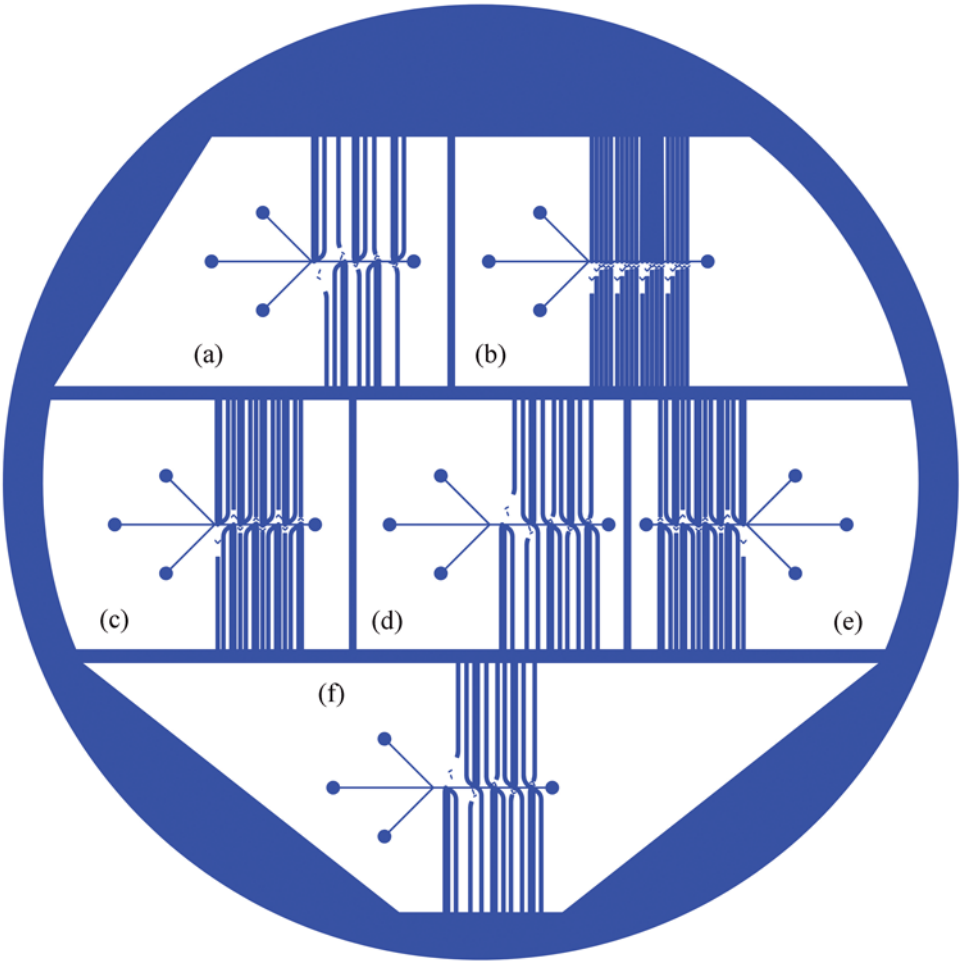


FIGURE 3.5: Photo of a 3-inch mask for PL procedure of the SU-8 device.

In addition, because of the large difference in coefficient of thermal expansion between SU-8 and Pyrex glass, $5.2\times10^{-5}$/℃ and $3.25\times10^{-6}$/℃, respectively, the heating and cooling profiles have a significant impact on the smoothness of the optical components. When the heating and cooling processes are performed rapidly, thermal stress accumulated in the SU-8 can not be released completely, yielding deformations of the patterns. Figure 3.7 shows scanning electron microscope (SEM) graphs of a SU-8 device fabricated by PL procedure with rapid PEB step using hot plate, heating up to 90℃ in 1 minute, holding for 5 minutes and cooling down to 25℃ in 20 minutes.

After the PL process of SU-8 devices on a glass wafer, the glass wafer should be diced into individual devices and the edges should be as close to, but not touching, the end of waveguides as possible to facilitate the light coupling between the input

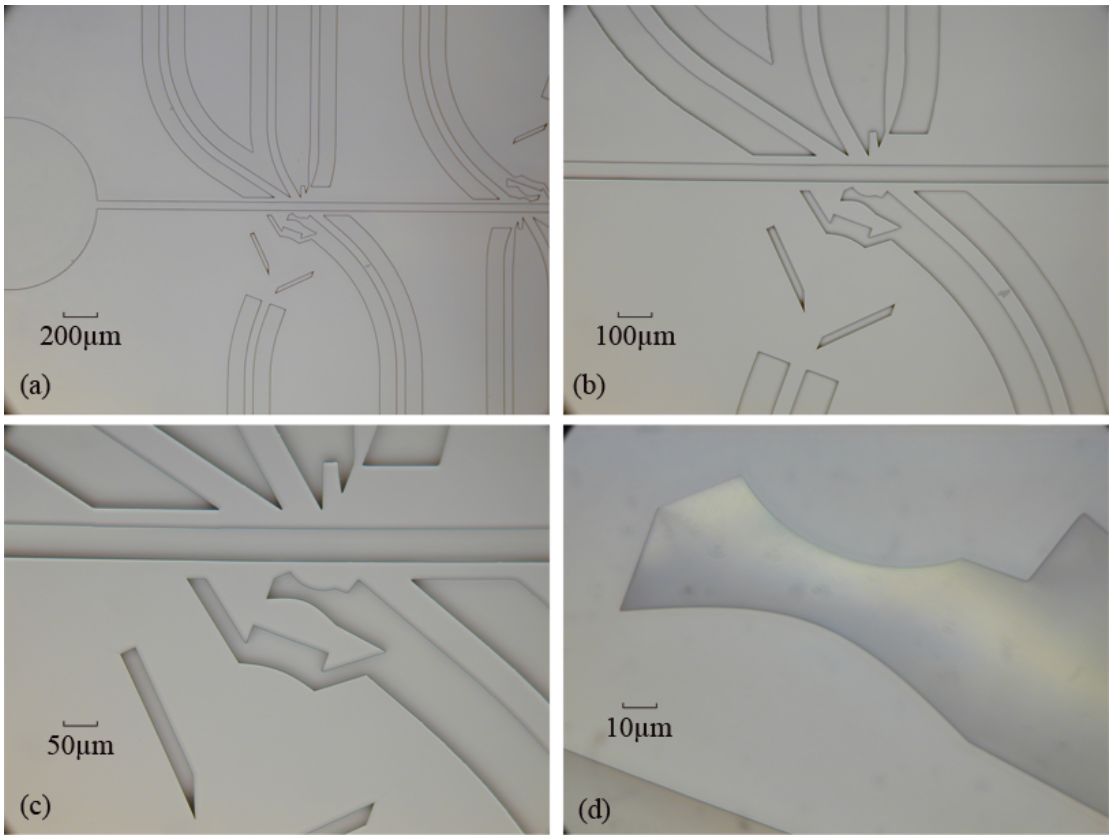


FIGURE 3.6: Photos of the SU-8 device fabricated in the optimized PL condition. (a), (b), (c) and (d) are taken under an optical microscope with magnifications of 50, 100, 200 and 1000, respectively.

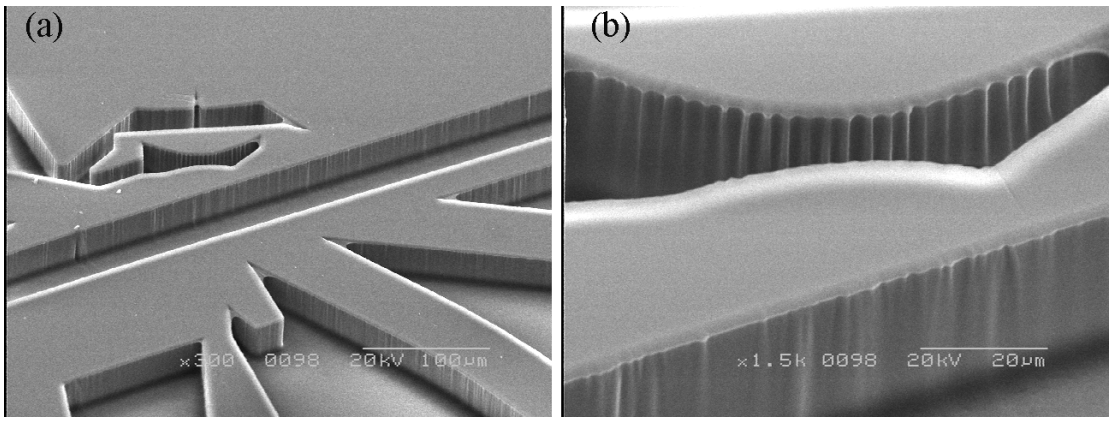


FIGURE 3.7: (a) A SEM graph of a SU-8 device fabricated by PL procedure with a rapid PEB step using hot plate, heating up to 90℃ in 1 minute, holding for 5 minutes and cooling down to 25℃ in 20 minutes. (b) A detailed view of the sidewall of an optical lens.

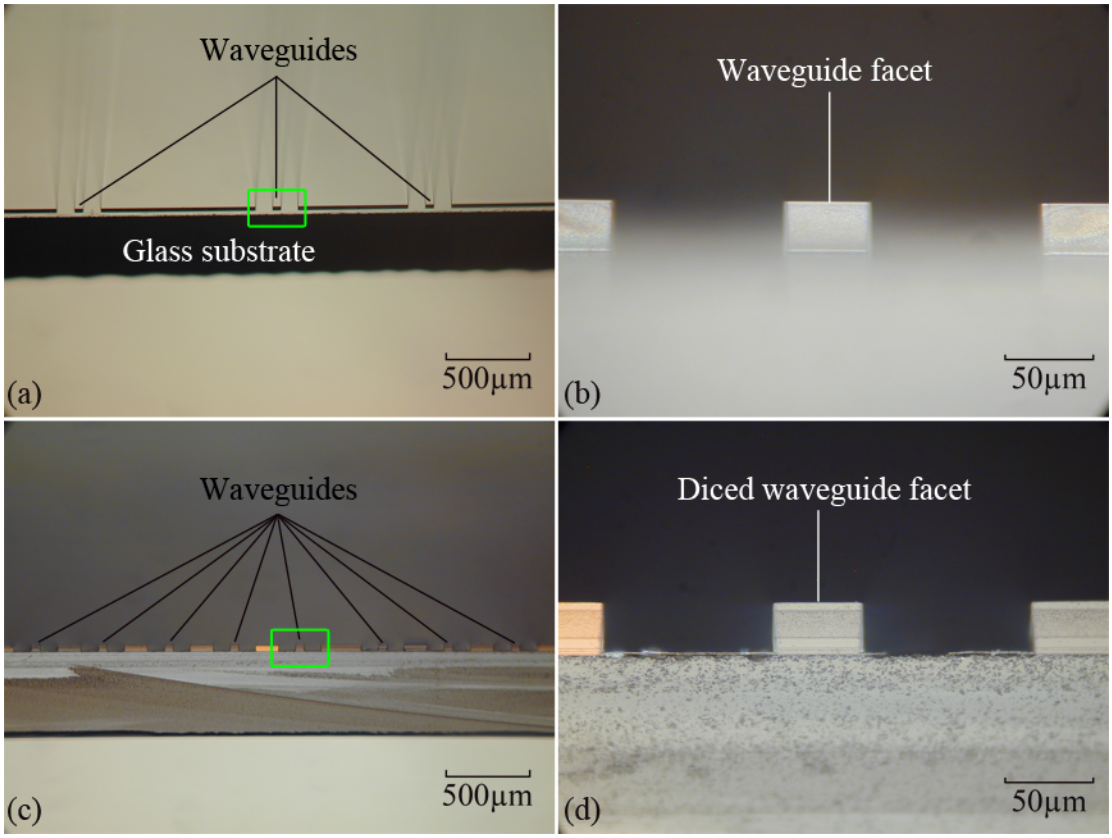


FIGURE 3.8: Photos of the waveguides facets of diced devices, (a, b) for dicing without touching the waveguide, (c, d) for dicing across the waveguide; (b) and (d) are magnified views of the areas indicated by rectangles in (a) and (c), respectively.

optical fiber and the waveguides in the device, as shown in Figure 3.8(a) and (b). A cut crossing the waveguide, as shown in Figure 3.8(b), will results in a rough facet that dramatically reduces the efficiency of coupling light into the waveguide from the input optical fiber.

### 3.3.2 PDMS cover slip fabrication

PDMS cover slips fabricated by procedures described in the subsection 3.2.3 utilizes manual punching to make holes for fluid connections. Although metal pins are inserted carefully into these holes, clogging caused by PDMS debris cannot be avoided completely, which results in limited device lifetime. Figure 3.9 shows a device clogged by PDMS debris.

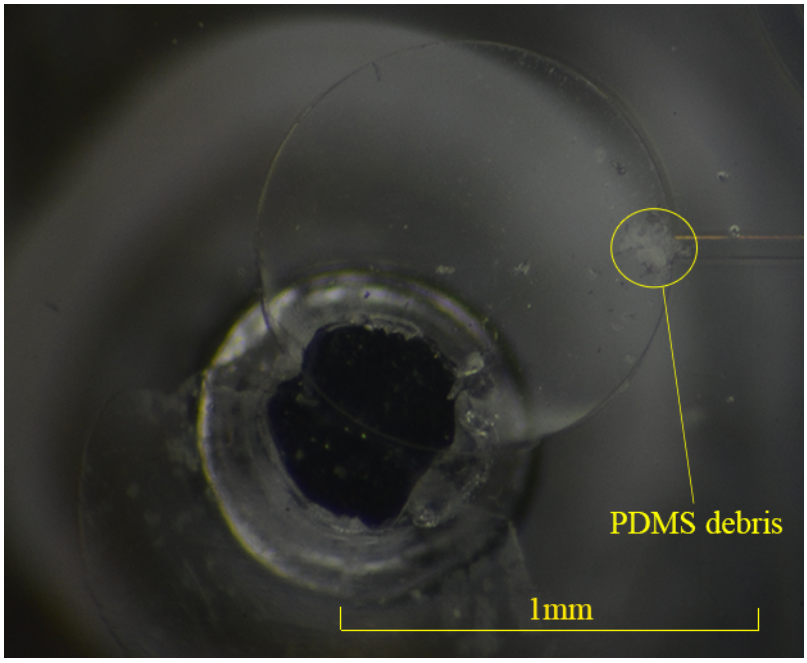


FIGURE 3.9: A device clogged by PDMS debris.

To ensure no PDMS debris clogging, the holes in the PDMS cover slips should not be fabricated using mechanical punching, by which debris is inevitable. Therefore, a mold is created for the PDMS cover slip preparation.

The mold is comprised of two aluminum plates separated by 3 mm. The top plate is drilled with 0.794 mm diameter holes at locations aligned with all inlets and outlets of the SU-8 device, where metal cylinders of the same diameter are inserted with a extrusion height of 3 mm, while the bottom one is a roughly polished aluminum plate. Both plates are then coated with 20µm-thick SU-8 3035 photoresist to ensure the flat surfaces of the mold, as shown in Figure 3.10.

PDMS cover slips fabricated by punching and using the above mold are compared in Figure 3.11, (a)

## 3.4 System setup

The setup of the MFC based on the photonic-microfluidic integrated device is shown schematically in Figure 3.12(a), and a photo of the system excluding the laser source and computer is presented in (b).

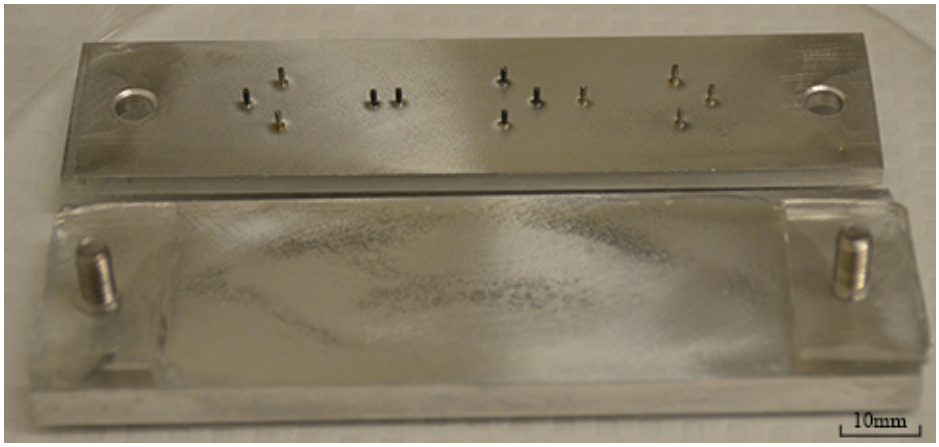


FIGURE 3.10: Photo of the PDMS mold.

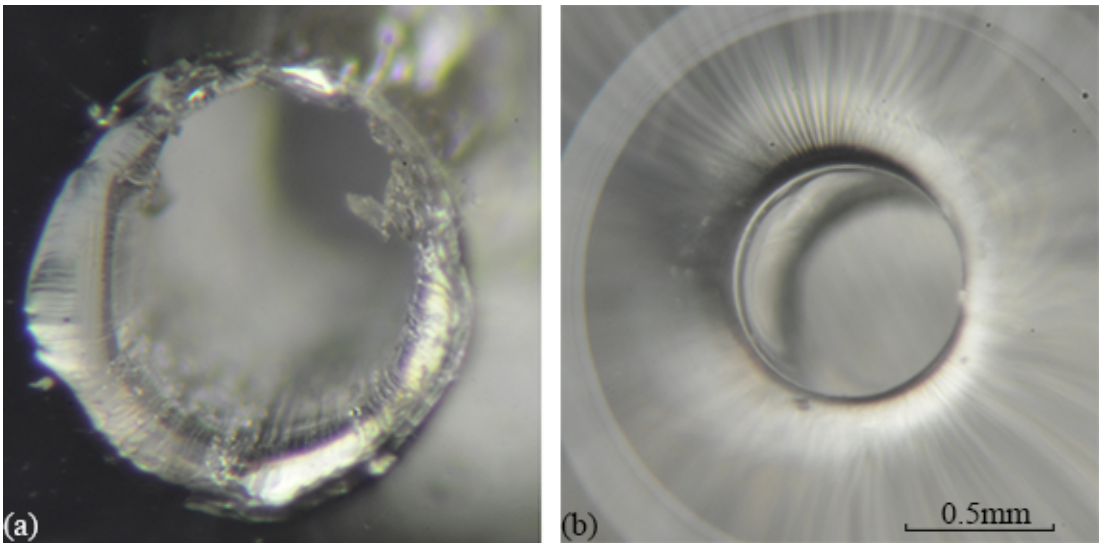


FIGURE 3.11: Comparison of the holes in the PDMS cover slips fabricated by two different methods, (a) by manual punching and (b) by using a mold.

### 3.4.1 Light source and optical coupling

A fiber pigtailed laser of 532nm wavelength (CQ Laser Technologies Co., Ltd., Nanjing, China) is selected to be the light source for the MFC because it features small size, low cost and high performance. This green DPSS laser is selected for the MFC because it features small size, low cost and high performance. The laser emits 532nm continuous wave (CW) with maximum output power of 500mW, which is sufficient for our application.

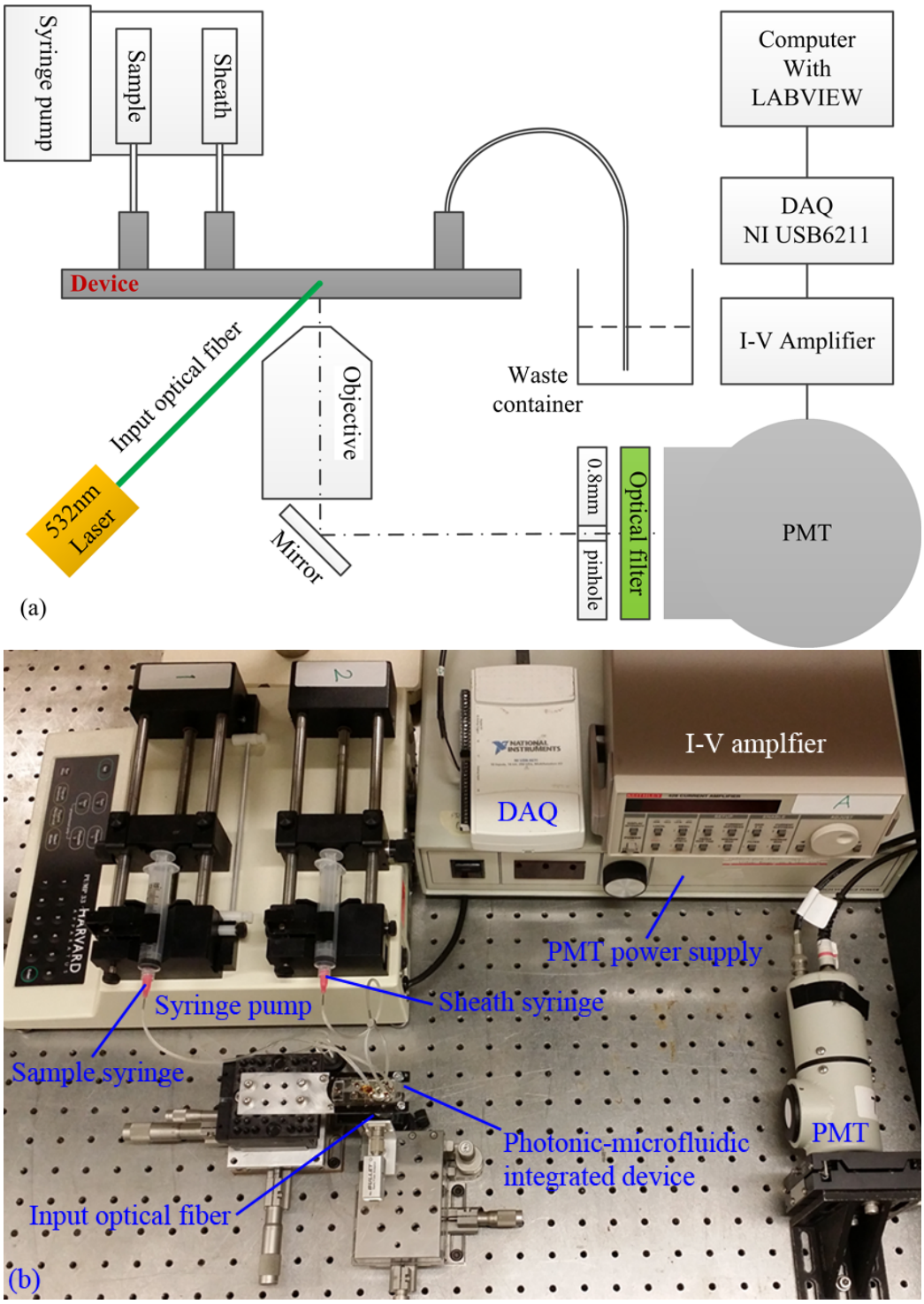


FIGURE 3.12: (a) Schematic view of the system setup of the micro-flow cytometer based on the photonic-microfluidic integrated device; (b) a photo of the system excluding the laser source and computer.

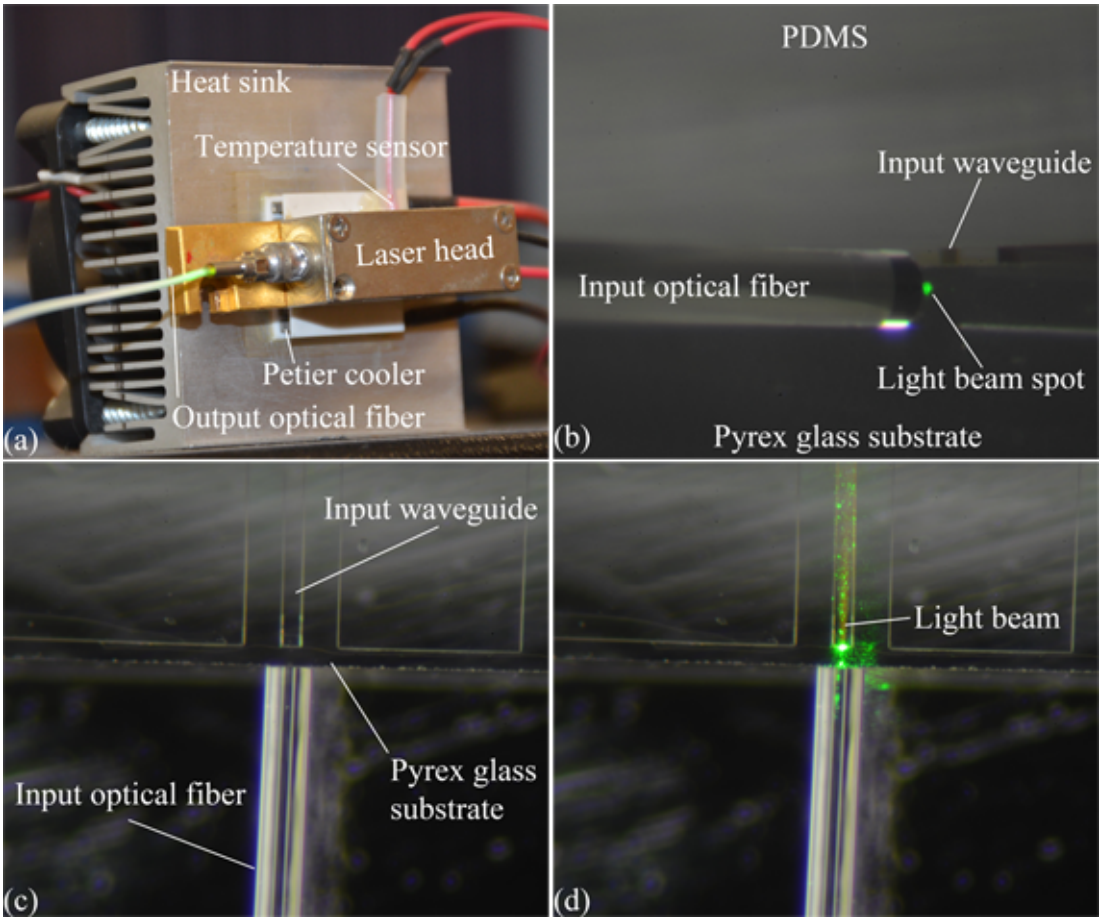


FIGURE 3.13: (a) Photo of the 532nm laser source used in the MFC; (b) Light coupling between the input optical fiber and the input waveguide of the device (light beam spot is shifted intentionally away from the end of the input waveguide); (c) top view of the input light coupling without laser illumination; (d) top view of the input light coupling with laser illumination showing the light beam propagation inside the input waveguide.

Figure 3.13(a) presents a photo of the laser head with temperature controlling components including a Petier cooler, heat sink and fan. It is a diode-pumped solid-state (DPSS) laser that produces 532nm green light by frequency doubling in a periodically poled Lithium Niobate (PPLN) crystal from 1064nm wavelength light generated by pumping a neodymium-doped yttrium orthovanadate (Nd:$YVO_4$) crystal with a high-power 808nm laser diode. Light is coupled into an output optical fiber, which is also called an input optical fiber when referring to the device.

Figure 3.13(b) shows the alignment between the input optical fiber and the device waveguide, in which the input beam spot is intentionally shifted away from the input waveguide for better viewing of the beam spot. To ensure ideal light coupling, the input beam spot should be less than the dimension of waveguide facet. Otherwise, a portion of input light will travel outside the waveguide and thus increase the background luminance of the environment, resulting in decreased signal-to-noise ratio of the MFC. Therefore, the core diameter of the input optical fiber is chosen to be 25$\mu$m because the dimension of the input waveguide facet is 50 by 30$\mu$m in the photonic-microfluidic integrated devices used in this work. After the fiber and waveguide are alignment, two photos show the top views of the optical coupling without and with the illumination of laser source in Figure 3.13(c) and (d), respectively. It is evident that the input light enters the waveguide and is confined inside. A bright spot is seen on the waveguide facet because the shutter duration of the camera is set quite long to ensure sufficient exposure for good viewing of the light beam inside the waveguide even when the facet reflects a small portion of input light into the camera.

### 3.4.2 On-chip beam shaping

Light from the input optical waveguide is focused onto the center of the microfluidic channel by the on-chip lens system, as shown by the microscopic photo in Figure 3.14. Theoretically, it is hard to see the input light beam under a microscope from the top because the input light travel inside the SU-8 photoresist layer and no light can be collected by the camera. Therefore, a device of poor quality is selected intentionally to view the on-chip beam shaping, which has relatively rough interface between the SU-8 photoresist and PDMS layers, enabling leaking of the input light for image capture. In addition, because the sidewalls of the patterns on the SU-8 photoresist are not exactly vertical to the substrate, bright spots will appear when the input light is reflected upwards and collected by the camera. However, although there are two bright spots on both sides of the microfluidic channel near the interrogation region, they will be rejected by a spatial filter in the light collection system. Therefore, there is little influence on the performance of the MFC.

Details on the beam shaping had been reported in previous publication[131, 132].

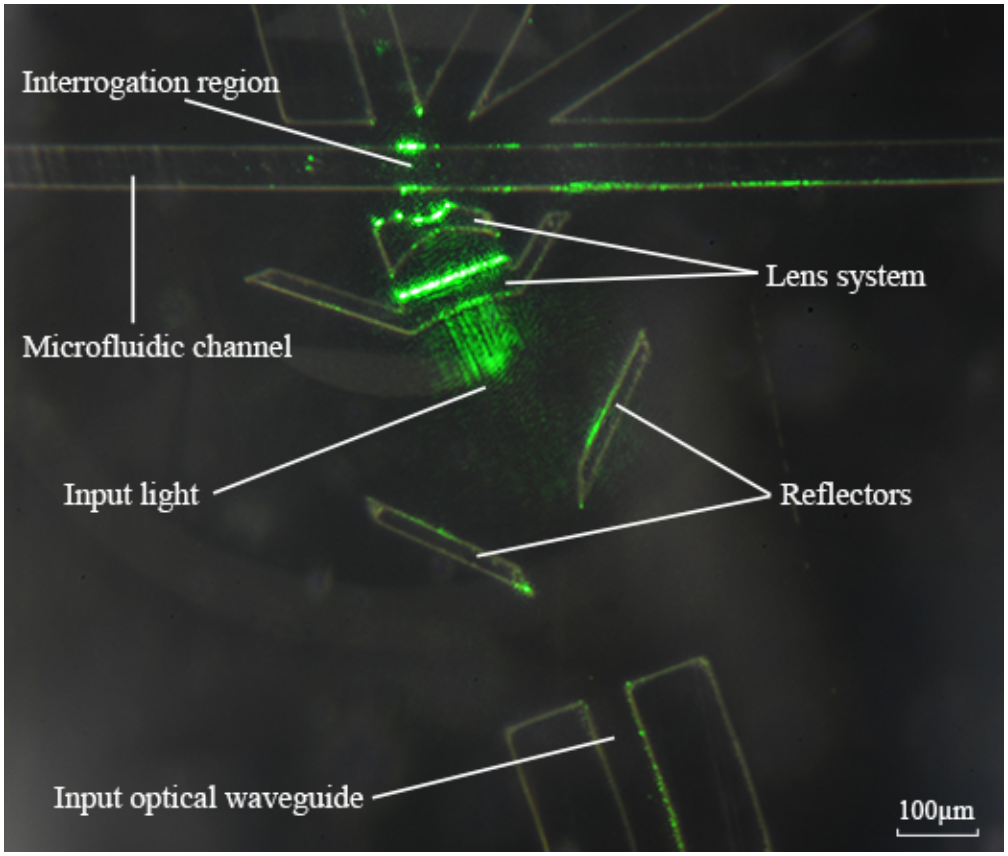


FIGURE 3.14: Photo of light beam shaping by the on-chip lens system in a photonic-microfluidic integrated device.

### 3.4.3 Side-scattered light collection and detection

Side-scattered (SSC) light produced when a particle passes through the interrogation region is collected by a microscope objective positioned under the photonic-microfluidic integrated device, as shown in Figure 3.15(a). A mirror is placed under the objective to change the optical axis from vertical to horizontal for the ease of component arrangement on the optical table. Through this microscope objective, the functionality layer (SU-8) is imaged onto the plane where the pinhole is placed, as shown in Figure 3.15(b). The center of pinhole is aligned with that of the interrogation region. An optical filter with a passband of 522-542 nm is attached onto the other side of the pinhole, which is mounted onto the entrance of a photo multiplying tube (PMT). The portion of SSC light passing through the pinhole and optical filter

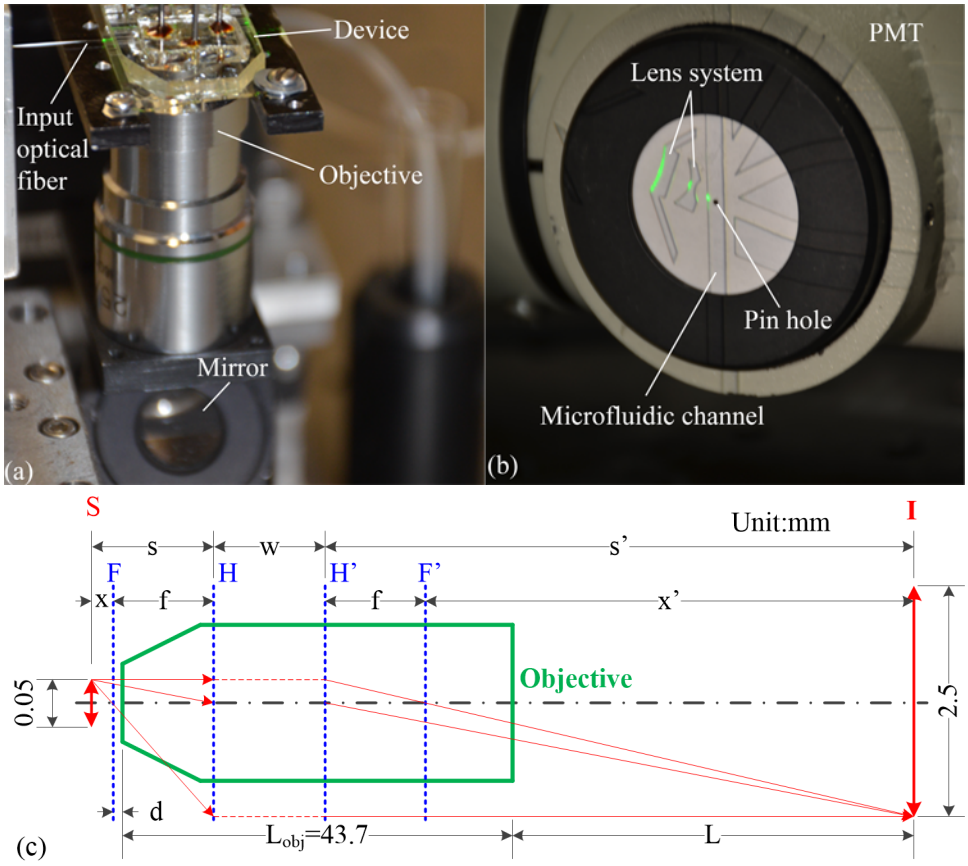


FIGURE 3.15: (a) Photo of the SSC light collection using a microscope objective positioned under the device; (b) Image of the device functionality layer on the plane where the pinhole is placed; (c) Equivalent optical diagram of the SSC light collection, in which the mirror is ignored.

is detected by the PMT and converted to electric current, which is further amplified by an I-V amplifier to voltage signals for digitization.

The objective used in the MFC is a standard microscope objective with a magnification factor of 25, a working distance of 1.3mm and a numerical aperture of 0.4. However, the objective is configured with less working distance than its specification to achieve a magnification of 50. The equivalent optical diagram of the SSC light collection is shown in Figure 3.13(c), including the principal planes (H and H') and focal planes (F and F') of the objective with a focal length of $f = 6.275mm$ and a principal plane spacing of $w = 2.259mm$. The distance between object focal point the entrance of objective, $d$, is about 0.66mm. When $x$ and $L$ are set to be 0.125mm

and 285mm, respectively, a 50 times magnified image of the SU-8 layer is focused onto the pinhole, as shown in Figure 3.13(b).

# Chapter 4

# Characterization of the Micro-Flow Cytometer

The micro-flow cytometer based on the photonic-microfluidic integrated device is designed to count the total number of bacteria in certain volume of water and then the concentration of bacteria can be extracted from the slope of throughput versus sample flow rate. In this chapter, standard micro-sized beads are used to mimic bacteria for the performance characterization of the micro-flow cytometer. Hydrodynamic focusing by sheath flows is used to confine the sample stream in the microfluidic channel, which is simulated by software simulation using COMSOL multiphysics and compared with experimental results. Finally, a high accuracy of over 96% is achieved for counting beads using customized data analysis in the MFC[133].

## 4.1 Sample preparation

Highly uniform blank polystyrene beads (Invitrogen, Burlington, ON, Canada) with a diameter of 2$\mu$m (2.00$\pm$0.04$\mu$m) are used to characterize the performance of micro-flow cytometer. A series of samples with different concentrations from $2\times10^4$ to $1\times10^6$ beads/mL are diluted from beads with an original concentration of $3\times10^7$ beads/mL by adding de-ionized (DI) water. Because the density of polystyrene beads is 1.055 $g/cm^3$ and the beads settle out within minutes in water, suspensions must be uniformly suspended by vortex mixing and sonicating before diluted. After transferring the sample suspensions into the sample syringe for testing in the micro-flow cytometer, the sample syringe with connected tube is removed from the system and sonicated every 5 minutes to ensure that beads in the sample syringe are suspended uniformly and thus the concentration of sample flow is constant during the testing period.

## 4.2 Hydrodynamic focusing

### 4.2.1 Simulation of hydrodynamic focusing

Hydrodynamic focusing is a technique used widely in flow cytometry to accurately control the position and dimension of the microfluidic tunnel that samples pass

through by building up the walls of tunnel from two fluid flows, which is together called the sheath fluid. The sample fluid containing particles or cells to be tested is injected into the middle of the sheath fluid comprised of two flows on both sides of the sample flow, as shown in Figure 4.1(a). In this work, the flows are configured symmetrically, i.e., the two sheath flow rates are identical, hence the focused sample stream is a ribbon in the center of the channel.

Although relationship between the width of focused sample stream and the ratio of sample flow rate versus total sheath flow rate had been calculated theoretically [134], the sample fluid was considered as a solution, not a suspension of particles. The mechanism of hydrodynamic focusing of particles is different from that of a solute such as fluorescent molecules. This is because the motion of particles is driven by the drag force due to friction between water and particles and governed by Newtonian equation, whereas the other is by the convection-diffusion equation. Therefore, the hydrodynamic focusing of particles is simulated using COMSOL Multiphysics software to determine the relationship between the width of focused sample stream of particles ($w_{fssp}$) and the ratio of sample to total flow rate($FR_{sample}/FR_{total}$).

In practice, $w_{fssp}$ is the dimension of particle distribution along y axis when they pass through the interrogation region. Therefore, the motion of particles in the microfluidic channel is simulated using COMSOL multiphysics software and their trajectories are calculated to determine the focused sample stream width. Figure 4.1 shows the 3D view and its top view of the structure used for the simulation. The height (along z axis) of all channels is 30$\mu$m.

In the simulation, two physical studies are performed successively. 1) Calculate the flow velocity field using the laminar flow interface under the single-phase flow branch of the fluid flow module. 2) Trace the motion of particles using the particle tracing for fluid flow interface, in which drag force to the particles from the fluid is taken into account.

The equations solved by the laminar flow interface are the Navier-Stokes equation for conservation of momentum (Equation 4.1) and the continuity equation for conservation of mass (Equation 4.2). Both are under stationary conditions.

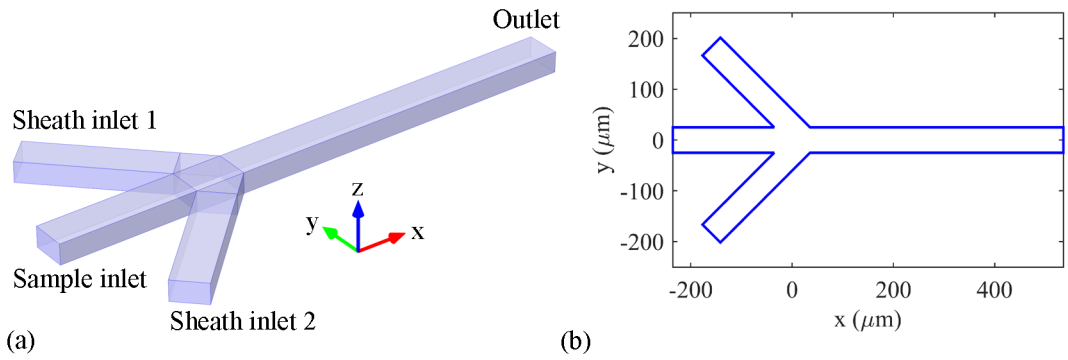


FIGURE 4.1: Structure for simulation of the hydrodynamic focusing, (a) 3D view and (b) top view.

$$\rho(\vec{u}\cdot\nabla)\vec{u} = \nabla\cdot[-p\overleftrightarrow{I} + \mu(\nabla\vec{u} + (\nabla\vec{u})^T)] + \vec{F} \tag{4.1}$$

$$\nabla\cdot(\rho\vec{u}) = 0 \tag{4.2}$$

where $\rho$ denotes the mass density of the fluid, $\vec{u}$ is the flow velocity field of the fluid, $\nabla$ is the gradient operator, $p$ is the scalar field of pressure, $\overleftrightarrow{I}$ is the identity second-order tensor, $\mu$ is the dynamic viscosity of the fluid, and $F$ is the external force applied to the fluid.

The boundary conditions for the sample inlet and the sheath inlets are laminar inflow with fixed flow rates, $FR_{sample}$ and $FR_{sheath}$, respectively. The boundary condition for the outlet is set to be zero pressure relative to the reference pressure of 1 atm, and the fluid velocity at all other walls is zero.

The flow velocity field of water is firstly calculated under $FR_{sample} = 33\mu L/hour$ and $FR_{sheath} = 330\mu L/hour$, which means a 1/10 ratio of sample to sheath flow rate. The results are shown in Figure 4.2, where the sliced view at different cross-sections along the flow paths is presented in (a) and other detailed views are shown in (b-e), xy-plane view at z = 0$\mu$m, yz-plane view at the outlet, u versus z at y = 0$\mu$m and u versus y at z = 0$\mu$m at the outlet, respectively. Figure 4.2(b) shows that the fluid velocity becomes constant along x-axis after the junction area and (c) demonstrates that the fluid in the center flows at maximal velocity while the fluid velocity is zero on

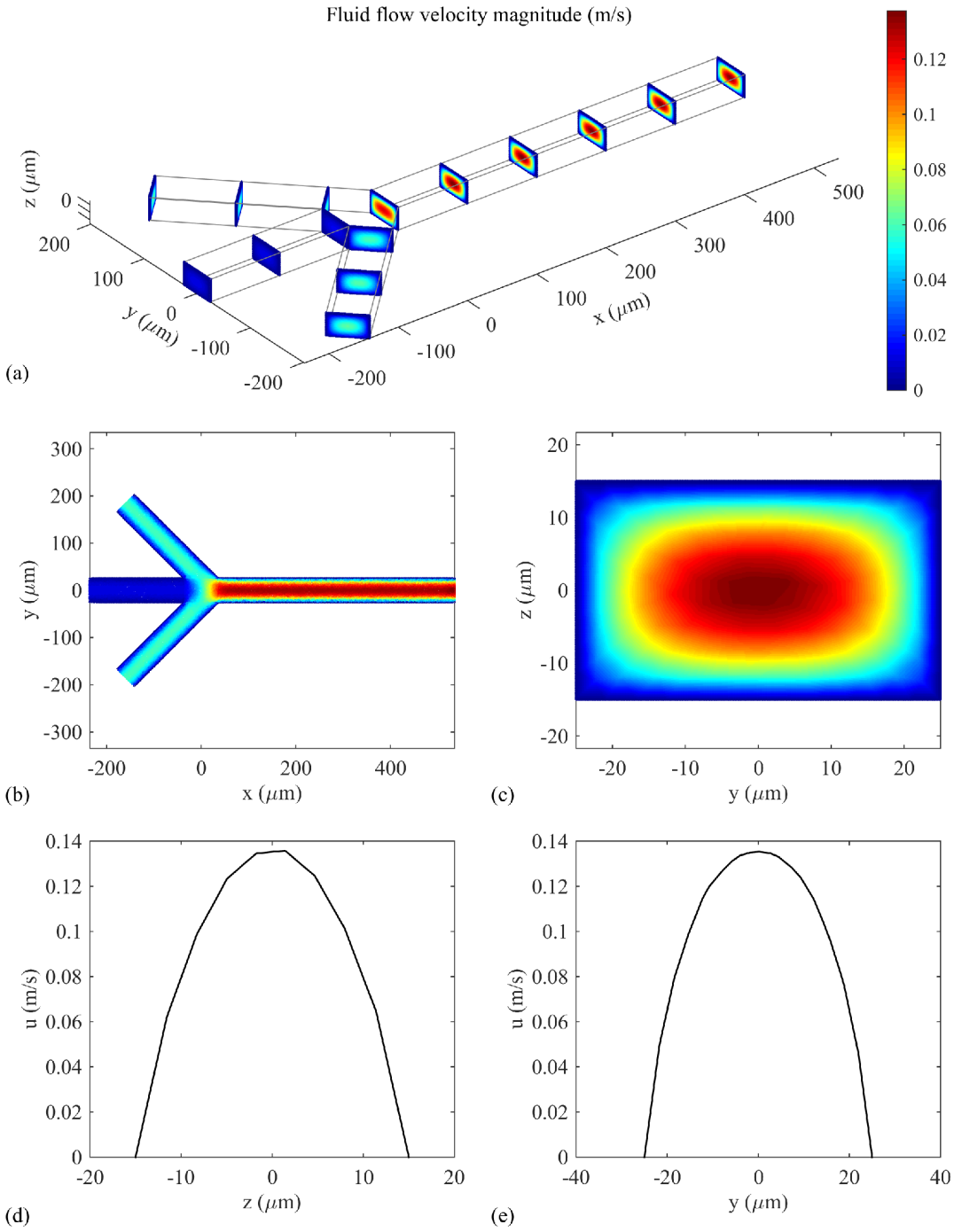


FIGURE 4.2: Simulated fluid flow velocity magnitude field, u, in the hydrodynamic focusing structure, (a) sliced views in 3D, (b) xy-plane view at z=0$\mu$m, (c) yz-plane view at the outlet, (d) u versus z at y = 0 at the outlet, (e) u versus y at z = 0 at the outlet.

all the boundaries. Figure 4.2(d) and (e) indicate the fluid velocity follow parabolic distribution on both y-axis and z-axis.

The results from the simulation above are fed into the particle tracing interface, which solves the Newtonian equation of motion with time dependence (Equation 4.3).

$$\frac{d(m_p\vec{v})}{dt} = \vec{F} \tag{4.3}$$

$$\vec{F} = \frac{1}{\tau_p} m_p(\vec{u} - \vec{v}) \tag{4.4}$$

where $d$ denotes the derivative operater, $m_p$ is the particle mass, $\vec{v}$ is the velocity field of a particle, $\vec{F}$ is total force applied to a particle, $\vec{u}$ is the velocity field of the fluid, $\tau_p = \rho_p d_p^2/18\mu$ is a constant derived from Stokes's law, in which $\rho_p$ and $d_p$ denotes the mass density and the diameter of the particle, respectively. To determine the particle distribution in the channel, 10,000 particles are released initially with a density proportional to the velocity magnitude of the fluid flow at the sample inlet. The boundary conditions for all other walls and the outlet are "freeze", i.e., $\vec{v} = \vec{v_c}$ where $\vec{v_c}$ is the particle velocity when striking the wall or the outlet.

All the symbols used in the simulations and equations are listed in Table 4.1.

The simulation of the particle trajectories is shown in Figure 4.3, where (a) and (b) present the Poincaré maps of the particle trajectories at multiple slices in 3D view and in top view, respectively, showing that particles are gradually focused into the center when moving along the microfluidic channel; (c) shows the Poincaré map at the outlet to demonstrate the particle distribution in the focused sample stream; (d) and (e) are the projections of the points in (c) along z-axis and y-axis, respectively, to show the particle distribution at each axis. From this simulation result, we can see that all particles will be focused in the center of the channel and distributed uniformly on the y-axis (Figure 4.3(e)) but quadratically on the z-axis (Figure 4.3(d)), which means most particles pass through the interrogation region in the center of the channel, but a portion of them pass at the top and bottom. Therefore, the width of focused sample stream is defined by the width of particle distribution on y-axis, which is

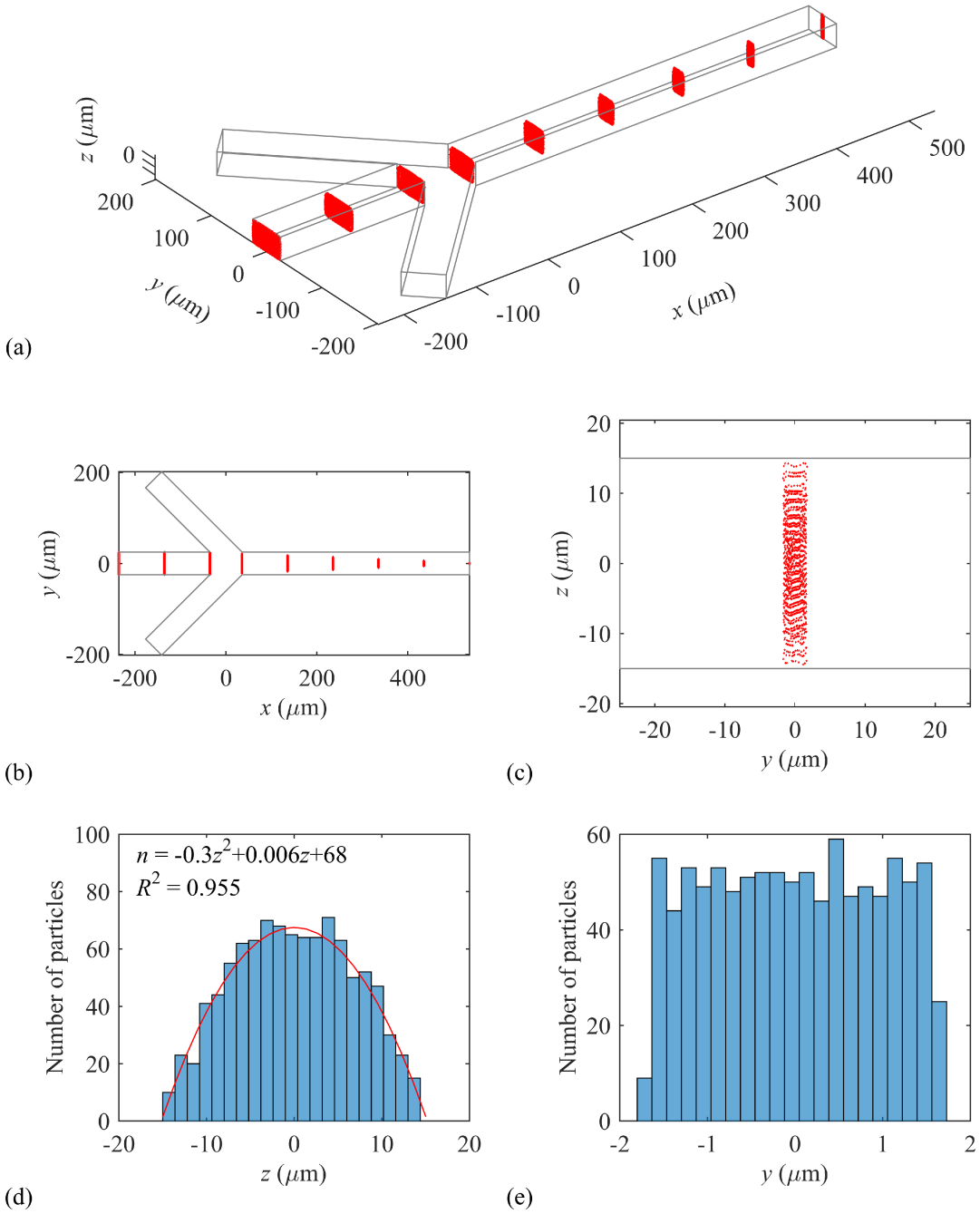


FIGURE 4.3: (a) Poincaré maps of the particle trajectories at multiple slices in 3D view, (b) top view of (a), (c) Poincaré map at the channel outlet and its projection on z-axis (d) and on y-axis (e).

TABLE 4.1: Listing of all the symbols used in the simulations and equations.

| Symbol | Denotation |
|---|---|
| $\rho, \rho_p$ | mass density of the fluid and particles, respectively |
| $m_p$ | mass of the particles |
| $d_p$ | diameter of the particles |
| $\vec{u}, \vec{v}$ | velocity field of the fluid and the particles, respectively |
| $u, v$ | amplitude of $\vec{u}$ and $\vec{v}$, respectively |
| $u_{avg}, v_{avg}$ | average of $u$ and $v$, respectively |
| $\nabla$ | gradient operator |
| $\overleftrightarrow{I}$ | identity second-order tensor |
| $p$ | pressure field of the fluid |
| $\mu$ | dynamic viscosity of the fluid |
| $\vec{F}$ | external force |
| $w_{fssp}$ | width of the focused sample stream of particles |
| $D$ | width of the microfluidic channels along y-axis |
| $h$ | half height of the microfluidic channels along z-axis |
| $A$ | cross-sectional area of the microfluidic channels |
| $\tau$ | transit time of each particle |
| $FR_{sample}$ | volumetric flow rate of the sample fluid |
| $FR_{sheath}$ | volumetric flow rate of the sheath fluids at the sheath inlets 1 and 2 |
| $FR_{total}$ | $FR_{sample} + FR_{sheath}$ |

3.4$\mu$m (Figure 4.3(e)) for the ratio of sample to sheath flow rate at 1:10. It is worth noting that the particles are considered as points here, but their dimensions should be taken into account when calculating the width of focused sample stream. Therefore, the actual $w_{fssp}$ will be the projection width along y-axis of all the particles plus two times of the particle radius, i.e., $w_{fssp}$ is 5.4$\mu$m for the results shown in Figure 4.3(e).

$$w_{fssp} = D\frac{FR_{sample}}{1.37(FR_{sample} + FR_{sheath})} + d_p \tag{4.5}$$

The relationship between $w_{fssp}$ and $FR_{sample}/FR_{total}$ is determined by simulations on different ratios of $FR_{sample}/FR_{sheath}$ from 0.1 to 1 at a constant total flow rate constant at 363$\mu L/h$. Figure 4.4 shows a linear dependence of $w_{fssp}/D$ on $FR_{sample}/FR_{total}$, where $D$ denotes the width of microfluidic channel (along y-axis). The intercept with y-axis at 0.035 is due to the particles diameter ($d_p$) of 2$\mu$m. Therefore, the relationship can be concluded to equation (4.5).

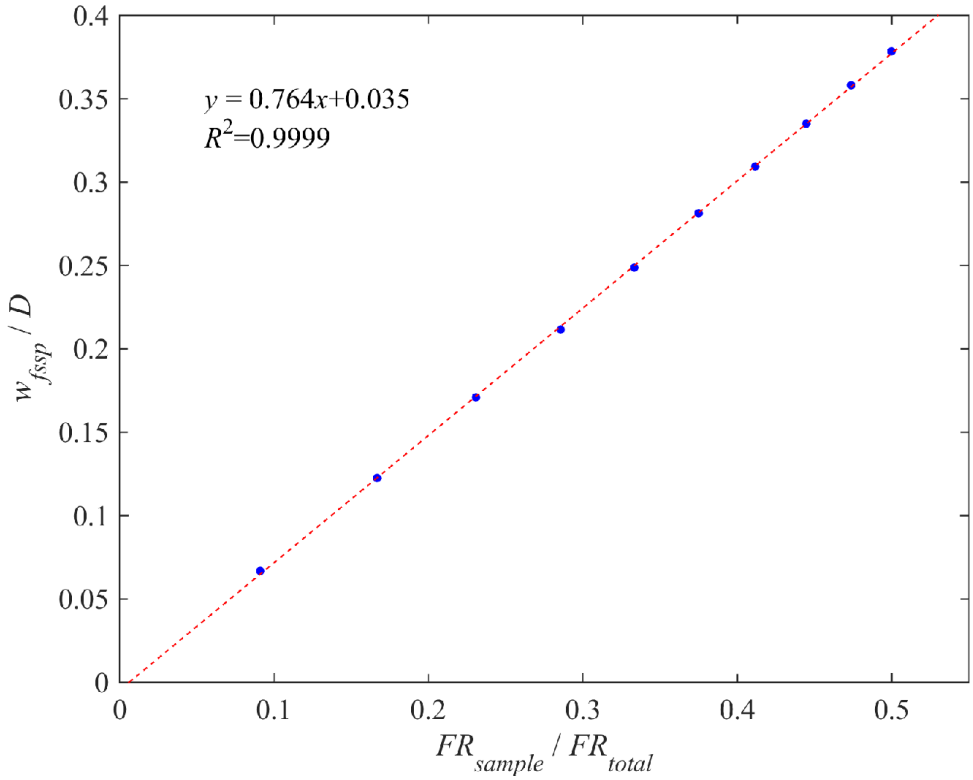


FIGURE 4.4: Dependence of the ratio of width of focused sample stream of particles ($w_{fssp}$) to the microfluidic channel width ($D$) on the ratio of sample to total flow rate ($FR_{sample}/FR_{total}$).

The calculation of $w_{fssp}$ relies on the assumption that particles are distributed uniformly along y-axis, which is valid only when the fluid flow velocity is low (i.e., $FR_{total}$ is low). However, the particle distribution pattern will deform when the average fluid flow velocity ($u_{avg}$) increases as $FR_{total}$ increases when the cross-sectional dimensions of the microfluidic channel are fixed. Therefore, simulations are performed at a fixed $FR_{sample}/FR_{sheath}$ with different $u_{avg}$ to find the range of $u_{avg}$ in which the assumption is valid. Figure 4.5 shows the Poincaré maps of particle trajectories at the channel outlet at a fixed $FR_{sample}/FR_{sheath}$ of 1/10 with different average fluid flow velocities, labeled by (a) to (j), respectively. It is evident that the particle distribution is uniform along y-axis when the $u_{avg}$ is less than $0.336m/s$ and changes gradually to a hyperbolic shape when the $u_{avg}$ increase from 0.336 to $0.672m/s$. Because the particles distribution is non-uniform along the y-axis when $u_{avg}$ is larger than $0.336m/s$,

the $w_{fssp}$ is defined as the projection width along y-axis of 95% particles surrounding their centroid plus $d_p$. The calculated $w_{fssp}$ is plotted versus $u_{avg}$ by the circles with a dashed line in the Figure 4.6, which shows a relatively constant $w_{fssp}$ when $u_{avg}$ is less than 0.27m/s and a slightly expanding stream with increasing $u_{avg}$ above 0.27m/s.

### 4.2.2 Comparison between simulation and experimental results

The simulations are compared with experimental results reported by Mu, et al [91]. The authors used a camera to acquire the images of 1.9$\mu$m fluorescence-labeled beads under hydrodynamical focusing at a constant $FR_{sample}/FR_{sheath}$ of 1/10 with $FR_{sample}$ varying from 30 to 150 $\mu$L/hour (equivalent to $FR_{total}$ from 330 to 1650 $\mu$L/hour or $u_{avg}$ from 0.092 to 0.458 $m/s$), showing a focused narrow stream after the joint part of sample and sheath flows. Their measurements demonstrated that a $w_{fssp}$ of about 5.5$\mu$m is achieved in a 50$\mu$m-wide PDMS channel, as shown by the dots with solid line in the Figure 4.6. The difference between the simulation and experiment results on the $w_{fssp}$ is less than 1$\mu$m, which demonstrates that the simulations are in good agreement with the experiments and hence are reliable and accurate.

## 4.3 Data collection and analysis

Low light signals are converted and amplified to electrical currents by using a photomultiplier tube (PMT), which are further amplified to voltage signals using a I-V amplifier, as shown in Figure 3.12. Voltage signals are then digitized by a data acquisition (DAQ) device (NI DAQmx USB-6211) and recorded using a customized LabVIEW (Laboratory Virtual Instrument Engineering Workbench) program, which integrates MATLAB (Matrix Laboratory) scripts for data analysis in real time.

### 4.3.1 Data collection using LabVIEW

LabVIEW is powerful platform and development environment for system design using a visual programming language from National Instruments. Labview includes extensive support for interfacing to devices and instruments, such as the data acquisition device used in this micro-flow cytometer, NI DAQmx USB-6211, which features a 16-bit analog-to-digital converter with a maximum sampling frequency of 250kHz.

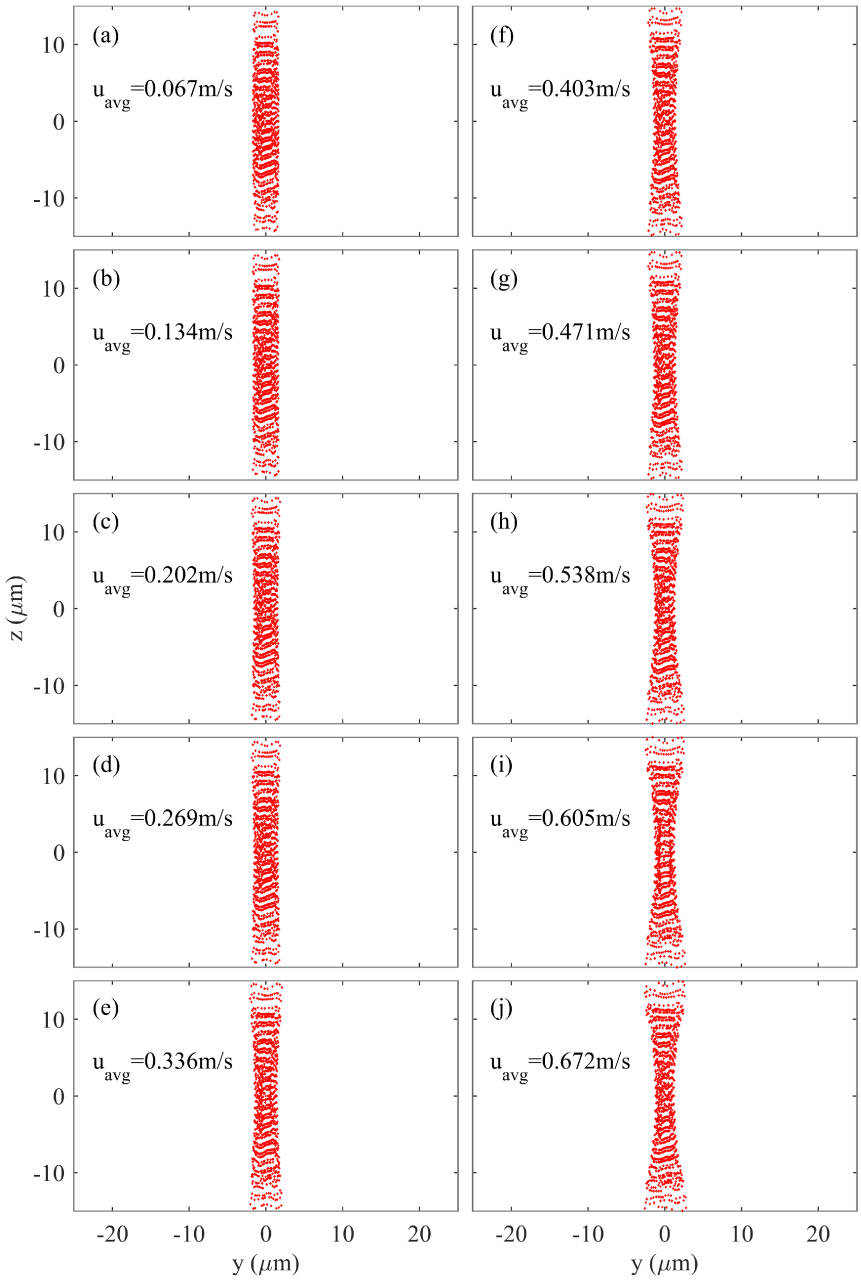


FIGURE 4.5: Poincaré map of particle trajectories at the channel outlet at a fixed $FR_{sample}/FR_{sheath}$ of 1/10 with different average fluid flow velocities ($u_{avg}$), labeled by (a) to (j), respectively.

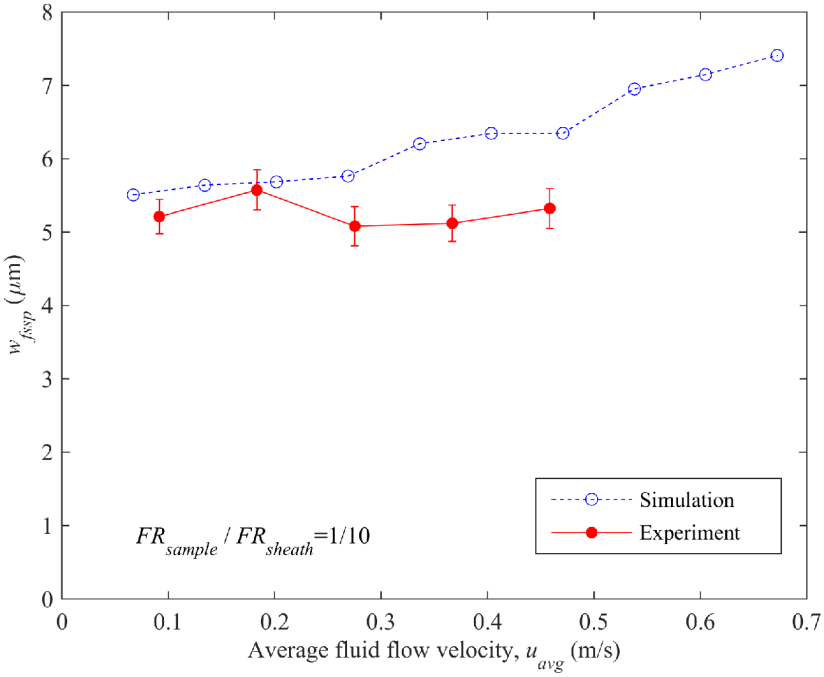


FIGURE 4.6: Comparison between the simulation (circles with dashed line) and experimental result in Reference [91] (dots with solid line) on the $w_{fssp}$ at a constant $FR_{sample}/FR_{sheath}$ of 1/10 with different average flow velocities, $u_{avg}$.

A customized LabVIEW program is designed to automate the data collection and analysis as well as storage of both raw data and processed data. It can also display the waveform of all data in real time, allowing the user to abort the data collection if abnormal situations occur. Figure 4.7 and 4.8 show the front panel and block diagram of the LabVIEW program. The DAQ device is configured for continuous sampling with a large buffer for temporary data storage, allowing for analyzing data in successive segments and display the processed data in real time.

There are 4 input parameters to set up the data collection and analysis, labeled by "Sampling frequency", "Sampling time", "Time target" and "Th_time", respectively. The first is used to set the sampling frequency of the DAQ device, the second for the sampling time per segment, the third for the total time for data collection and the final for preliminary rejection of noise, which will be explained in detail later.

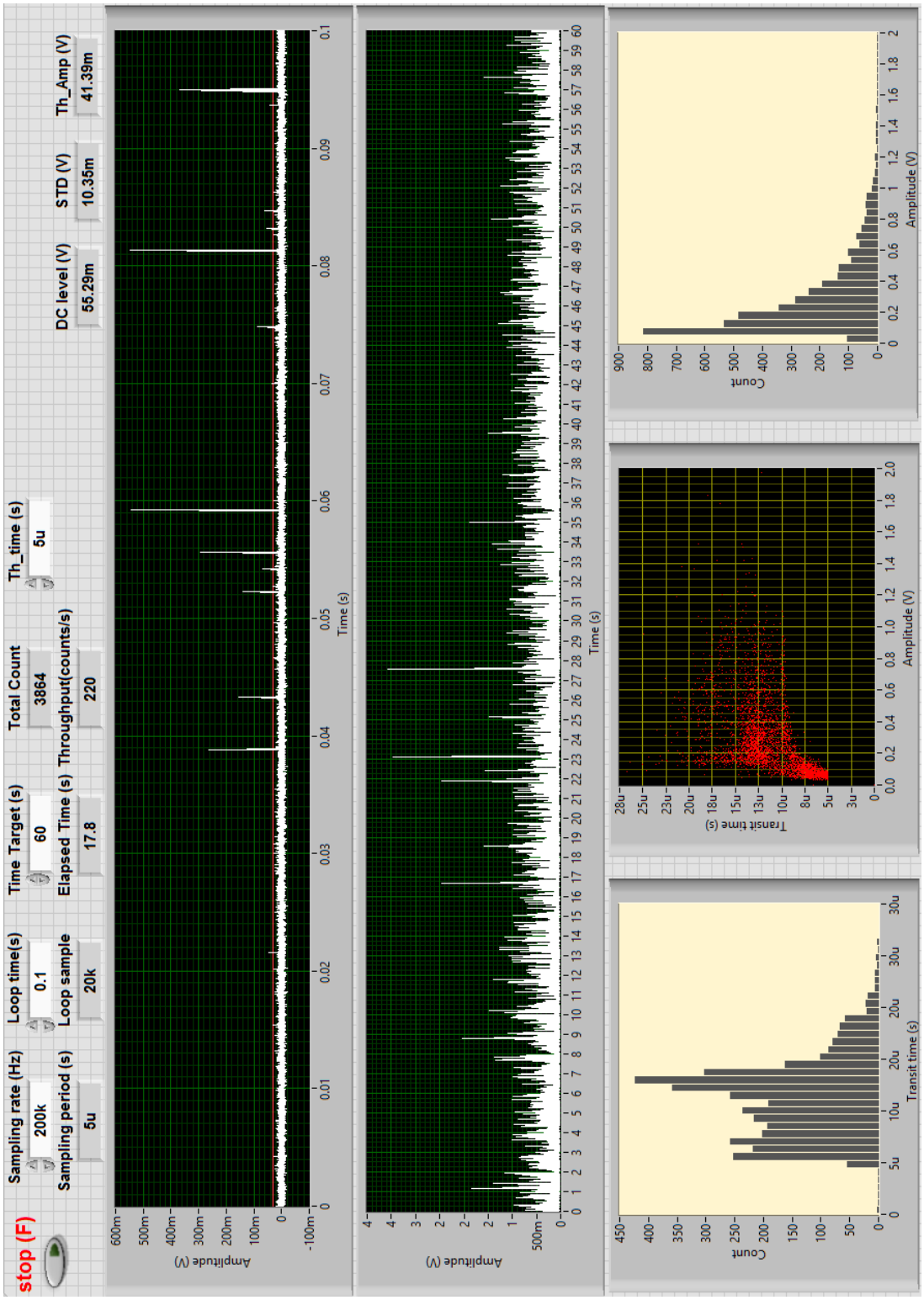


FIGURE 4.7: Front panel of the customized LabVIEW program.

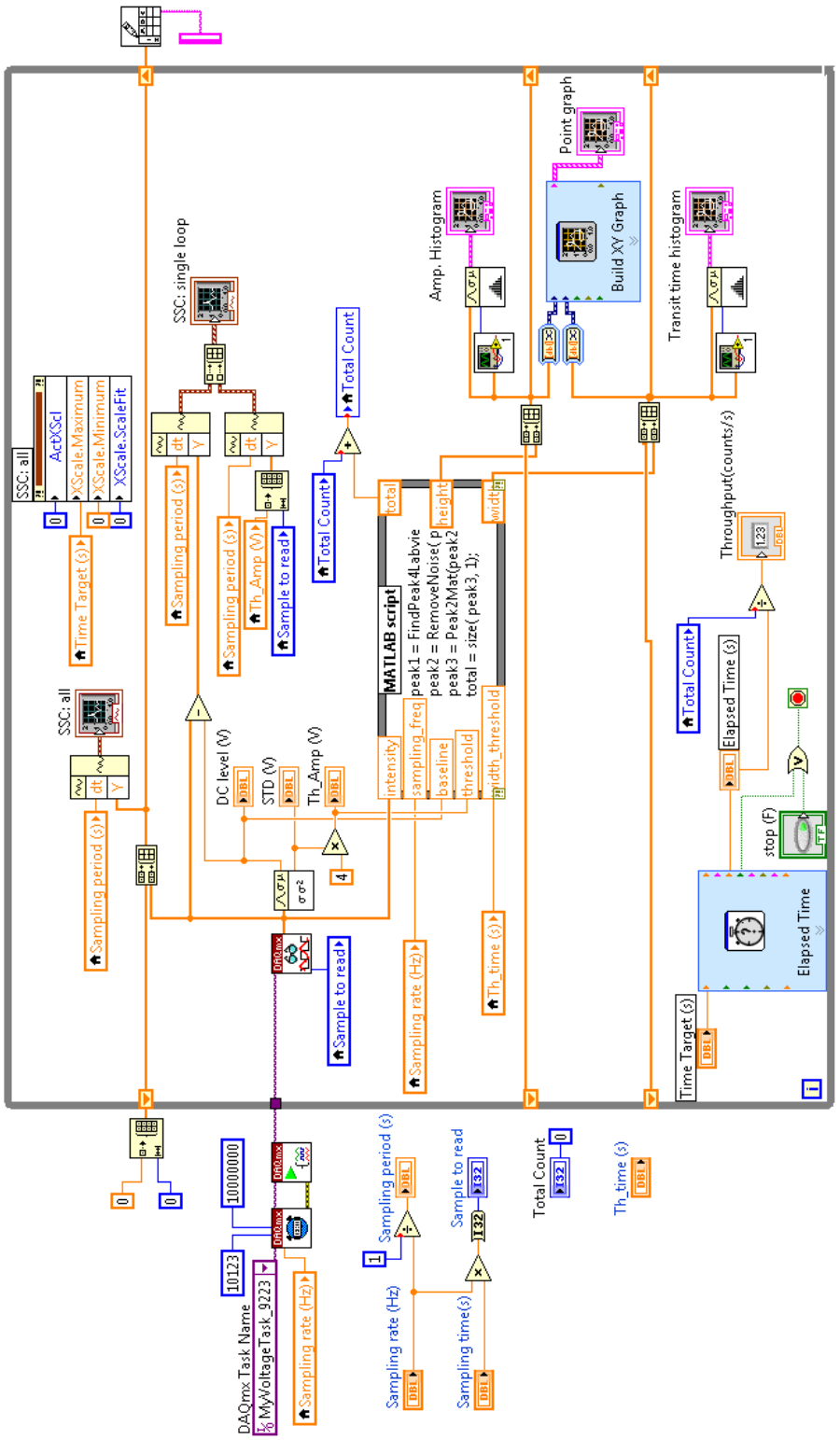


FIGURE 4.8: Block diagram of the customized LabVIEW program.

In the front panel, graph (a1) and (a2) display raw data instantly. The former shows the data collected in each segment and the latter plots all the data. During the operation of the micro-flow cytometer, one pulse will be produced when one particles passes through the interrogation region and this is called one event. The amplitude and transit time of each pulse will be extracted by customized MATLAB codes embedded in the LabVIEW program. Furthermore, the scatter plot of all pulses is shown in (a4) and the histograms of their projections on amplitude and transit time are shown in (a5) and (a3), respectively.

In addition, several numeric indicators are used to instantly display results, which are labeled by "Sampling period", "Sample to read", "Elapsed Time", "Total Count", "Throughput", "DC level", "STD", "Th_Amp". "Sampling period" is the reciprocal of the sampling frequency of DAQ device; "Sample to read" denotes the number of points to be read in each segment; "Elapsed Time" is the time duration from starting the data collection; "Total Count" shows the total count of all events; "Throughput" is the division of "Total Count" by "Elapsed Time"; "DC level". "STD" and "Th_Amp" show the mean value, standard deviation and 4 times of the standard deviation plus the mean value of the data in each segment, which represent the light intensity of the environment, the noise of the system, and the amplitude threshold to differentiate real events from noise, respectively.

### 4.3.2 Data analysis using MATLAB

The PMT anode current is used to indicate the side-scattered (SSC) light intensity, which is the recorded voltage signals divided by the gain of I-V amplifier. One second raw data of SSC light signals is shown in Figure 4.9(a) with a detailed view in (b) and the statistical histogram of all data points in (c). As shown in the figure, the majority of the raw data points are from the background noise. Therefore, a threshold is set to reject these noise data points.

The determination of threshold is of critical importance. A higher one will ignore a portion of pulses, resulting in less total count of effective events. A lower one will add a portion of background noise into the total count of events, resulting in a large false count. Thus, a trade-off between maximum total count of events and minimum false count requires the threshold to be a minimum value with an acceptable false count.

Since the data points of the background noise follow a Gaussian distribution, as shown in Figure 4.9(c), the threshold is chosen to be 4 times of its standard deviation [89], which means a false count of 32 out of 1 million data points.

This false count cannot be ignored if it is comparable with the particle throughput when the data acquisition rate is high. For example, the throughput error due to the false count will be 6 beads/s when the data acquisition rate is 200 kHz, which is comparable with the practical throughput, which will be presented in the next Section.

From the Gaussian fitting of the histogram of all data points, the background light level can be evaluated, which is the mean value of Gaussian distribution, as indicated by the dash-dot line Figure 4.9(b), (c) and (d). In addition, the noise level is evaluated as the standard deviation of the Gaussian distribution and the threshold is 4 times of the noise level, also shown in Figure 4.9(b)-(d) by dashed lines.

A pulse of higher amplitude than the threshold is considered as a possible event, as detailed in Figure 4.9(d), which indicates that one bead has passed through the interrogation region. The amplitude is measured relative to the background and the transit time is the interval between the intercepts of SSC light signals and the threshold.

Further rejection of noise has to be performed because of the non-negligible false count, which can be implemented in a 2-dimensional space of the amplitude and transit time of pulses. After rejection of data points from the background noise, the amplitude and transit time of all pulses in one measurement are extracted and plotted in Figure 4.10(a), in which the dots near the origin are considered from background noise and crosses are from real events that particles pass through the interrogation region. The discrimination of the event signals and noise is performed based on cluster analysis, as shown by the dashed line. Detailed MATLAB codes for these analyses are provide in the Appendix C.

The distributions of the amplitude and transit time of all events are shown by their histograms in Figure 4.10(b) and (c), respectively. Both are fitted using a 2-order Gaussian function. All the event points in (a) can be classified into four groups based on their amplitude and transit time, $g(I_1, \tau_1)$, $g(I_1, \tau_2)$, $g(I_2, \tau_1)$ and $g(I_2, \tau_2)$.

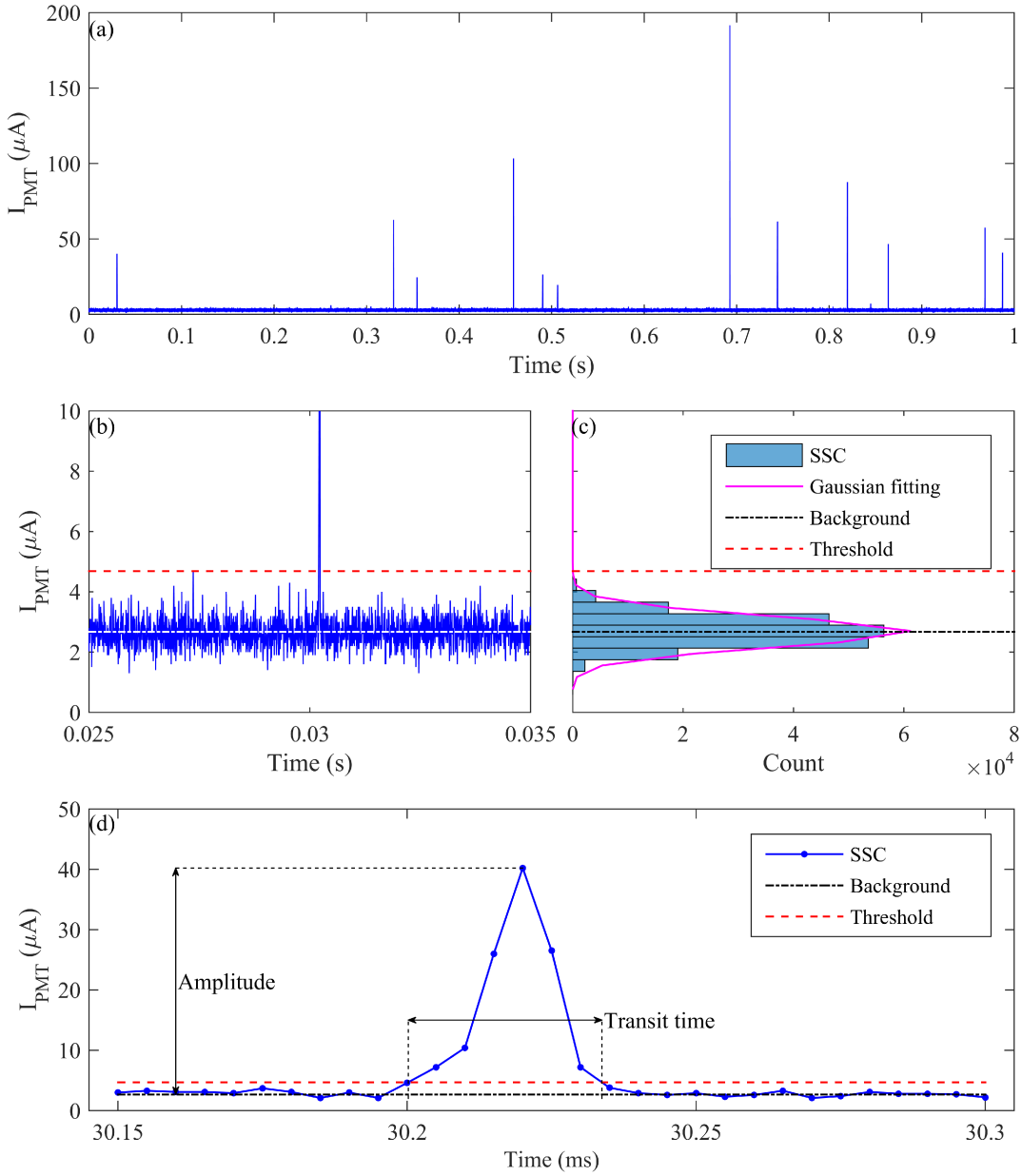


FIGURE 4.9: (a) One second raw data of SSC light signals indicated by the PMT anode current ($I_{PMT}$); (b) a detailed view of the SSC light signals; (c) histogram of all data points (bar) in (a) and the background (dash-dot line) and amplitude threshold (dashed line) based on its Gaussian fitting (solid line); (d) detailed view of one event in which one particle passes through the interrogation region and produces one pulse; the amplitude and threshold are measured relative to the background and the transit time is the interval between the intercepts of SSC light signals and the threshold.

Recalling the particle distribution along z-axis in Figure 4.3(d), most particles travel along the center of microfluidic channel where their velocity is high and thus the transit time of produced events is short, corresponding to $g(I_1, \tau_1)$ and $g(I_2, \tau_1)$, which can be considered as one group because their amplitude distributions overlap with each other. On the other hand, particles near the top and bottom surfaces of the microfluidic channel travel at a relatively lower velocity, which corresponds to the points in $g(I_1, \tau_2)$ and $g(I_2, \tau_2)$. Furthermore, the SSC light intensities produced by particles in these two groups are quite different because the acceptance angle of the particle group near the bottom is larger than that near the top. Therefore, $g(I_2, \tau_2)$ corresponds to the particles near the bottom and $g(I_1, \tau_2)$ near the top.

## 4.4 Performance of the micro-flow cytometer

The total number of the events in unit time interval is defined as the throughput of the micro-flow cytometer ($Throughput$). Theoretically, this is the product of sample flow rate ($FR_{sample}$) and beads concentration ($C_{beads}$) in the sample fluid plus the system error ($\varepsilon$), as shown in equation (1). The performance of the micro-flow cytometer can be evaluated by the linearity of the $Throughput$ over $FR_{sample}$ or $C_{beads}$ and the magnitude of system error, and is represented by

$$Throughput = C_{beads} FR_{sample} + \varepsilon. \tag{4.6}$$

### 4.4.1 Throughput versus sample flow rate at fixed sample to sheath flow rate ratio

A series of measurements on counting micro-sized beads are performed with $FR_{sample}$ from 25 to 300$\mu$L/hour when keeping the ratio of sample-to-sheath flow rate fixed at 1/6.26, which means a stream of particles with a width of about 7$\mu$m and velocities of 0.05-0.6m/s (as simulated in Figure 4.5). The concentration of beads used in these measurements is $5\times10^5$ beads/mL, which is selected to ensure relatively high throughput of particles to reduce the collection time. Lower concentrations of samples will be tested in next sections. Figure 4.11(a) shows the dependence of measured throughput versus $FR_{sample}$ and its linear fitting, from which the concentration of beads can be calculated to be $5.076\times10^5$ beads/mL based on the slope of the linear

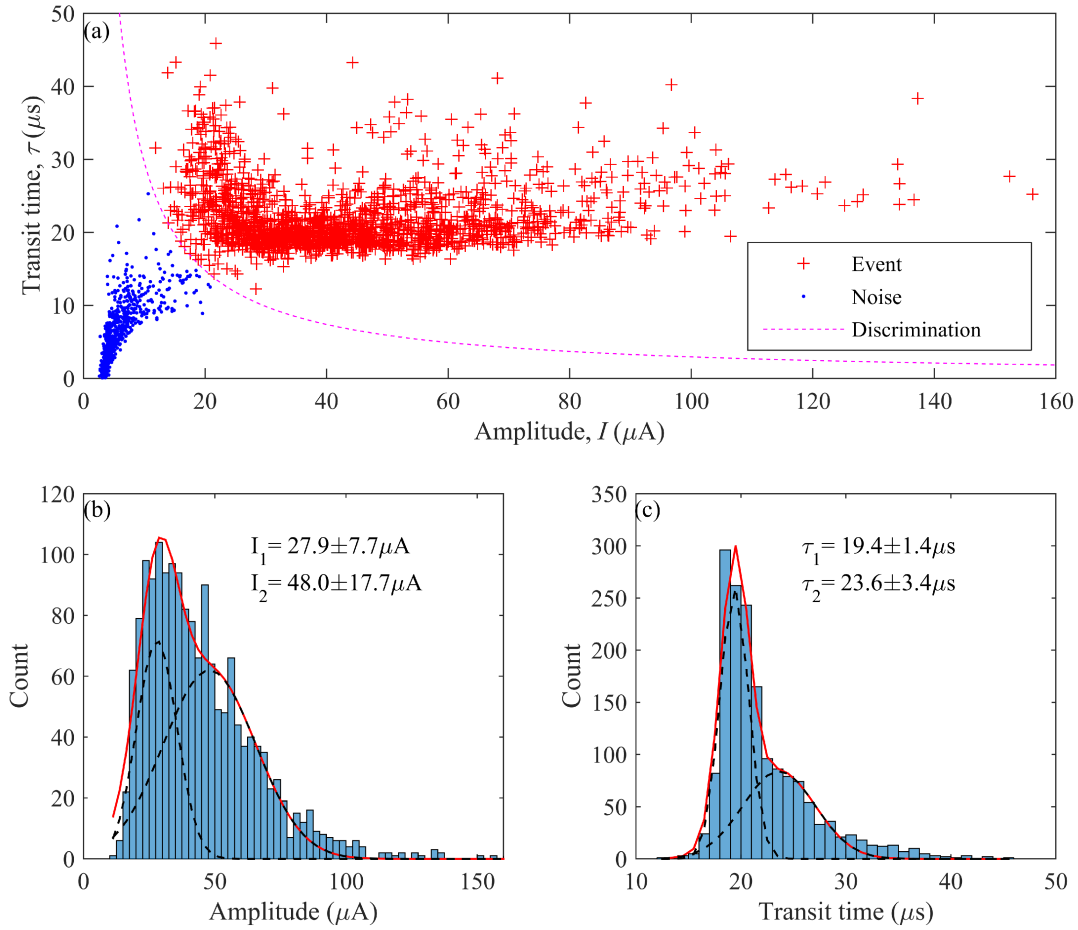


FIGURE 4.10: (a) Scatter plotting of all pulses in a 60 second collection of SSC signals, including events (cross), noise (dot) and their discrimination curve (dashed line); (b) histogram of the amplitude of all events with its 2-order Gaussian fitting; (c) histogram of the transit time of all events with its 2-order Gaussian fitting.

fitting. Therefore, the relative error between the measured value and its expectation is only 1.52%. In addition, the system error of 0.094 for counting is low compared to the throughputs, so that it can be neglected.

All events in each measurement are recorded and their transit times are extracted using the method illustrated in Figure 4.9(b). The relationship between the average transit time of all events in each measurement and the $FR_{total}$ is shown in Figure 4.11(b). Defining the interrogation length (the dimension of the interrogation region along x axis in Figure 4.1(a)) as $L$, the transit time of each bead, $\tau$, will be

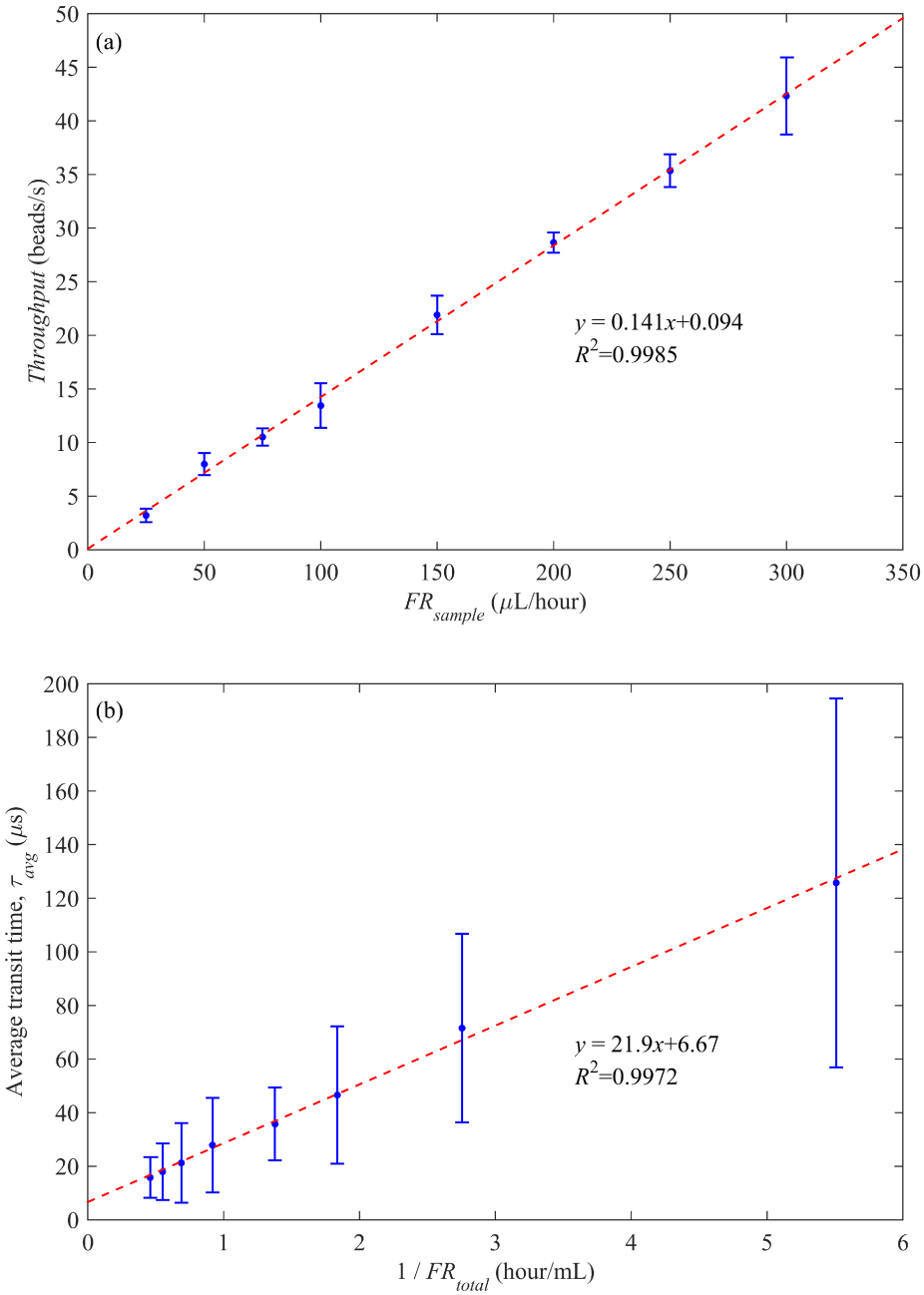


FIGURE 4.11: (a) Measured throughput of beads (dots) versus sample flow rate ($FR_{sample}$) at a fixed ratio of sample to sheath flow rate, 1/6.26, and its linear fitting (dashed line); (b) relationship between the average transit time of beads and the total flow rate ($FR_{total}$) (dots) and its linear fitting (dashed line).

$L/v$, where $v$ is dependent on the $z$ coordinate of the bead, and thus, so is $\tau$. Here, the dependence of $v$ on the $y$-coordinate is ignored because all the beads are confined in the middle of the microfluidic channel (along y axis), as shown in Figure 4.3(e). Considering all events in one measurement, the average transit time, $\tau_{avg}$, can be calculated from equation (4.7).

$$\tau_{avg} = \int_{-h}^{h} \frac{L}{v(z)} p(z)dz = \int_{-h}^{h} \frac{L}{v_{max}[1-(z/h)^2]} p(z)dz \tag{4.7}$$

where $2h$ denotes the height of the microfluidic channel (along z axis), $v_{max}$ is the maximum velocity of the beads in the center of the microfluidic channel and $p(z)$ is the normalized probability of the bead location along z axis, which is proportional to the distribution shown in Figure 4.3(d), and thus can be formulated to $p_0[1-(z/h)^2]$ because the term, $0.006z$, can be neglected. Using the normalization condition, $\int_{-h}^{h} p(z)dz = \int_{-h}^{h} p_0[1-(z/h)^2]dz = 1$, $p_0$ is calculated to be $3/4h$.

Therefore, the equation 4.7 can be simplified to equation 4.8, which shows the linear relationship between $L$ and $1/FR_{total}$.

$$\tau_{avg} = \frac{L}{2v_{max}/3} = \frac{LA}{FR_{total}} \tag{4.8}$$

where $A$ denotes the cross-sectional area of the microfluidic channel, $50mum \times 30\mu m$. Using the slope of the linear fitting in Figure 4.11(b), the interrogation length, $L$, is calculated to be 4.1$\mu$m, which is very close to the beam width of the incident light plus 2 times of the bead radius, 3.5$\mu$m. The difference of 0.6$\mu$m arises because the beam width of the incident light is defined as the full-width at half-maximum (FWHM) of the light intensity along x-axis, whereas the light outside FWHM can also produce scattered light. In addition, the y-intercept of 6.67$\mu$s in Figure 4.11(b) is close to one sample period of the DAQ device, $5\mu m$, when a sampling rate of 200 kHz is used. Both the results on counting beads and the transit time analysis demonstrate the high-accuracy of the micro-flow cytometer.

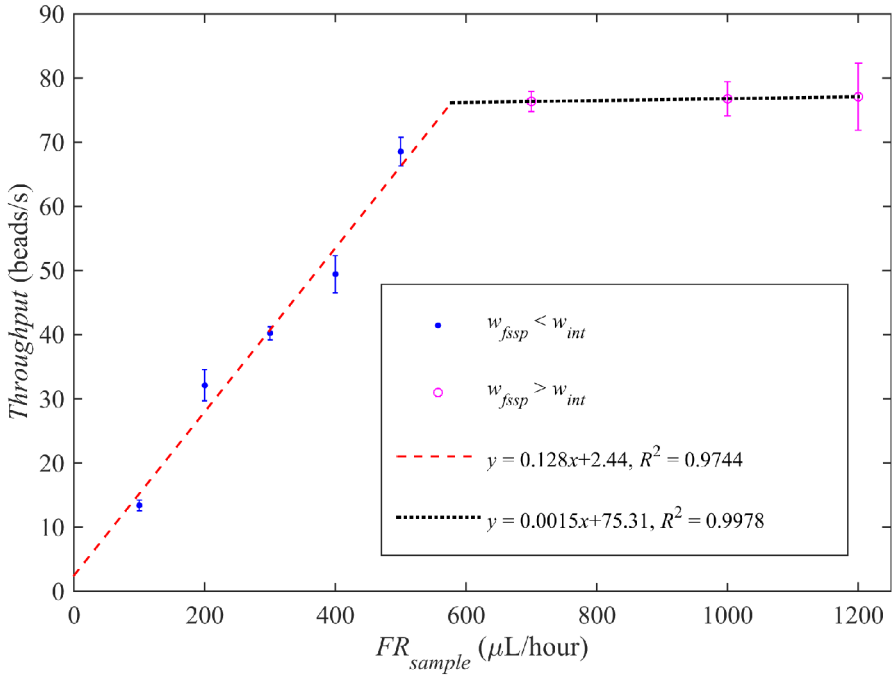


FIGURE 4.12: Measured throughput of beads versus sample flow rate ($FR_{sample}$) when keeping the total flow rate constant at 1452$\mu$L/hour (dots and circles) and their linear fittings as shown (dashed and dotted lines).

### 4.4.2 Throughput versus sample flow rate at fixed total flow rate

The counting performance of the micro-flow cytometer is further tested by varying $FR_{sample}$ from 100 to 1200 $\mu$L/hour but keeping $FR_{total}$ fixed at 1452 $\mu$L/hour, as show in Figure 4.12, which exhibits segmented relationships between the measured throughput of beads and the $FR_{sample}$. The *Throughput* of beads is linear to $FR_{sample}$ when $FR_{sample} \leq 500\mu L/hour$ (dots), but is almost constant when $FR_{sample} \geq 700\mu L/hour$ (circles). By extrapolating the two segments, a turnoff point is estimated at $FR_{sample} = 580\mu L/hour$, which means a $w_{fssp}$ of 15.2$\mu$m based on equation (4.5). In the setup of the micro-flow cytometer, an objective lens and a 0.8mm-diameter pinhole are used to collect the scattered light with a lateral magnification factor of 50. Thus the equivalent width of the interrogation region (along y-axis), $w_{int}$, is 16$\mu$m, which is very close to the estimated $w_{fssp}$ at the turnoff point. This experimental result also demonstrates the reliability of the simulations on hydrodynamic focusing.

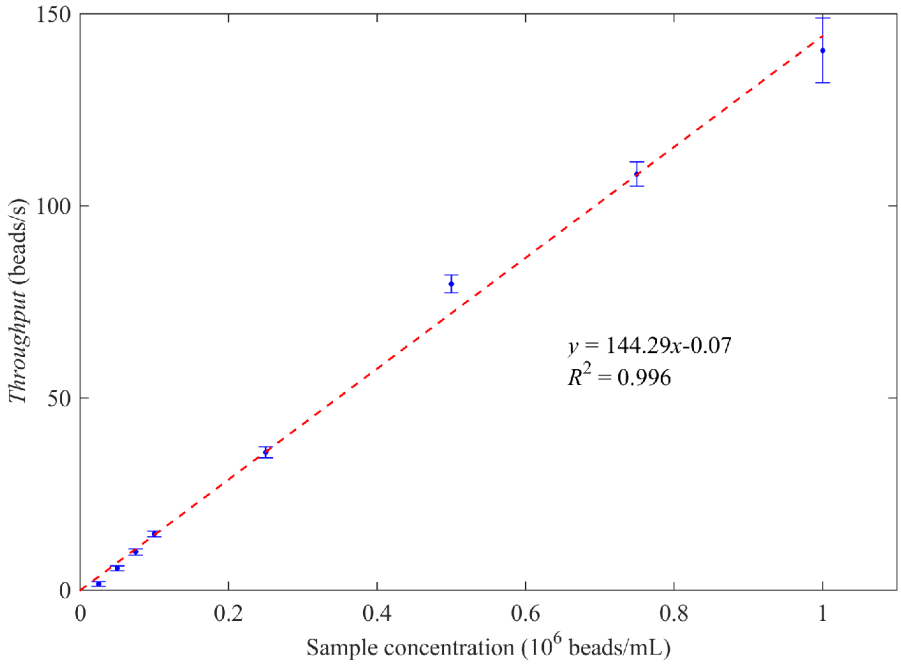


FIGURE 4.13: Measured throughput of beads versus sample concentration when keeping the sample and sheath flow rates constant at 500$\mu$L/hour and 952$\mu$L/hour, respectively.

### 4.4.3 Throughput versus sample concentration

The lower detection limit of micro-flow cytometer is tested by counting beads while varying the sample concentration from $2.5\times10^4$ to $1.0\times10^6$ beads/mL under fixed $FR_{sample}$ and $FR_{total}$ of 500 and 1452 $\mu$L/hour, respectively, as shown in Figure 4.13 (dots). The uncertainty of the sample concentration is about 8% because the sample of $1.0\times10^6$ beads/mL is calibrated using a haemocytometer, from which others are diluted. Their linear fitting with $R^2$ of 0.996 also proves the theoretical relationship in equation (4.6), from which the theoretical slope of the fitting is calculated to be 138.89. Therefore, the relative error between the measurements and theoretical calculation is 3.89%, demonstrating a high counting accuracy of the micro-flow cytometer. In addition, the y-intercept of -0.07 can be ignored with sample concentration down to $1\times10^4$ beads/mL, proving a low system error for absolute counting.

### 4.4.4 Comparison

In Table 4.2, a comparison of the performance of our work with results of similar micro-flow cytometers published recently is provided. Because these publications focused on different aspects of a micro-flow cytometer, only key parameters of a cytometer and the characteristics on absolute counting are listed in this table. A detection of E. coli was reported using aptamer-conjugated fluorescent nanoparticles bonding to the E. coli cells, from which a linearity of 0.963 between the measured counts of fluorescent pulses and those of a conventional colony counting method was achieved with three different concentrations of $4 \times 10^3$, $4 \times 10^4$, $2 \times 10^5$ cfu/ml[135]. Here, the relatively low linearity results is because the counts are underestimated since only fluorescent pulse peak intensity is used for the counting and a relatively high threshold was selected to discriminate the effective signals from the background noise. Counting of magnetic beads[136] and E. coli[137] with concentrations down to $5 \times 10^4$ beads/mL and $1 \times 10^4$ cells/mL were demonstrated with a longer time for data collection. A similar measurement time was reported on counting samples of concentrations that were one or two orders of magnitude higher[89, 91]. Moreover, additional time is required for data processing after all signals are recorded[89, 91, 137]. In comparison with these published results, our work demonstrates better performance either for the dynamic range of the sample concentration, or with the linearity and amount of time for data collection and analysis.

TABLE 4.2: Summary of reported performances of similar micro-flow cytometers on absolute counting.

| Year | **This work** **2016** | Ref. 135 2015 | Ref. 136 2013 | Ref. 137 2011 | Ref. 91 2011 | | Ref. 89 2011 |
|---|---|---|---|---|---|---|---|
| Particle focusing | **1D** | 1D | 2D | 1D | 1D | | 1D |
| Excitation beam shaping | **1D on-chip** | Free space | Inserting fiber | Free space | Free space | | Inserting fiber |
| Optical detection | **Free space** | Free space | Inserting fiber | Free space | Free space | | Inserting fiber |
| Detector | **PMT** | MPPC | PMT | CCD | PMT | | PMT |
| DAQ rate | **200kHz** | - | 60kHz | 30fps | 2kHz | | Event triggered |
| Data processing | **On-line** | On-line | On-line | Off-line | Off-line | | Off-line |
| Sample | **2$\mu$m-beads** | A-FNP-E.coli | Magnetic beads | E. coli | 1$\mu$m-beads | E. coli | 6$\mu$m-beads |
| $C_{sample}$ (particles/mL) | **2.5 $\times$ $10^4$ - 1 $\times$ $10^6$** | $4 \times 10^3$ - $2 \times 10^5$ | $5 \times 10^4$ | $1 \times 10^4$ - $1 \times 10^6$ | $1 \times 10^7$ | $5 \times 10^6$ | $3 \times 10^5$ |
| Data collection time (min) | **1** | 3 | 5 | 10-45 | 1.67 | | 1.25 |
| Throughput (particles/s) | **3.6-144.3** | 0.3-5.8 | 10.8 | - | 83-416 | 350 | 3.75 |
| Throughput vs $FR_{sample}$ linearity | **0.998** | - | - | - | 0.997 | - | - |
| Throughput vs $C_{sample}$ linearity | **0.996** | 0.963 | - | 0.98 | - | - | - |

PMT: photomultiplier tube
MPPC: multi-pixel photon counter
CCD: charge-coupled device
A-FNP: aptamer-conjugated fluorescent nanoparticle

# Chapter 5

# Counting E. Coli using the Micro-Flow Cytometer

A micro-flow cytometer based on the photonic-microfluidic integrated device was designed to count bacteria suspended in water samples. Its performance was described in Chapter 4, exhibiting a high accuracy for counting micro-sized beads. In this chapter, the MFC is used to count E. coli and a 92% detection efficiency is achieved. Our results demonstrate the feasibility of using the MFC for practical bacterial detection[138].

## 5.1 Sample preparation

E. coli DH5$\alpha$ strain is inoculated into a tryptic soy broth and cultured overnight in a 37 ℃ incubator. E. coli cells are pelleted by centrifuging and then re-suspended in phosphate buffered saline (PBS) solution. The concentration of E. coli suspension is estimated by its optical density at 600 nm ($OD_{600}$), which is previously calibrated by comparison of measured $OD_{600}$ of an E. coli suspension and the concentration calculated from manual counting using a haemocytometer (Hausser Scientific, Horsham, PA, USA) under a microscope (Eclipse E200, Nikon, Mississauga, ON, Canada). The calibration shows that an $OD_{600}$ of 1 corresponds to a concentration of $8.3\times10^8$ cells/mL with a relative standard deviation of 8%.

Since water samples taken from environmental sources such as surface water or drinking water usually contains some inorganic particles, then 2$\mu$m- and 4$\mu$m-diameter ($2.00\pm0.04\mu$m and $4.20\pm0.21\mu$m, respectively) uniform blank polystyrene beads (Invitrogen, Burlington, ON, Canada) were added into the E. coli suspension to test their influence on the detection of E. coli. The concentrations of E. coli, 2$\mu$m- and 4$\mu$m-diameter beads in the mixture are $4.5\times10^6$ cells/mL, $2.5\times10^6$ beads/mL and $2.5\times10^6$ beads/mL, respectively.

The concentration of E. coli used in the experiments in this work is $10^6$ cells/mL, which is much higher than the concentration of E. coli in drinking water or surface

water, usually 0–100 cells/mL. Therefore, a pre-concentration of the water sample should be performed to increase the concentration of E. coli by 3-6 orders of magnitude. The pre-concentration stage is not included in this work.

## 5.2 System setup

The system setup of the MFC for counting E. coli is similar to that described in the Section 3.4 of Chapter 3, but utilizes an objective with a zoom image amplifier tube for the SSC light collection. Figure 5.1 shows a schematic setup of the MFC in (a) and a photo of the device with input fiber and SSC light collection objective in (b).

Light from a 532nm laser (Beijing Stone Laser Ltd., Beijing, China) is coupled into the input waveguide through an optical fiber, then focused to the interrogation region by the on-chip lens system. Beads or bacteria suspension in a syringe are injected into the sample inlet by a syringe pump and hydrodynamically focused into the center of the microfluidic channel by the sheath flows at both sides. SSC light produced when the samples pass through the interrogation region is collected by the objective and filtered by an optical filter with a passband of 522-542 nm. A spatial filter with a 0.8mm diameter pinhole is used to reject the ambient light. A photomultiplier tube (PMT) (Newport, Irvine, CA, USA) is used to detect, convert and amplify the light signals into current signals, which will be further amplified by a current-to-voltage amplifier to give voltage signals. The voltage signals are then digitized by a data acquisition card (USB-6211, National Instruments, Austin, TX, USA) and recorded by a custom LabView program for data analysis.

The 50$\mu$m-wide microfluidic channel is focused and imaged onto the plane of the pinhole through the objective with a lateral magnification of 50 and central alignment between the interrogation region and the pinhole. The pinhole and optical filter are mounted inside the PMT to ensure minimum distance between the pinhole and the photocathode of PMT and complete collection of the scattered light passing through the pinhole. The optical path length between the PMT and the microfluidic channel is about 50 cm.

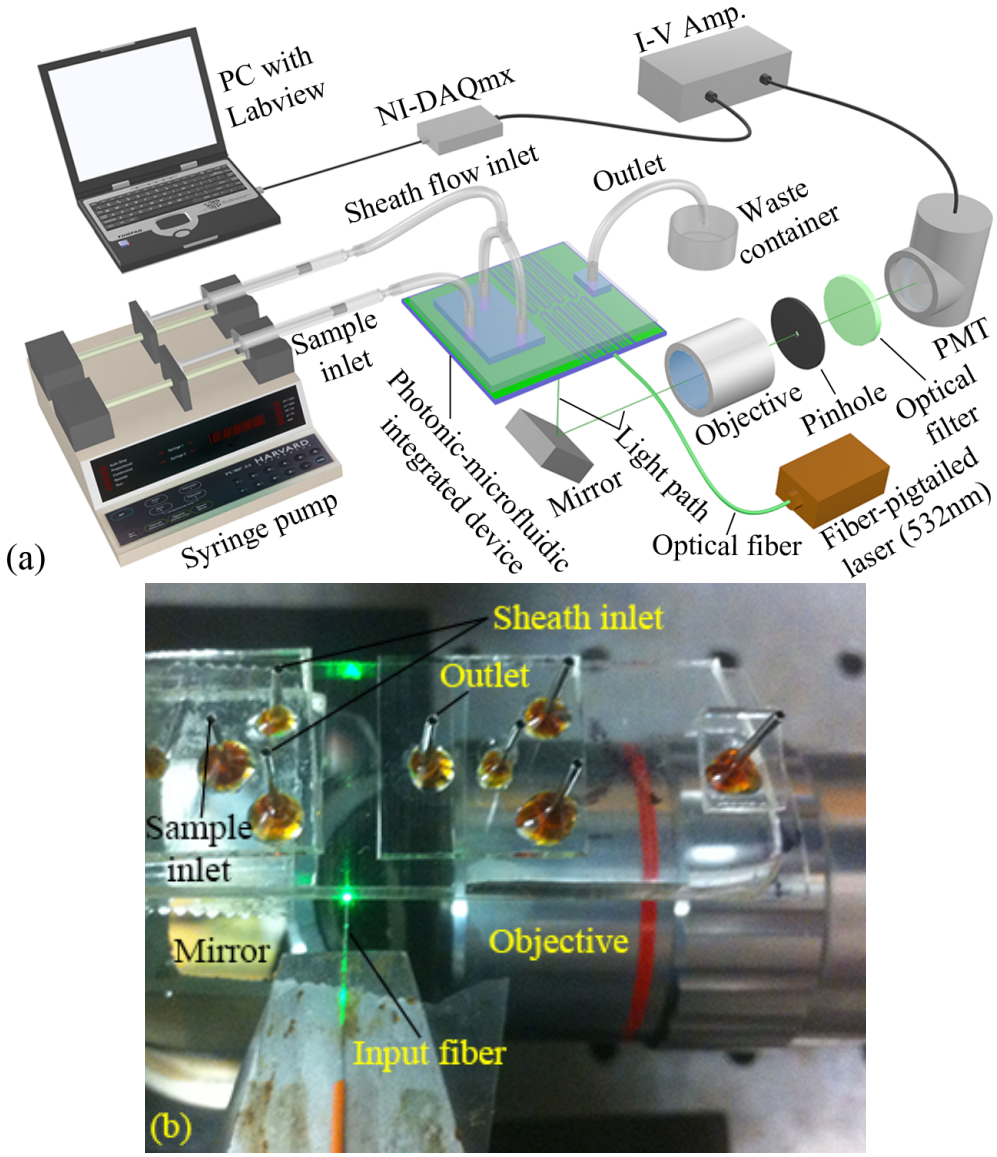


FIGURE 5.1: (a) System setup of a micro-flow cytometer based on the photonic-microfluidic integrated device; (b) a photo of the device with input fiber and light collection components in the system setup.

## 5.3 Counting performance

### 5.3.1 Testing on beads

The performance of this micro-flow cytometer is first calibrated by testing with highly uniform polystyrene beads of diameter of 1$\mu$m although it is characterized by counting 2$\mu$m-beads in Chapter 4 because the E. coli cells are rod-shaped with a length of about 2 $\mu$m and a diameter of 0.5 – 1 $\mu$m.

Figure 5.2(a) shows one-second raw data of SSC signals for a 50-second collection, in which all the bursts generated are clear and obvious. The amplitude and transit time of all bursts are extracted and then plotted in Figure 5.2(b), based on which a discrimination curve is determined to separate the effective events and false ones that originate from background noise. The spreading of all the effective events are evaluated by their statistical histograms on both the pulse height and the transit time, as presented in Figures 5.2 (c) and (d), respectively.

From the perspective of pulse height distribution, all the events can be classified into two sets, which correspond to $I_1 = 0.76 \pm 0.15\mu A$ and $I_2 = 1.01 \pm 0.29\mu A$. The coefficient of variations (CVs, ratio of standard deviation to mean) of $I_1$ and $I_2$ are 19.7% and 28.7%, respectively. $I_2$ is spread more widely than $I_1$ and thus relates to the overall particle distribution from the bottom to the top in the microfluidic channel, whereas $I_1$ is generated by the majority of particles located near the center. Both CVs are relatively high compared to conventional flow cytometer because only 2D hydrodynamic sample centering is used. Since there is no vertical confinement of the beads in the microfluidic channel, then they may vary in the vertical direction, giving rise to a larger variation of SSC signal and hence a larger CV.

From the perspective of transit time distribution, all the events can also be divided into two groups, corresponding to $\tau_1 = 131.5 \pm 9.9\mu s$ and $\tau_2 = 150.9 \pm 34.1\mu s$ with CVs of 7.5% and 22.6%, respectively. $\tau_1$ relates to the particles distributed in the center of the channel and $\tau_2$ originates to the particles spread vertically.

### 5.3.2 Counting E. coli

This micro-flow cytometer is used to count E. coli cells based on the SSC light signals produced when the cells are interrogated by the green laser beam. Figure 5.3(a)

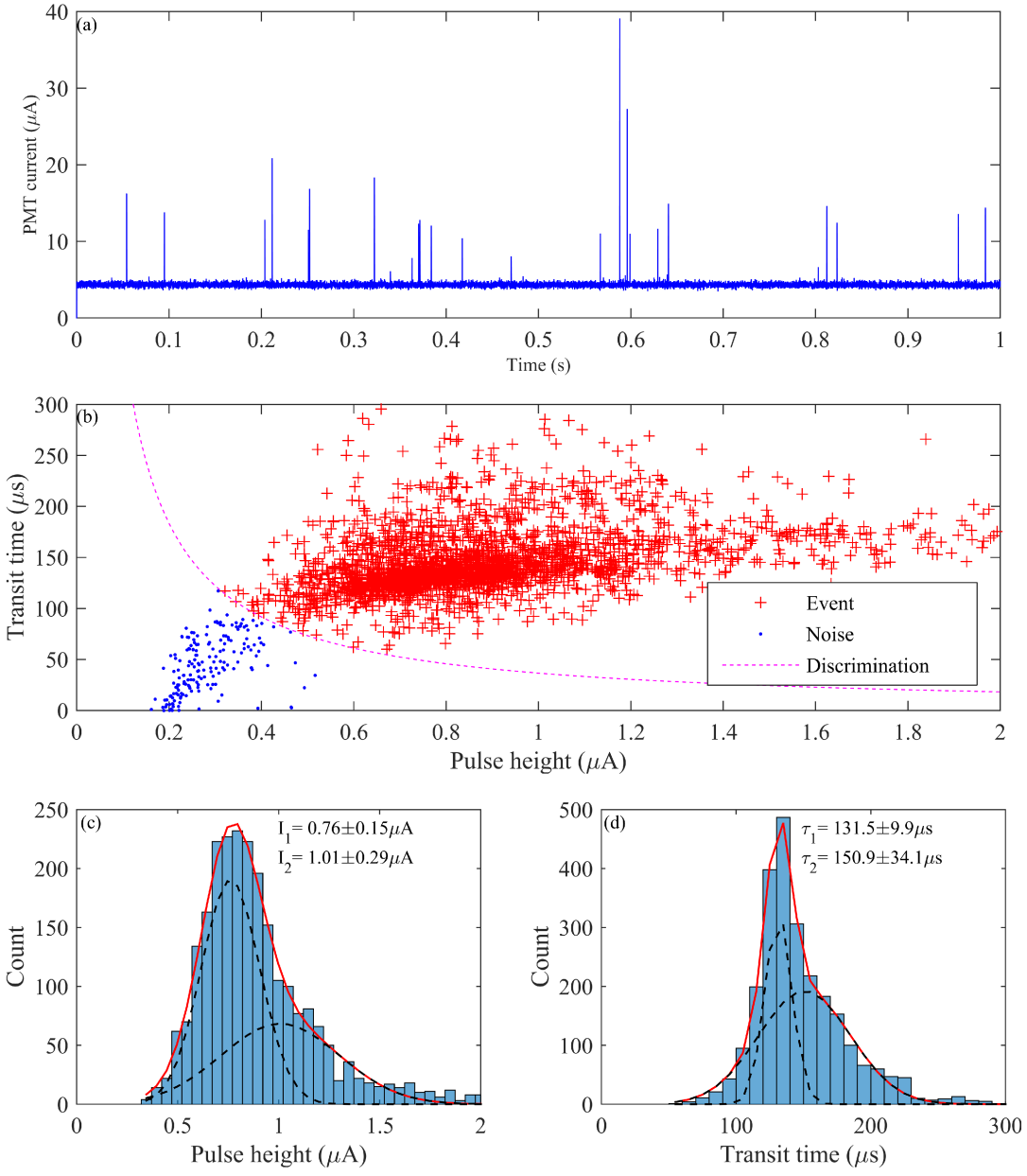


FIGURE 5.2: (a) One-second raw data of SSC signals from 1$\mu$m-diameter blank polystyrene beads for a 50-second collection; (b) scatter plotting of all events in the collection of SSC signals, including event signals (cross) and noises (dot), and their discrimination curve (dashed line); (c) statistical histogram (bars) of pulse height of all events and its Gaussian fitting (solid); (d) statistical histogram (bars) of transit time of all events.

presents the raw data of SSC signals from E. coli cells in a 50-second collection and (b) shows the scatter plotting of all events including the effective event signals and a portion of noise as well as their discrimination curve. Compared to the SSC signals from 1$\mu$m-diameter beads, the intensity of that from E. coli cells is much lower because the difference of refractive index ($n$) between E. coli cells ($n = 1.38$) and water ($n = 1.33$) is much less than that between polystyrene ($n = 1.55$) and water. In addition, the signals from the E. coli cells are close to and mixed with the background noise, which make it difficult to discriminate the effective events from the false ones. Therefore, it is necessary to select an appropriate threshold to reject noise to an acceptable extent. As discussed in Chapter 4, a higher threshold will ignore a portion of events, resulting in less total count of events. A lower one will add a portion of background noise into the total count of events, resulting in a large false count. Thus, a trade-off between maximum total count of events and minimum false count requires the threshold to be a minimum value with an acceptable false count. Since the majority of the data points is from background noise and its histogram is a Gaussian distribution, the threshold is chosen to be 4 times of its standard deviation[89], which means a false count of 32 out of 1 million data points in a 50 second collection.

Fifty-second measurements were performed successively for 10 times to count E. coli suspension in PBS with a concentration of $7.3\times10^6$ cells/mL. The sample and sheath flow rates are fixed at 50 and 313$\mu$L/hour, respectively. The expected throughput of E. coli is the product of E. coli concentration and the sample flow rate, and is calculated to be 101.4 cells/s. Experimental throughputs of the E. coli and signal-to-noise ratios (SNRs) for each measurement are shown in Figure 5.4(b). The SNR of one measurement is defined as the ratio of average signal amplitude to the root mean square of the background noise. The decreasing trend with time of the E. coli throughput arises from the decreasing effective E. coli concentration due to its precipitation in the sample syringe during these measurements. However, the average throughput is 92% of the expected value with a relative standard deviation of 9%. Also, SNRs between 11 and 13 reduces the possibility of false counting from the background noise. The histograms of event signals in the $1^{st}$, $5^{th}$ and $10^{th}$ measurements are shown in Figure 5.4(a), in which a wide population distribution can be found because the size

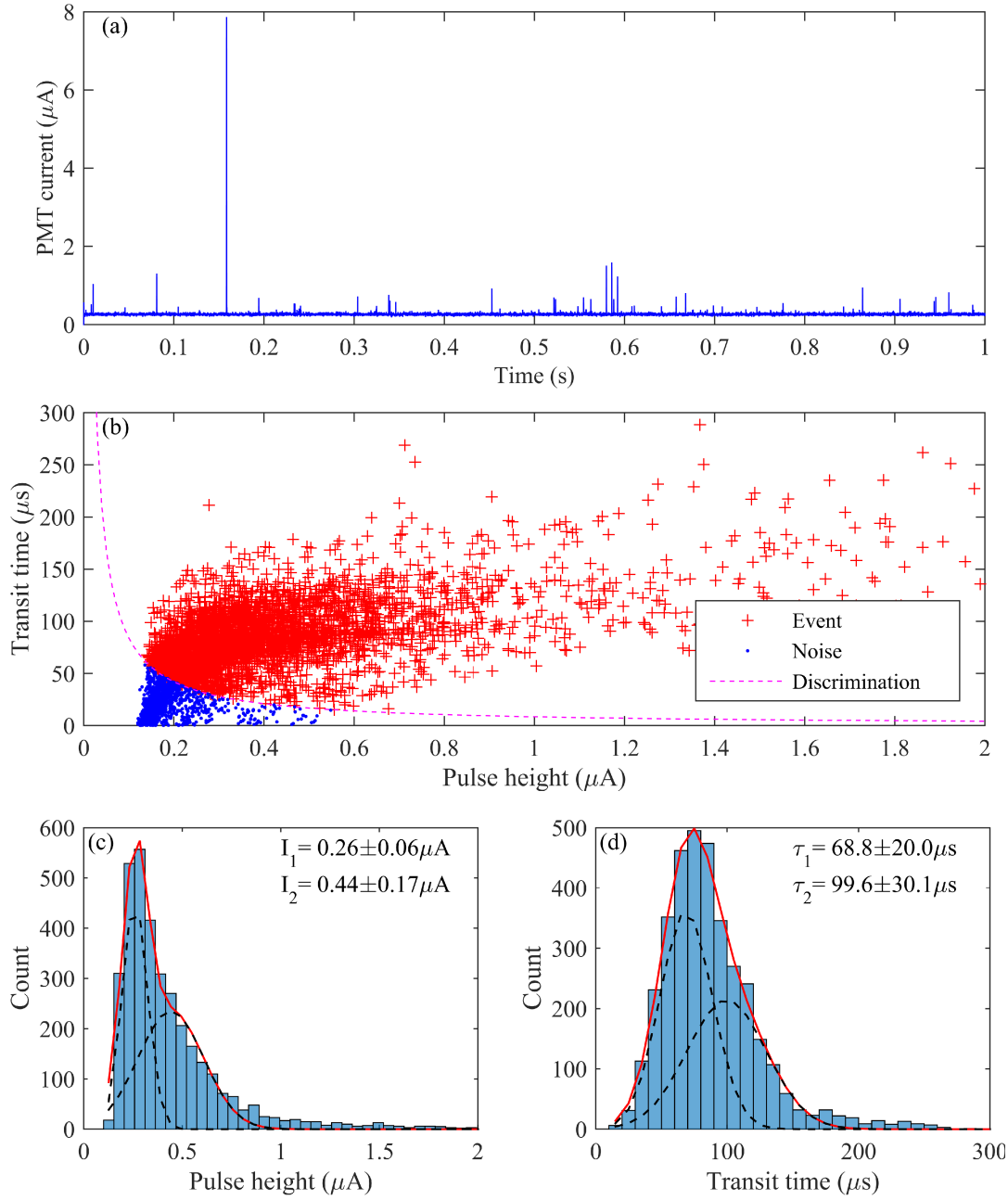


FIGURE 5.3: (a) One-second raw data of SSC signals from E. coli cells for a 50-second collection; (b) scatter plotting of all events in the collection of SSC signals, including event signals (cross) and noises (dot), and their discrimination curve (dashed line); (c) statistical histogram (bars) of pulse height of all events and its Gaussian fitting (solid); (d) statistical histogram (bars) of transit time of all events.

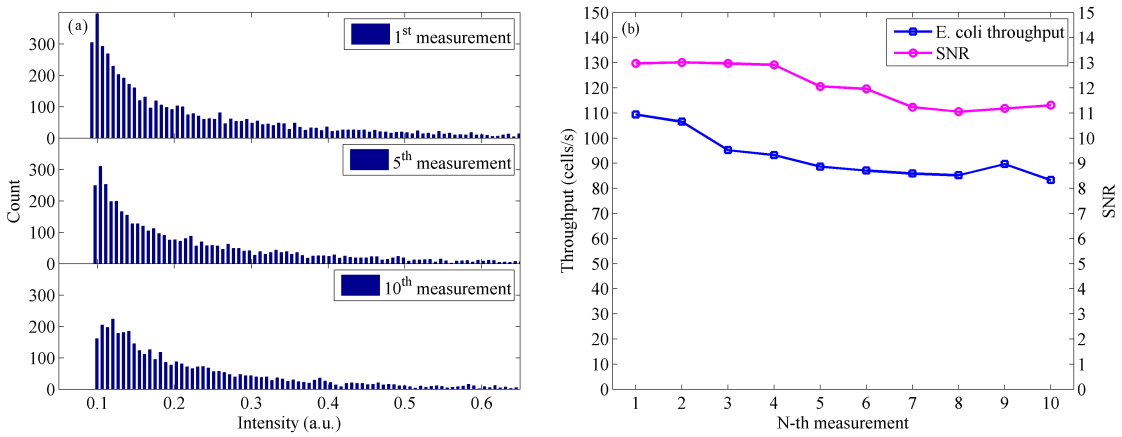


FIGURE 5.4: (a) Statistical histograms of events in the $1^{st}$, $5^{th}$ and $10^{th}$ measurements; (b) Throughputs of E. coli counting (square) and SNRs (circle) for 10 successive measurements with 50-second collection for each. The E. coli concentration is $7.3\times10^6$ cells/mL and the sample and sheath flow rates are 50 and 313 $\mu$L/hour, respectively.

of E. coli cells residing on different growth phases will vary. In addition, rod-shape of E. coli cells results in a higher scattering cross-section than spherical particles when the cells pass through the interrogation area, causing a larger variation of SSC signal intensity.

Varying the sample flow rates from 50 to 150 $\mu$L/hour with a fixed sheath flow rate of 313 $\mu$L/hour were used to study the effect of the sample-to-sheath flow rate ratio on the detection efficiency of counting E. coli, as shown in Table 5.1. The sample stream width is calculated using the following equation,

$$d = \frac{FR_{sample}}{1.5(FR_{sample} + FR_{sheath})}D$$

where $d$ is the focused sample stream width; $FR_{sample}$ and $FR_{sheath}$ are sample and sheath flow rates, respectively; $D$ is width of microfluidic channel (50$\mu$m for the device used). This equation is simplified from equation (11) in Ref. 134 with the assumption that the densities of sample and sheath solutions are equal. This assumption is reasonable because the difference in their relative density is less than $4\times10^{-6}$, which is calculated using parameters of E. coli, pellet density (1.06 g/mL) [139], cell volume (0.6–0.7 $\mu m^3$) [140] and concentration ($4.9\times10^6$ cells/mL) used in the experiment.

TABLE 5.1: Effect of the sample-to-sheath flow rate ratio on sample stream width, E. coli throughputs, detection efficiency and SNR.

| Sample flow rate ($\mu$L/hour) | Sample to sheath flow rate ratio[a] | Sample stream width ($\mu$m)[b] | Measured throughput (cells/s)[c] | Expected throughput (cells/s)[d] | Detection efficiency (%)[e] | SNR |
|---|---|---|---|---|---|---|
| 50 | 0.16 | 4.6 | 65.8±4.9 | 68 | 97±7 | 10.7 |
| 75 | 0.24 | 6.4 | 85.3±2.6 | 102 | 84±3 | 11.0 |
| 100 | 0.32 | 8.1 | 86.2±1.9 | 136 | 63±1 | 10.4 |
| 125 | 0.40 | 9.5 | 91.0±5.9 | 170 | 53±3 | 10.4 |
| 150 | 0.48 | 10.8 | 100.8±7.7 | 204 | 45±8 | 9.7 |

[a] Sheath flow rate is fixed at 313 $\mu$L/hour.
[b] Calculated as described in text.
[c] Obtained from 8 successive measurements with 50 seconds collection for each.
[d] Product of sample flow rate and sample concentration of $4.9\times10^6$ cells/mL.
[e] Ratio of measured throughput to expected throughput.

From Table 5.1, a trade-off exists between the detection efficiency, the ratio of the measured throughput to the expected throughput, and the sample-to-sheath flow rate ratio. When the ratio is 0.16, the sample stream width is 4.6 $\mu$m, E. coli cells are confined to pass through the center of interrogation region and thus are detected with very high accuracy (∼97%). However, when the sample stream width increases, the number of E. coli cells passing through the interrogation region near the edges also increases. SSC light from these cells has a higher possibility to exit the acceptance angle of the objective and is consequently missed for counting, resulting a reduced detection efficiency. This is in agreement with previously reported results in Ref. 84. The SNRs between 9.7 and 11 ensure low possibility of false counting from the background noise.

### 5.3.3 Mixture of E. coli and beads

Interference of particles on counting E. coli is tested by adding 2$\mu$m- and 4$\mu$m-diameter polystyrene beads into the E. coli suspension samples. Ten measurements were performed to check the repeatability of the experiments and Figure 5.5 shows results of a typical experiment. Figure 5.5(a) displays 1 second SSC signal intensity with thresholds of E. coli and beads, 2$\mu$m and 4$\mu$m beads; (b1) shows the histogram of all events in the 50-second collection in logarithmic scale while (b2) and (b3) show

the detailed histograms of E. coli and beads as well as their Gaussian fittings, respectively. The population distribution of E. coli is clearly separated from that of 2$\mu$m and 4$\mu$m beads, indicating that the interference of 2$\mu$m and 4$\mu$m beads can be removed based on the different range of SSC signal intensity. The SSC signal intensity is positively correlated to the particle size and refractive index difference between the particles and water. Note that the refractive index of E. coli is very close to water because an E. coli cell is mostly composed of water. Therefore, interference from particles with sizes of 2$\mu$m and larger can be eliminated based on the SSC signal intensity. However, interference from smaller particles exists, which requires other technique for differentiation, such as labeling E. coli with dye-conjugated antibody and collecting fluorescent and SSC signals simultaneously.

### 5.3.4 Comparison

In Table 5.2, a comparison between reported results and our work is provided. An important advantage of this work is achieving comparable detection efficiency with other works using a micro-flow cytometer of reduced system complexity. This was obtained by integrating the input waveguide and beam shaping lens system on chip [141] and utilizing simple 2D hydrodynamic sample centering that only requires 1 channel of sheath flow. Integration of beam shaping lens system eliminates the bulky lens system and accessories required to position the large lens system for optical path alignment, thus reducing the system cost.

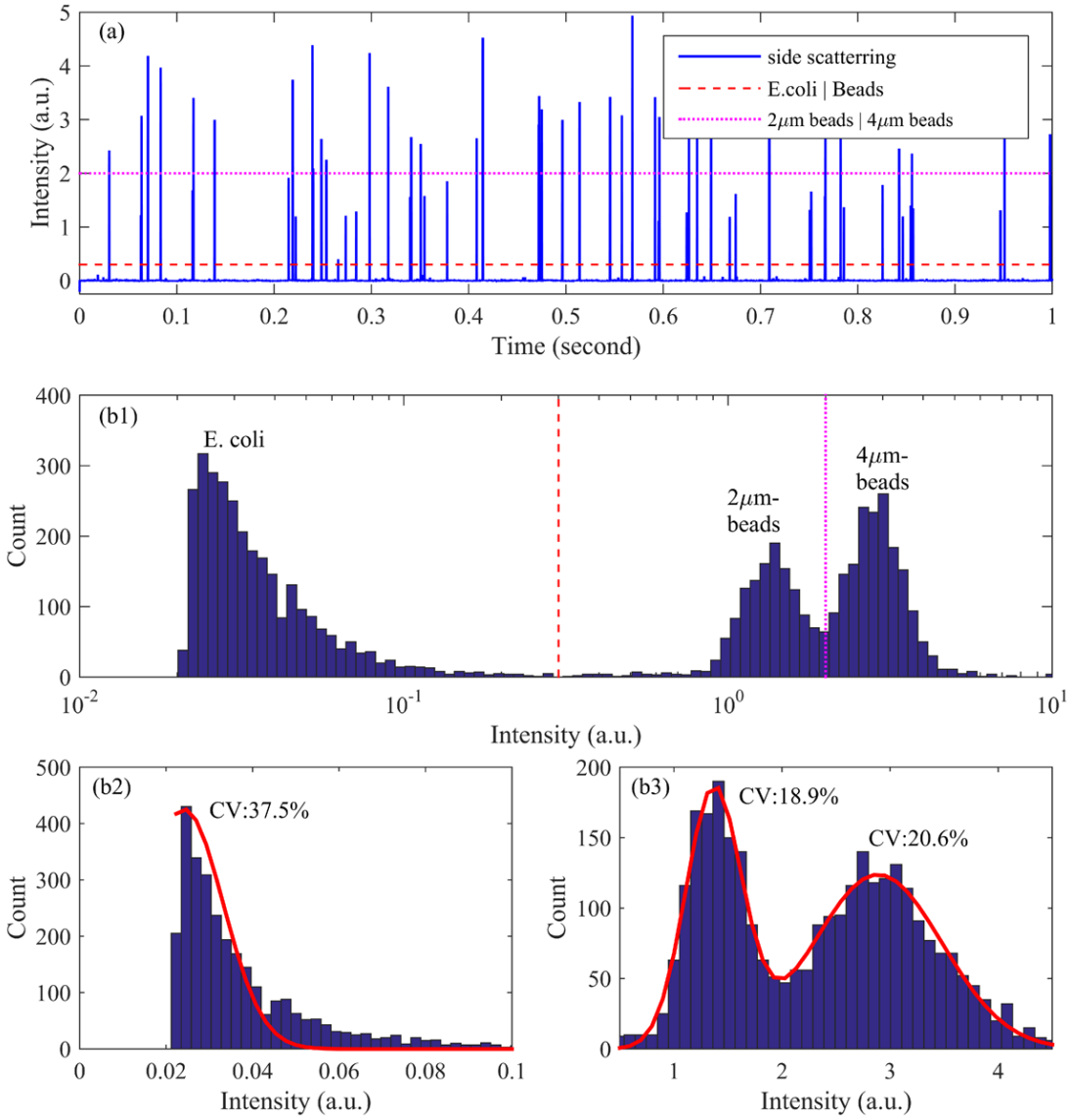


FIGURE 5.5: (a) One second display of SSC signal intensity for a 50-second collection testing on a mixture of E. coli, 2$\mu$m- and 4$\mu$m-diameter beads (solid), intensity separations between E.coli and beads (dashed), between 2$\mu$m- and 4$\mu$m-diameter beads (dotted); (b1) Statistical histograms of events produced by the mixture (bar) with logarithmic scale of intensity, (b2, b3) Statistical histograms of events from E. coli and beads with linear scale of intensity and their Gaussian fittings respectively.

TABLE 5.2: Summary of reported performances of similar micro-flow cytometers and from this work.

| Year | Ref. | Sample | Sample centering technique | Excitation light beam shaping | Throughput (particles/s) | Detection efficiency (%) | | Sample (concentration or velocity) |
|---|---|---|---|---|---|---|---|---|
| | | | | | | Fluo. | SSC | |
| 1999 | 84 | 0.93$\mu$m beads | 2D electrokinetic | 3D free space | 15 | 98 | – | $6.6\times10^7$beads/mL |
| 2001 | 90 | E. coli | 2D electrokinetic | 3D free space | 36 | 94 | – | $2.5-4.5$mm/s |
| 2011 | 91 | 1$\mu$m beads | 2D hydrodynamic | 3D free space | 416.7 | 91.3 | 88.9 | $1\times10^7$beads/mL |
| 2011 | 91 | E. coli | 2D hydrodynamic | 3D free space | 350 | 89.7 | 94.5 | $5\times10^6$beads/mL |
| 2006 | 92 | 1.9$\mu$m beads | 3D hydrodynamic | 3D free space | 17000 | 97 | – | $2.8\times10^8$beads/mL |
| 2015 | **This work** | E. coli | 2D hydrodynamic | 2D on-chip | 101 | – | **92** | $7.3\times10^6$beads/mL |

# Chapter 6

# Conclusion and Recommendation

## 6.1 Conclusion

The presence of coliforms in drinking water is considered as a possible indicator of pathogenic bacteria that can cause waterborne diseases or even fatalities. Generally, E. coli is selected to be an indicator of the microbiological parameter of water quality. Standard methods such as the membrane filter technique involving bacterial culture are time-consuming to detect total coliforms or E. coli. In addition, only a small percentage of the total bacterial population present in environmental water is culturable, which further limits the use of culture-based methods to detect bacteria. Thus, standard methods do not provide real time or accurate information on the presence or absence of bacteria in water. If bacteria are present, timely actions can be taken to prevent the spread of waterborne diseases. Therefore, there is a critical need for simple and rapid detection of bacteria in the water distribution network.

Many techniques have been proposed to rapidly detect bacteria. They include immunological methods, PCR- and FISH-based techniques, FTIR spectroscopic and flow cytometric methods. Many of these methods require sample preparation that cannot be performed on site or require expensive reagents. Therefore, an optical system is proposed to overcome the obstacles towards the in-line monitoring of bacteria in drinking water, which combines the FTIR spectroscopy for bacterial differentiation and micro-flow cytometry for bacteria quantification.

Direct measurement of FTIR spectra of bacterial cells in water is inevitable to ensure the in-line use of the system. The FTIR spectra of common bacteria present in the source water are obtained directly in the water environment by using the spectral window of water where its absorption is low. The differentiation of these cells is performed successfully at species level by the analyses of their spectra. In addition, a preliminary study is conducted on the fabrication of $CaF_2$ concentrator to increase

the bacterial concentration of raw water. A novel phenomenon is found on the stress release process of silicon nitride films on $CaF_2$ crystalline substrate.

Silicon nitride films of a thickness of 50-200 nm are deposited by PECVD on bare (100) and (111) $CaF_2$ crystal substrates. Delaminated wavy buckles formed in the films immediately after removing the deposited $CaF_2$ crystals from the PECVD chamber, are due to the release of internal compressive stress in the films. The stress releasing processes are observed macroscopically and microscopically. Stress releasing patterns start from the substrate edges and then propagate to the centers along defined directions aligned with the crystallographic orientations of the $CaF_2$ substrate. The stress releasing velocity of $SiN_x$ film on (111) $CaF_2$ is larger than that of $SiN_x$ film with the same thickness on (100) $CaF_2$, probably due to the larger interfacial surface stress for $SiN_x$ on (111) $CaF_2$. The velocities of $SiN_x$ film on both (100) and (111) $CaF_2$ increase with the film thickness increasing because thicker films exhibit larger stresses. Finally, the atomic ratio, x, of stress $SiN_x$ and stress-release $SiN_x$ is analyzed by using X-ray photoelectron spectroscopy. The results show the same x, proving that the stress releasing process is a physical change.

Accurate counting of particles at low concentrations is demonstrated using a micro-flow cytometer based on a device integrated microfluidic channels and beam-shaping lens system. The measured throughput of particles is linearly dependent on the concentration and volumetric flow rate of the sample particles when one of them is fixed. The lower limit of the concentration achieved is $2.5 \times 10^4$ beads/ml. The throughput of particles is also linear to the sample flow rate with fixed total flow rate, exhibiting no degradation of the counting efficiency when the focused sample stream expands due to the improved data analysis method that can discriminate effective signal and noise precisely. The throughput is constant when the width of the focused sample stream is larger than the diameter of SSC collection aperture. The turnoff point is explained using the simulated results of the width of the focused sample stream of particles by tracing their movements in the fluid. Finally, the above results of high linearity for counting even at low concentrations prove the high accuracy of this micro-flow cytometer, which makes it very suitable for applications on absolute counting of low concentration samples such as rare cell in blood analysis or pathogen detection for water and food security.

Counting of E. coli in PBS is demonstrated by using a micro-flow cytometer based on a photonic-microfluidic integrated device. The integrated system consists of input waveguides, a beam shaping lens system and microfluidic channels with a 2D hydrodynamic focusing. Only the SSC light signals from samples are collected in free space and used for counting, allowing for detecting bacteria in water without tagging them. A detection efficiency of 92% is achieved at a throughput of 101 cells/s when compared with standard counts using a haemocytometer. The detection efficiency is correlated to the sample-to-sheath flow rate ratio. A high detection efficiency of 97% is achieved at a low ratio of 0.16. Tests on mixtures of E. coli, 2$\mu$m- and 4$\mu$m-diameter polystyrene beads show distinct separation on their scattering intensities, indicating that interference from particles of similar or larger sizes can be easily removed.

## 6.2 Recommendation

This work has made many efforts towards the ultimate goal of in-line monitoring of bacteria in drinking water. But there still exist a few issues to be solved in the near future.

First, a library of the IR spectra of bacteria commonly found in source water should be established for the differentiation and identification of unknown bacterial samples. For each bacterial species, a series of samples with different concentrations should be acquired, which can be used to eliminate the spectral background mainly caused by scattering. Thus, more precise IR spectrum can be acquired for each strain. Moreover, the thickness of the liquid cuvette containing the bacterial suspension can be reduced to 5-10$\mu$m, which can further reduce the absorption of water. In addition, the algorithm of spectral decomposition on the basis of spectra in the library should be developed to calculate the weight coefficients, which indicates the percentage of bacterial cells of each species relative to the total cells.

Second, the concentrations of coliform bacteria and E. coli are ultra-low, about 0 – 100 cells/ml even in contaminated drinking water, which makes it difficult for detection, especially when other non-coliform bacteria exist in much higher concentrations than the coliforms. A bacterial sample in relatively high concentration is needed to ensure sufficient signal-to-noise ratio in the FTIR measurement. Moreover, the lower

limit of detection of the micro-flow cytometer is about $10^4$ cells/ml. Therefore, the raw water samples have to be concentrated first.

A relatively large volume of raw water should be concentrated to meet the requirement of FTIR and MFC measurements. The concentrating ratio is dependent on the original concentration of bacteria in the raw water. For example, a concentrating ratio of 1000 should be achieved for the MFC measurement when the bacterial concentration is 10cells/mL in the raw water. Thus, 1mL concentrate means that 1000mL raw water should be processed. The concentrating process is similar to the filtration, but with emphasis on the retentate or permeate. Screen type filters should be used to keep the bacterial cells in the retentate. Depth type filters are not recommended because bacterial cells are captured inside the filter in the process and are difficult to recover them in the retentate. In addition, the maximum pore size of the filter should be less 0.5$\mu$m to ensure no bacterial cells can pass through the membrane. Moreover, tangential flow configuration is recommended for the concentrating process because it can reduce the influence of bacterial accumulation on the filtration flow rate.

Third, the micro-flow cytometer should be further improved to decrease its lower limit of detection (LOD) on the sample concentration. It can be achieved either by increasing the sample flow rate or by reducing the minimum throughput that the MFC can measure, or both. Regarding the sample flow rate, its maximum relies on the maximal velocity of the fluid in the channel and the cross-sectional area of the microfluidic channel. The former is limited by the maximal velocity at which the bacterial cells can survive because excessively high velocity of fluid can break cells. The latter is restricted by the SU-8 device fabrication. On the other hand, low throughput of particles or cells means the detection of single pulse in a waveform acquired at high sampling rate for long time duration. For example, assuming the particle velocity of 1m/s and the light beam width of 10$\mu$m, when the sample rate is $10^6$ samples per second, a throughput of 1 particle per minute means a pulse of 10 data points in a background of $6\times10^7$ data points. Thus, high-speed electronics with large storage memory will be needed for the data processing.

Fourth, all the components should be assembled to a compact micro-flow cytometer, including the core device, light source and detector, syringe pumps, optical and electronic components. Semiconductor laser diodes are recommended to be used as the

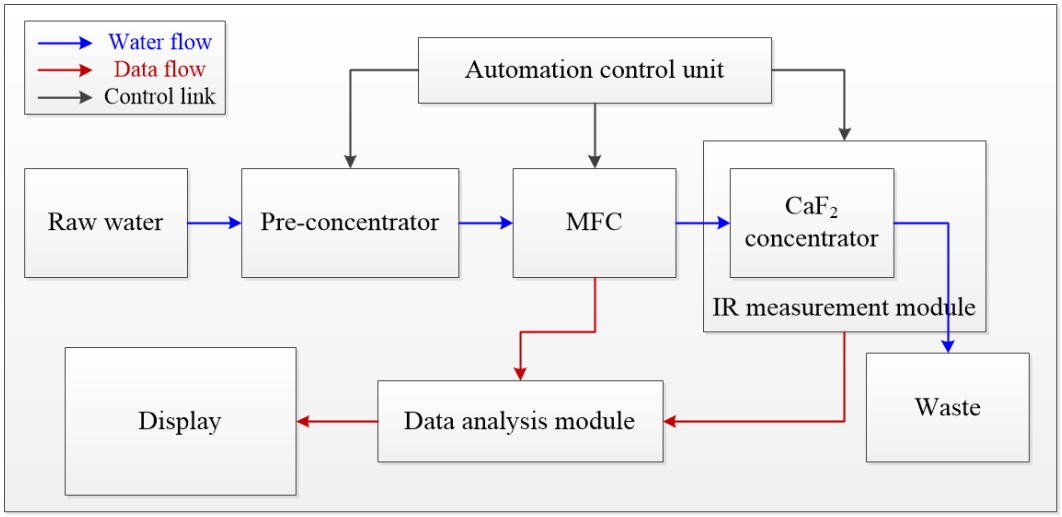


FIGURE 6.1: Schematic digram of the system for in-line monitoring of bacteria in drinking water.

light source because of its small size and low cost. Micro-PMT or avalanche photodiodes are preferred for the light detection. Small size stepper motors can be used to drive the syringe to precisely control the sample and sheath flow rates. Analog-to-digital converter with 12 or 16 bit conversion resolution and sampling rate of 1 million samples per second or higher is recommended for the data acquisition.

Finally, the system for in-line monitoring of bacteria in drinking water should be assembled. A schematic diagram of the system is shown in Figure 6.1. Raw water is pre-concentrated and injected into the micro-flow cytometer to measure the concentration of total bacterial cells. Then, the effluent is further concentrated using the $CaF_2$ concentrator for IR spectral acquisition of the bacteria in the water sample. Measured data are analyzed to calculate the concentration of bacteria in each species present in the library, which is displayed or transmitted to a remote center.

# Appendix A

# Fabrication procedure of SU-8 device

1. **Wafer cleaning**. To ensure good adhesion of the SU-8 photoresist layers onto the glass wafer, any organic substances that perhaps exist on the substrate surface must be removed.

   (a) Submerse a Pyrex glass wafer in a beak of acetone and then put the beak in a ultrasonic cleaner for 10 minutes.

   (b) Replace the acetone with ethanol and perform another ultrasonic cleaning for 10 minutes.

   (c) Rinse the wafer with de-ionized (DI) water and then dry it with pure nitrogen.

   (d) Soak the wafer in a piranha solution for 30 minutes.

   (e) Rinse the wafer with DI water and dry it using pure nitrogen blowing.

2. **Wafer baking**. The cleaned wafers are baked in an oven at 265℃ for 3 hours in order to ensure all water molecules are removed from the wafer surface because their existences can reduce the adhesion of SU-8 photoresist onto the glass wafer.

3. Intermediate layer formation using SU-8 3035 photoresist that features enhanced adhesion to substrates.

   (a) **Coat**. The SU-8 3035 photoresist is diluted in the corresponding developer at a mass ratio of 3:7. The diluted solution is poured onto the wafer and then spun at 3000 round per minute (rpm) for 60 seconds, yielding a film of approximately 600nm thick.

   (b) **Soft bake**. The wafer is placed onto a hotplate at 95℃ for 5 minutes to drive out any solvent in the photoresist.

(c) **UV exposure**. The wafer is placed in the mask aligner and exposed for 20 seconds without mask at an UV light (365nm) intensity of 4.5 $mW/cm^2$.

(d) **Post-exposure bake (PEB)**. The exposed wafer is placed onto a hotplate at 95℃ for 5 minutes to facilitate the cross-linking of molecules in the intermediate layer.

4. Functionality layer formation using SU-8 2035 photoresist capable of producing high aspect ratio structures.

   (a) **Coat**. As a photoresist of high viscosity, a portion of SU-8 2035 is carefully poured onto the center of the wafer in order to avoid bubble formation. The wafer is manually tilted and rotated to ensure that the entire surface is covered before spinning. Then the wafer is spun with a speed profile of ramping up, holding and ramping down.

      i. Ramping up. The spinner accelerates from 0 to 2000rpm in 30 seconds.

      ii. Holding. The wafer is spinning at 2000rpm for 60 seconds.

      iii. Ramping down. The spinner decelerates from 2000rpm to 0 in 30 seconds.

   (b) **Edge bead removal (EBR)**. During the previous spin coat process, a build up of photoresist will occur on the edge of the substrate, resulting much thicker film at the edge than in the center. By removing any edge bead, the photomask can be placed into close contact with the wafer for improved resolution and aspect ratio. In addition, the thick photoresist at the edge may contaminate the hotplate during soft bake process. Therefore, the wafer is spun at 500rpm and a small stream of the corresponding developer is applied at the edge of the wafer top surface to remove the edge bead.

   (c) **Soft bake**. The coated wafer is placed into an programmable oven at room temperature (25℃), which is set to ramp up to 95℃ in 1 hour followed by immediate ramping down to 25℃ in 3 hours. This slow thermal treatment process is to ensure the relaxation of the film stress due to the difference in thermal expansion coefficients of SU-8 photoresist and glass.

(d) **UV exposure**. The coated wafer is exposed to UV light for pattern transfer from the mask. To ensure good resolution and high aspect ratio, the top surface of the coated wafer should be in contact with the mask. The UV exposure is performed in on/off cycles with typically 5-10 seconds on and 5 seconds off intervals. This is to ensure a relaxation of the acid produced in the exposed SU-8 photoresist and avoid results similar to over exposure when the SU-8 photoresist is exposed at the same dose for one time. It is found that the UV light intensity and total number of cycles are flexible without detriment to the device quality as long as the total exposure dose is constant. Because the UV exposure dose is a key parameter to device quality, it is optimized experimentally, which will be detailed in the following subsection.

(e) **PEB**. The exposed wafer is placed into an programmable oven at room temperature (25℃), which is set to ramp up to 90℃ in 1 hour followed by immediate ramping down to 25℃ in 3 hours. This thermal treatment drives the cross-linking of the exposed SU-8 epoxy molecules to form the rigid structures required. Heating and especially cooling must be done slowly to ensure that the bonding between the device layer and the intermediate layer is maintained otherwise the device layer will detach away from the intermediate layer.

(f) **Development**. The wafers are submersed in the developer and agitated for 5 minutes and then rinsed with a stream of isopropyl alcohol (IPA) followed by drying under a nitrogen blow.

(g) **Inspection**. The wafer with formed devices can be inspected under a microscope to determine the quality of formed structures. Any defects near the optical structures will result in difficult sealing with PDMS cover slip.

(h) **Device encapsulation**. The finished wafers are encapsulated with a sacrificial layer to prevent debris during dicing from contact the SU-8 devices. Shipley S1818 photoresist is applied to the entire surface and spun at 500rpm for 30 seconds. The wafer is then placed onto a hotplate at 95℃ for 5 minutes.

5. **Wafer dicing**. To fully utilize the advantage of photolithography on volume production, 6 devices are fabricated in one wafer with single PL process. Then, the wafer is diced into separate devices, allowing for input and output light coupling at the facets of the waveguide structures. A dicing saw is used to cut the finished wafers.

   (a) **Wafer dicing**. A finished wafer is mounted by vacuum suction onto the sample holder of the dicing machine through a tape. Cuts are made as close to the formed waveguide facets as possible without touching them.

   (b) **Encapsulant removal**. The Shipley S1818 photoresist on the top of each device should be removed by acetone spray. Dicing debris is also washed off with the photoresist. Once the S1818 photoresist is removed, rinse the devices in the SU-8 developer and then IPA, followed by rinse in DI water and drying by nitrogen blow.

   (c) **Inspection**. Devices can be inspected again under a microscope to ensure that waveguide facets are clean, intact and that the devices are clean and there are no debris.

# Appendix B

## Photolithographic mask

The mask for PL procedure of SU-8 devices includes 6 devices.

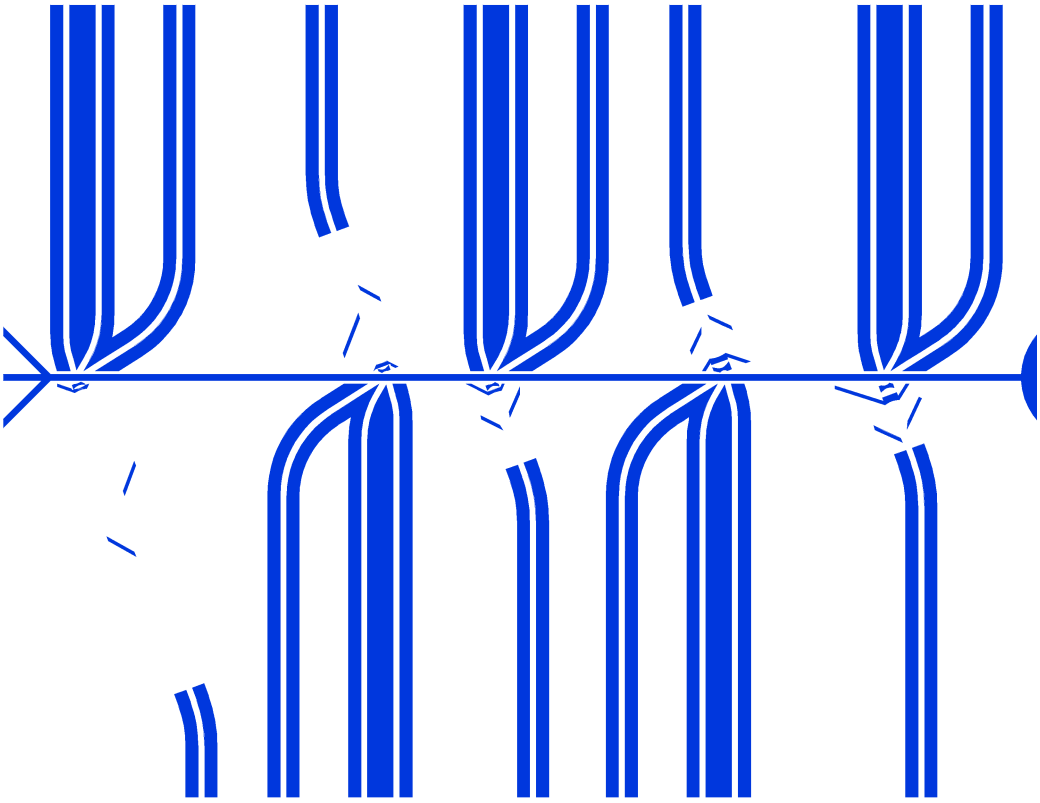

FIGURE B.1: Device 1 of the mask for PL procedure of the SU-8 device, in which the incident angle of each beam is 20° relative to the normal of the microfluidic channel.

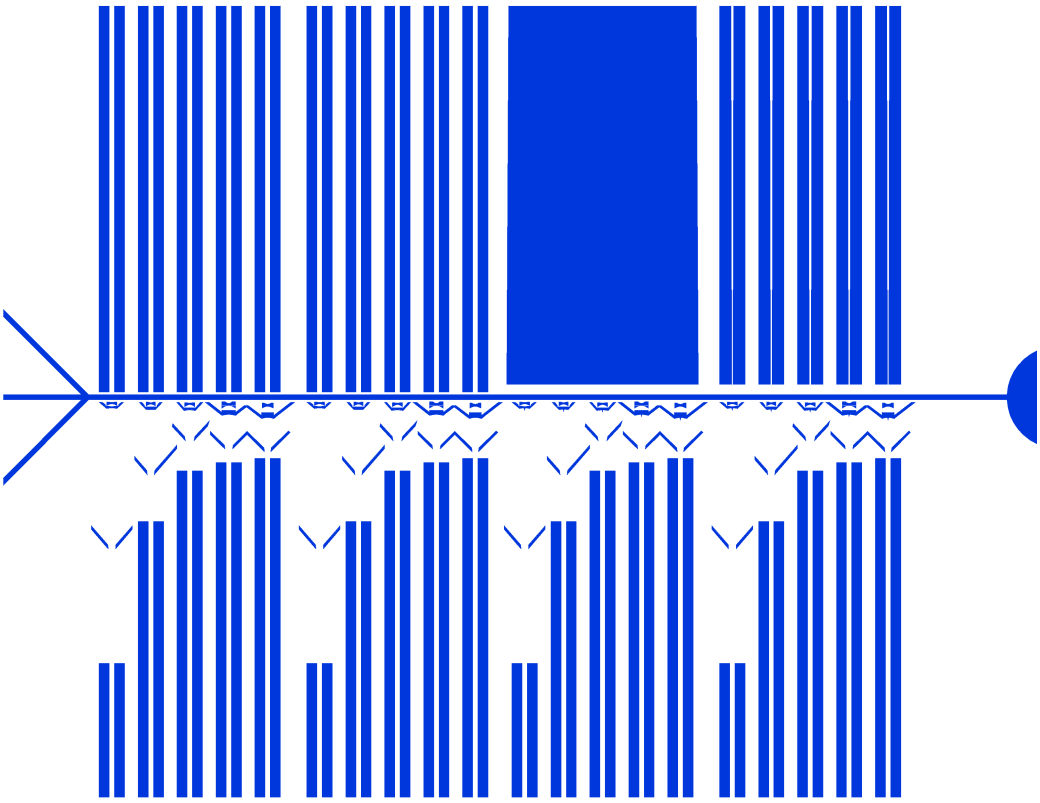

FIGURE B.2: Device 2 of the mask for PL procedure of the SU-8 device, in which all the illumination beams are normally incident to the microfluidic channel.

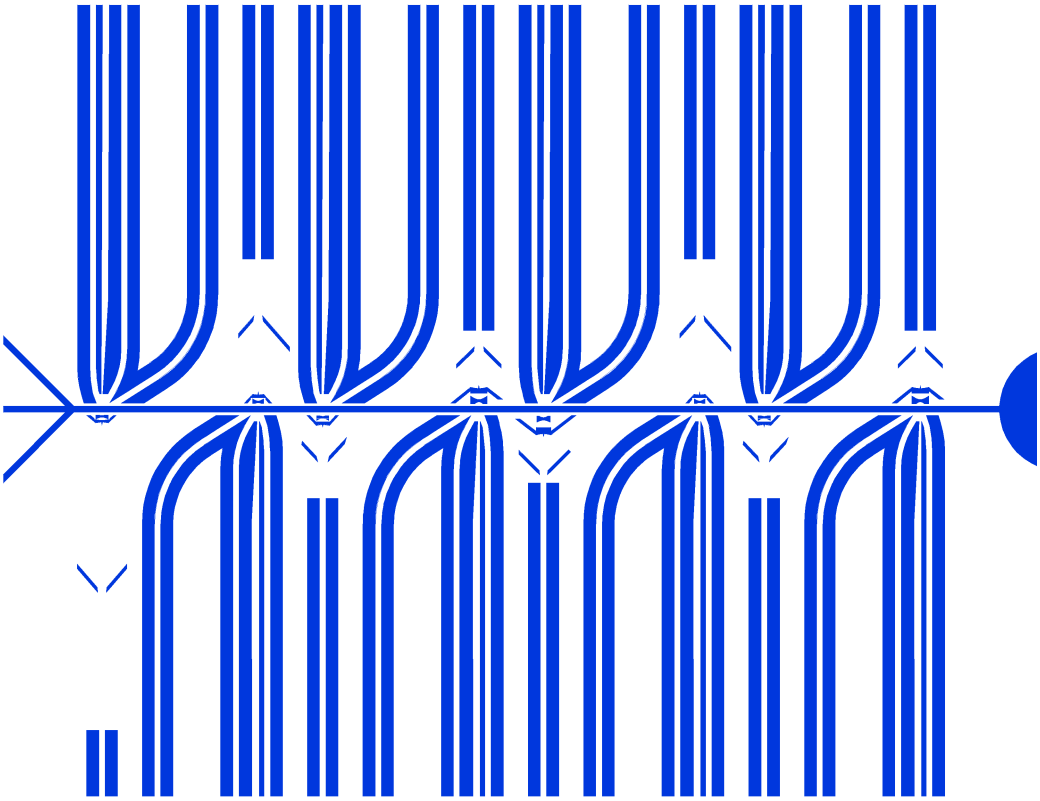

FIGURE B.3: Device 3 of the mask for PL procedure of the SU-8 device, in which all the illumination beams are normally incident to the microfluidic channel and a notch is added onto the first lens for on-chip detection of forward scattered light.

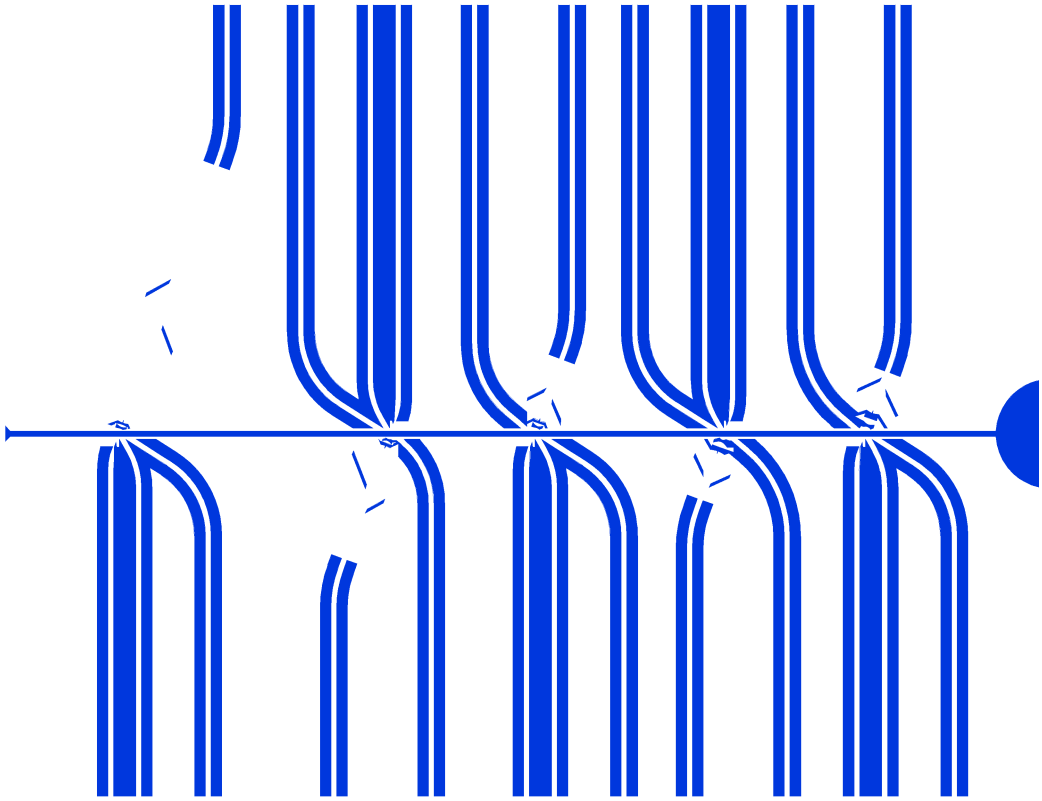

FIGURE B.4: Device 4 of the mask for PL procedure of the SU-8 device, in which the incident angle of each beam is 20° relative to the normal of the microfluidic channel and a notch is added onto the first lens for on-chip detection of forward scattered light.

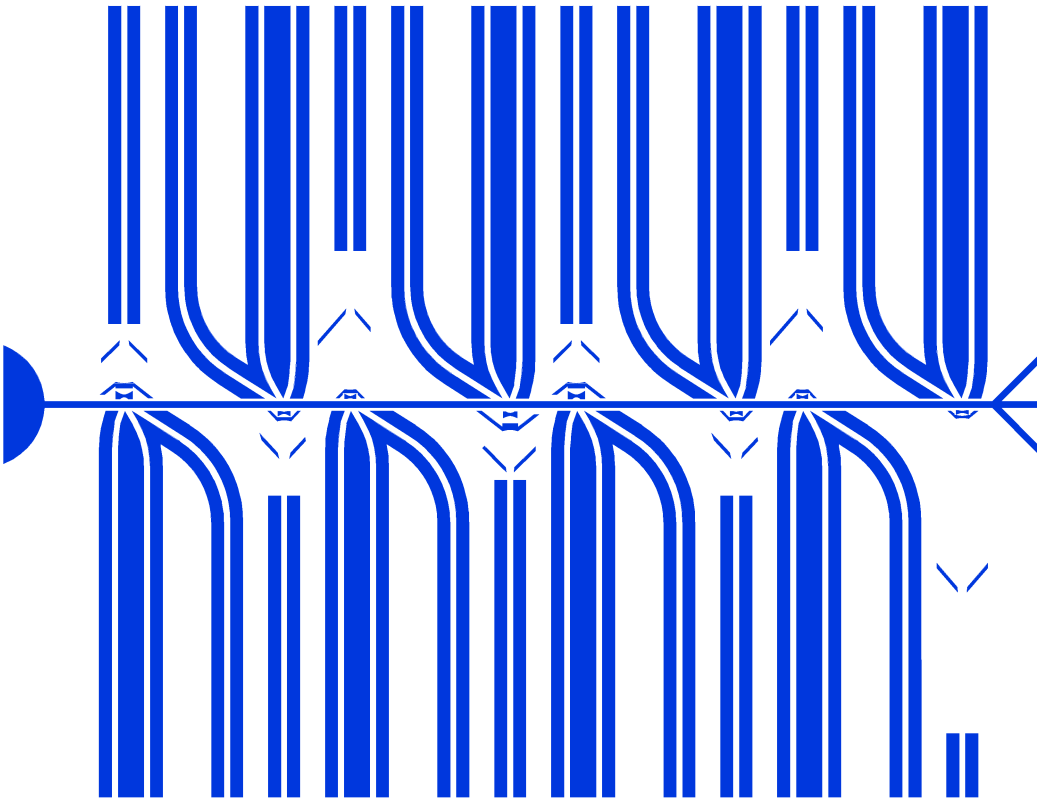

FIGURE B.5: Device 5 of the mask for PL procedure of the SU-8 device, in which all the illumination beams are normally incident to the microfluidic channel.

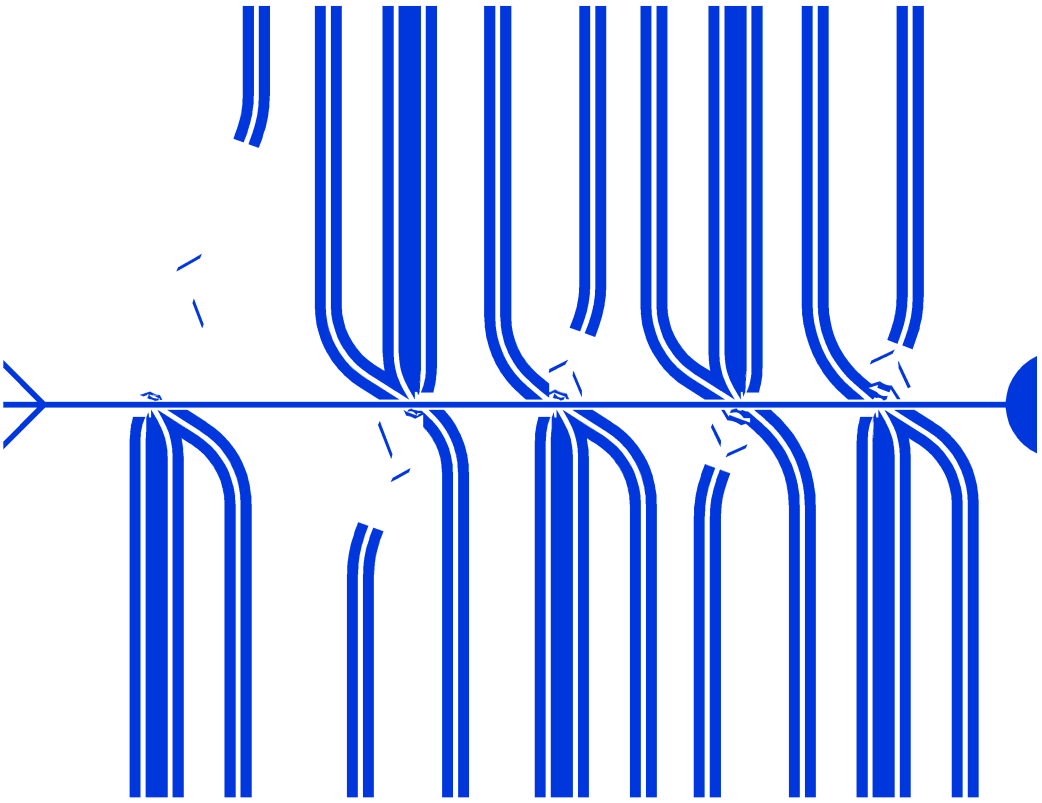

FIGURE B.6: Device 6 of the mask for PL procedure of the SU-8 device, in which the incident angle of each beam is 20° relative to the normal of the microfluidic channel.

# Appendix C

# MATLAB codes

### Gaussian function construction

```
function [ expr, coeff ] = gauss(ord)

% GAUSS construct ord-th summation of gaussian functions

% Check arguments
if nargin > 1 || ord < 1 || ord > 99
    error('gauss:NotCorrectInputArguments','Not correct input arguments');
end

% Construct expression
coeff = cell(ord, 3);
gauss_fun = cell(ord, 1);
for n = 1:ord
    if n<10
        coeff{n, 1} = [ 'a0', int2str(n) ];
        coeff{n, 2} = [ 'b0', int2str(n) ];
        coeff{n, 3} = [ 'c0', int2str(n) ];
    else
        coeff{n, 1} = [ 'a', int2str(n) ];
        coeff{n, 2} = [ 'b', int2str(n) ];
        coeff{n, 3} = [ 'c', int2str(n) ];
    end
    gauss_fun{n, 1} = [ coeff{n, 1}, '*exp(', '-((x-', coeff{n, 2}, ')/', ...
     coeff{n, 3}, ')^2)' ];
end
expr = gauss_fun{ord, 1};
n = ord - 1;
while n
    expr = strcat( gauss_fun{n, 1}, '+', expr );
    n = n - 1;
end
```

### Curve fitting with Gaussian function

```
function [ cfun gof ] = mgfit(k, E)

E_residual = E;
ord = 1;
peaks = [];
coeff_lower = [];
coeff_upper = [];
coeff_start = [];
fit_rsquare = 0;
fit_rsquare_goal = 0.9999;
tic;
while fit_rsquare < fit_rsquare_goal && ord <= 99
    [ peak_y, peak_ind ] = max(E_residual);
    peak_x = k(peak_ind);
    peaks = [ peaks, peak_x ];
    ord = length(peaks);
    [ fun_expr, coeff ] = gauss(ord);
    fitting_fun = fittype(fun_expr);
    coeff_lower = [ coeff_lower; 0, k(1), 0 ];
    coeff_upper = [ coeff_upper; max(E), k(end), k(end)-k(1) ];
    coeff_start = [ coeff_start; peak_y, peak_x, 1 ];
    fitting_option = fitoptions('Method','NonlinearLeastSquares', ...
                                'Lower', coeff_lower(:), ...
                                'Upper', coeff_upper(:), ...
                                'Startpoint', coeff_start(:));
    [cfun, gof] = fit( k, E(:, 1), fitting_fun, fitting_option );
    disp(ord);
    disp(gof);
    coeff_val = coeffvalues(cfun);
    coeff_start = reshape(coeff_val, [], 3);
    E_residual = E - cfun(k);
    fit_rsquare = gof.rsquare;
    ord = ord + 1;
end
toc;
```

### Principal component analysis

```
%% PCA

load IR_spectra_9_strains_mgfit.mat;


B = A(3:end, :);
for i = 1:n_spectra
    B(:, i) = diff( cfun{i}(k), 2 );
end

C = B';
[coeff,score,latent,tsquared,explained,mu] = pca(C);

legend_str = {'E. coli MG1655', 'E. coli HS2210', 'A. jandaei', ...
              'A. media','Ent. casseliflavus', 'Ent. durans', ...
              'Ent. gallinarum', 'Ent. hirae', 'Ent. saccharolyticus'};
color_str = { 'b', 'r', 'b', 'r', 'b', 'r', 'm', 'g', 'k' };
marker_str = { 'o', 'o', '+', '+', 'd', 'd', 'd', 'd', 'd' };
markeredgecolor_str = { 'b', 'r', 'b', 'r', 'b', 'r', 'm', 'g', 'k' };

fig3 = figure( 'OuterPosition', get( 0, 'ScreenSize' ) );
figure4thesis( fig3, 6, 5 );
s(1) = axes( 'Position', [ 0.125 0.4 0.5 0.6] );
for i = 1:n_spectra
    scatter3( score(i, 1), score(i, 2), score(i, 3), ...
        'Marker', marker_str{ceil(i/8)}, ...
        'MarkerEdgeColor', markeredgecolor_str{ceil(i/8)} );
    hold on;
end
xlabel( 'Score 1', 'Position', [-0.02, -0.09, -0.04], 'Rotation', 20 );
ylabel( 'Score 2', 'Position', [-0.08, 0, -0.04], 'Rotation', -33 );
zlabel( 'Score 3' );
text( 'Units', 'normalized', 'Position', [0.01, 0.8], 'String', '(a)', ...
      'VerticalAlignment', 'top' );

s(5) = axes( 'Position', [ 0.8 0.6 0.1 0.1], 'Visible', 'off' );
for i = 1:length(strain)
    scatter( score((i-1)*8+1, 1), score((i-1)*8+1, 1), ...
        'Marker', marker_str{i}, 'MarkerEdgeColor', markeredgecolor_str{i} );
    hold on;
end
h = legend(legend_str, 'Location', 'eastoutside');
set( h, 'Position', [ 0.7 0.5 0.275 0.4] );

s(2) = axes( 'Position', [ 0.08 0.08 0.24 0.24] );
for i = 1:n_spectra
    scatter( score(i, 1), score(i, 2), 'Marker', marker_str{ceil(i/8)}, ...
             'MarkerEdgeColor', markeredgecolor_str{ceil(i/8)} );
    hold on;
```

```
end
xlim( [-0.05 0.05] );
ylim( [-0.05, 0.1] );

E_coli_score1_mean = mean( score(1:16, 1) );
E_coli_score1_std = std( score(1:16, 1) );
A_E_score1_mean = mean( score(17:end, 1) );
A_E_score1_std = std( score(17:end, 1) );
score1_sep = ( E_coli_score1_mean + E_coli_score1_std + A_E_score1_mean ...
               - A_E_score1_std ) / 2;
plot( [1; 1] * score1_sep, [-0.05; 0.1], 'k--' );

MG_score2_mean = mean( score(1:8, 2) );
MG_score2_std = std( score(1:8, 2) );
HS_score2_mean = mean( score(9:16, 2) );
HS_score2_std = std( score(9:16, 2) );
score2_sep = ( MG_score2_mean - MG_score2_std + HS_score2_mean ...
               + HS_score2_std ) / 2;
plot( [-0.05; score1_sep], [1; 1] * score2_sep, 'k--' );

xlabel( 'Score 1' );
ylabel( 'Score 2' );
text( 'Units', 'normalized', 'Position', [0.01, 1], 'String', '(b)',  ...
      'VerticalAlignment', 'top' );
s(3) = axes( 'Position', [ 0.4133 0.08 0.24 0.24] );
for i = 1:n_spectra
    scatter( score(i, 1), score(i, 3), 'Marker', marker_str{ceil(i/8)}, ...
             'MarkerEdgeColor', markeredgecolor_str{ceil(i/8)} );
    hold on;
end
xlim( [-0.05 0.05] );
ylim( [-0.04, 0.04] );
A_score3_mean = mean( score(17:32, 3) );
A_score3_std = std( score(17:32, 3) );
Ent_score3_mean = mean( score(33:end, 3) );
Ent_score3_std = std( score(33:end, 3) );
score3_sep = ( A_score3_mean - 2 * A_score3_std + Ent_score3_mean ...
               + 2 * Ent_score3_std ) / 2;
plot( [1; 1] * score1_sep, [-0.04; 0.04], 'k--' );
plot( [score1_sep; 0.05], [1;1] * score3_sep, 'k--' );

xlabel( 'Score 1' );
ylabel( 'Score 3' );
text( 'Units', 'normalized', 'Position', [0.01, 1], 'String', '(c)',  ...
      'VerticalAlignment', 'top' );

s(4) = axes( 'Position', [ 0.7467 0.08 0.24 0.24] );
for i = 1:n_spectra
    scatter( score(i, 2), score(i, 3), 'Marker', marker_str{ceil(i/8)}, ...
             'MarkerEdgeColor', markeredgecolor_str{ceil(i/8)} );
    hold on;
```

```
end
xlabel( 'Score 2' );
ylabel( 'Score 3' );
text( 'Units', 'normalized', 'Position', [0.01, 1], 'String', '(d)', ...
      'VerticalAlignment', 'top' );



hs = findobj( 'Type', 'scatter' );
set( hs, 'LineWidth', 1 );
```

### Determine pulse amplitude and transit time

```
function  peak = FindPeak( intensity, sampling_freq )
%UNTITLED Summary of this function goes here
%   Detailed explanation goes here

peak = struct('height', [], 'width', [], 'index', [], 'baseline', [], ...
'threshold', []);

[ baseline, threshold ] = FindBaselineThreshold( intensity );
dt = 1/sampling_freq;

I = intensity - baseline;
index = find(I > threshold);
N = length( I );
n = length( index );

if n == 0           % No peak found
    peak = [];
    return;
elseif n == 1               % 1 single point peak found
    peak.height = I(index);
    peak.index = index;
    if index == 1           % first data point
        peak.width = (I(index) - threshold) * (1 / I(index) + 1 / ...
        (I(index)-I(index+1)));
    elseif index == N       % last data point
        peak.width = (I(index) - threshold) * (1 / (I(index)-I(index-1)) ...
        + 1 / I(index));
    else
        peak.width = (I(index) - threshold) * (1 / (I(index)-I(index-1)) ...
        + 1 / (I(index)-I(index+1)));
    end
    peak.width = peak.width * dt;
    peak.baseline = baseline;
    peak.threshold = threshold;
    return;
else                 % 1 peak with multiple points or more peaks found
    peak_count = 1;
    peak_index = zeros(n, 2);
    peak_index(1, :) = [index(1), index(1)];
    for i = 1:n-1
        if index(i+1) == index(i) + 1
            peak_index(peak_count, 2) = index(i+1);
        else
            peak_count = peak_count + 1;
            peak_index(peak_count, :) = index(i+1) * [1, 1];
        end
    end
    peak_index(peak_count+1:end, :) = [];
    %% calculate widths of all peaks
```

```
    for i = 1:peak_count
        if peak_index(i, 1) == 1 && peak_index(i, 2) == N
            peak(i, 1).width = peak_index(i, 2) - peak_index(i, 1) ...
                             + 1 - threshold / I(1) ...
                             + 1 - threshold / I(N);
        elseif peak_index(i, 1) == 1 && peak_index(i, 2) ~= N
            peak(i, 1).width = peak_index(i, 2) - peak_index(i, 1) ...
                             + 1 - threshold / I(1) ...
                             + (I(peak_index(i, 2)) - threshold) / ...
                             (I(peak_index(i, 2))-I(peak_index(i, 2)+1));
        elseif peak_index(i, 1) ~= 1 && peak_index(i, 2) == N
            peak(i, 1).width = peak_index(i, 2) - peak_index(i, 1) ...
                             + (I(peak_index(i, 1)) - threshold) / ...
                             (I(peak_index(i, 1))-I(peak_index(i, 1)-1)) ...
                             + 1 - threshold / I(N);
        else
            peak(i, 1).width = peak_index(i, 2) - peak_index(i, 1) ...
                             + (I(peak_index(i, 1)) - threshold) / ...
                             (I(peak_index(i, 1))-I(peak_index(i, 1)-1)) ...
                             + (I(peak_index(i, 2)) - threshold) / ...
                             (I(peak_index(i, 2))-I(peak_index(i, 2)+1));
        end
        peak(i, 1).width = peak(i, 1).width * dt;
    end
    %% find index of peak heights
    for i=1:peak_count
        if peak_index(i, 1) ~= peak_index(i, 2)
            single_peak = I(peak_index(i, 1):peak_index(i, 2));
            [~, ind_peak] = max(single_peak);
            peak_index(i, 1) = peak_index(i, 1) + ind_peak - 1;
        end
        peak(i, 1).index = peak_index(i, 1);
        peak(i, 1).height = I( peak_index(i, 1) );
        peak(i, 1).baseline = baseline;
        peak(i, 1).threshold = threshold;
    end
end
```

### Determine the baseline and threshold

```
function [ baseline, threshold ] = FindBaselineThreshold( intensity )

mu = mean( intensity );
sigma = std( intensity );
indx = intensity < mu + 4 * sigma & intensity > mu - 4 * sigma;
% [ n, x ] = hist( intensity(indx), ceil(range(intensity(indx))/...
std(intensity(indx))*3) );
% y = fit( x', n', 'gauss1');
% baseline = y.b1;
% threshold = 4 * y.c1 / sqrt(2);
intensity1 = intensity( indx );
mu1 = mean( intensity1 );
sigma1 = std( intensity1 );
indx1 = intensity1 < mu1 + 4 * sigma1 & intensity1 > mu1 - 4 * sigma1;
baseline = mean( intensity(indx1) );
threshold = 4 * std( intensity(indx1) );
```

### Convert structure array to matrix

```
function peak_mat = Peak2Mat( peak )
%Peak2Mat convert structure array, peak, to matrix with each column corresponding
%to each field in peak

[ m, n ] = size( peak );

if m * n == 0
    peak_mat = [];
else
    names = fieldnames( peak );
    p = size( names, 1 );
    peak_mat = zeros(m, p);
    for i = 1:p
        peak_mat(:, i) = [ peak.(names{i}) ]';
    end
end

end
```

# Bibliography


[1] William R Mac Kenzie, Neil J Hoxie, Mary E Proctor, M Stephen Gradus, Kathleen A Blair, Dan E Peterson, James J Kazmierczak, David G Addiss, Kim R Fox, Joan B Rose, and Jeffrey P Davis. A Massive Outbreak in Milwaukee of Cryptosporidium Infection Transmitted through the Public Water Supply. *N. Engl. J. Med.*, 331(3):161–167, 1994.

[2] Justice Dennis O'Connor. Report of the Walkerton Inquiry: The events of May 2000 and related issues. Part 1: A summary. Technical report, Ontario Ministry of the Attorney General, Toronto, Ontario, 2002.

[3] Kelly A Reynolds, Kristina D Mena, and Charles P Gerba. Risk of Waterborne Illness Via Drinking Water in the United States. *Rev Env. Contam Toxicol*, 192:117–158, 2008.

[4] Li Liu, Hope L Johnson, Simon Cousens, Jamie Perin, Susana Scott, Joy E Lawn, Igor Rudan, Harry Campbell, Richard Cibulskis, Mengying Li, Colin Mathers, and Robert E Black. Global, regional, and national causes of child mortality: an updated systematic analysis for 2010 with time trends since 2000. *Lancet*, 379(9832):2151–61, 2012.

[5] Helen Bridle, Brian Miller, and Marc P Y Desmulliez. Application of microfluidics in waterborne pathogen monitoring: A review. *Water Res.*, 55(0):256–271, 2014.

[6] Phaedra S Corso, Michael H Kramer, Kathleen A Blair, David G Addiss, Jeffrey P Davis, and Anne C Haddix. Costs of Illness in the 1993 Waterborne Cryptosporidium Outbreak, Milwaukee, Wisconsin. *Emerg. Infect. Dis. J.*, 9(4):426, 2003.

[7] Timothy M Straub and Darrell P Chandler. Towards a unified system for detecting waterborne pathogens. *J. Microbiol. Methods*, 53(2):185–197, 2003.

[8] *Guideline for drinking-water quality*. World Health Organization, 4 edition, 2011.

[9] Annie Rompré, Pierre Servais, Julia Baudart, Marie-Renée De-Roubin, and Patrick Laurent. Detection and enumeration of coliforms in drinking water: current methods and emerging approaches. *J. Microbiol. Methods*, 49(1):31–54, 2002.

[10] Pam Tallon, Brenda Magajna, Cassandra Lofranco, and Kam Tin Leung. Microbial Indicators of Faecal Contamination in Water: A Current Perspective. *Water. Air. Soil Pollut.*, 166(1-4): 139–166, 2005.

[11] APHA, AWWA, and WEF. *Standard Methods for the Examination of Water and Wastewater*. American Public Health Association, Washington, 22nd edition, 2012.

[12] P H Mäkelä and H Mayer. Enterobacterial common antigen. *Bacteriol. Rev.*, 40(3):591–632, 1976.

[13] Abul K Abbas. *Basic immunology : functions and disorders of the immune system*. Elsevier, St. Louis, Mo., fifth edition, 2016.

[14] I Hübner, I Steinmetz, U Obst, D Giebel, and D Bitter-Suermann. Rapid determination of members of the family Enterobacteriaceae in drinking water by an immunological assay using a monoclonal antibody against enterobacterial common antigen. *Appl. Envir. Microbiol.*, 58 (9):3187–3191, 1992.

[15] Renata Zaccone, Ermanno Crisafi, and Gabriella Caruso. Evaluation of fecal pollution in coastal Italian waters by immunofluorescence. *Aquat. Microb. Ecol.*, 9(1):79–85, 1995.

[16] G Caruso, F De Pasquale, M Mancuso, D Zampino, and E Crisafi. Fluorescent Antibody-Viability Staining and $\beta$-Glucuronidase Assay as Rapid Methods for Monitoring Escherichia coli Viability in Coastal Marine Waters. *J. Immunoass. Immunochem.*, 27(1):1–13, 2006.

[17] R Kfir and B Genthe. Advantages and Disadvantages of the Use of Immunodetection Techniques for the Enumeration of Microorganisms and Toxins in Water. *Water Sci. Technol.*, 27 (3-4):243–252, 1993.

[18] A K Bej, R J Steffan, J DiCesare, L Haff, and R M Atlas. Detection of coliform bacteria in water by polymerase chain reaction and gene probes. *Appl. Envir. Microbiol.*, 56(2):307–314, 1990.

[19] A K Bej, M H Mahbubani, J L Dicesare, and R M Atlas. Polymerase chain reaction-gene probe detection of microorganisms by using filter-concentrated samples. *Appl. Envir. Microbiol.*, 57 (12):3529–3534, 1991.

[20] A K Bej, S C McCarty, and R M Atlas. Detection of coliform bacteria and Escherichia coli by multiplex polymerase chain reaction: comparison with defined substrate and plating methods for water quality monitoring. *Appl. Envir. Microbiol.*, 57(8):2429–2432, 1991.

[21] E.J. Fricker and C.R. Fricker. Application of the polymerase chain reaction to the identification of Escherichia coli and coliforms in water. *Lett. Appl. Microbiol.*, 19(1):44–46, 1994.

[22] David Juck, Jordan Ingram, Michèle Prévost, Josée Coallier, and Charles Greer. Nested PCR protocol for the rapid detection of Escherichia coli in potable water. *Can. J. Microbiol.*, 42 (8):862–866, 1996.

[23] S Iqbal, J Robinson, D Deere, J. R Saunders, C Edwards, and J Porter. Efficiency of the polymerase chain reaction amplification of the uid gene for detection of Escherichia coli in contaminated water. *Lett. Appl. Microbiol.*, 24(6):498 – 502, 1997.

[24] Tarja Pitkänen. Review of Campylobacter spp. in drinking and environmental waters. *J. Microbiol. Methods*, 95(1):39–47, 2013.

[25] Diana Mendes Silva and Lucília Domingues. On the track for an efficient detection of Escherichia coli in water: A review on PCR-based methods. *Ecotoxicol. Environ. Saf.*, 113: 400–411, 2015.

[26] Eva Theres Gensberger, Angela Sessitsch, and Tanja Kostić. Propidium monoazide-quantitative polymerase chain reaction for viable Escherichia coli and Pseudomonas aeruginosa detection from abundant background microflora. *Anal. Biochem.*, 441(1):69–72, 2013.

[27] Rosina Girones, Maria Antonia Ferrús, José Luis Alonso, Jesus Rodriguez-Manzano, Byron Calgua, Adriana de Abreu Corrêa, Ayalkibet Hundesa, Anna Carratala, and Sílvia Bofill-Mas. Molecular detection of pathogens in water–the pros and cons of molecular techniques. *Water Res.*, 44(15):4325–39, 2010.

[28] Hyatt C Green and Katharine G Field. Sensitive detection of sample interference in environmental qPCR. *Water Res.*, 46(10):3251–60, 2012.

[29] Andrée F Maheux, Luc Bissonnette, and Michel G Bergeron. Rapid detection of the Escherichia coli genospecies in water by conventional and real-time PCR. *Methods Mol. Biol.*, 943:289–305, 2013.

[30] Surafel Mulugeta, Ryan Hindman, Adam M Olszewski, Kaitlyn Hoover, Kendall Greene, Matthew Lieberman, and Steven A Mauro. Contamination level and location of recreational freshwater influence the ability to predict Escherichia coli concentration by qPCR targeting Bacteroides. *J. Environ. Manage.*, 103:95–101, 2012.

[31] S Ram, P Vajpayee, P D Dwivedi, and R Shanker. Culture-free detection and enumeration of STEC in water. *Ecotoxicol. Environ. Saf.*, 74(4):551–7, 2011.

[32] A Schriewer, A Wehlmann, and S Wuertz. Improving qPCR efficiency in environmental samples by selective removal of humic acids with DAX-8. *J. Microbiol. Methods*, 85(1):16–21, 2011.

[33] M Wagner, R Amann, H Lemmer, and K H Schleifer. Probing activated sludge with oligonucleotides specific for proteobacteria: inadequacy of culture-dependent methods for describing microbial community structure. *Appl. Envir. Microbiol.*, 59(5):1520–1525, 1993.

[34] Rudolf I Amann, Wolfgang Ludwig, and Karl-Heinz Schleifer. Phylogenetic Identification and In Situ Detection of Individual Microbial Cells without Cultivation. *Microbiol. Rev.*, 59(1): 143, 1995.

[35] M.W Mittelman, M Habash, J.-M Lacroix, A.E Khoury, and M Krajden. Rapid detection of Enterobacteriaceae in urine by fluorescent 16S rRNA in situ hybridization on membrane filters. *J. Microbiol. Methods*, 30(2):153–160, 1997.

[36] Frank J Loge, Robert W Emerick, Donald E Thompson, Douglas C Nelson, and Jeannie L Darby. Development of a Fluorescent 16S rRNA Oligonucleotide Probe Specific to the Family Enterobacteriaceae. *Water Environ. Res.*, 71(1):75–83, 1999.

[37] L K Poulsen, F Lan, C S Kristensen, P Hobolth, S Molin, and K A Krogfelt. Spatial distribution of Escherichia coli in the mouse large intestine inferred from rRNA in situ hybridization. *Infect. Immun.*, 62(11):5191–5194, 1994.

[38] Béatrice Regnault, Sylvie Martin-Delautre, Monique Lejay-Collin, Martine Lefèvre, and Patrick A.D. Grimont. Oligonucleotide probe for the visualization of Escherichiacoli/Escherichia fergusonii cells by in situ hybridization:specificity and potential applications. *Res. Microbiol.*, 151(7):521–533, 2000.

[39] J. Baudart and P. Lebaron. Rapid detection of Escherichia coli in waters using fluorescent in situ hybridization, direct viable counting and solid phase cytometry. *J. Appl. Microbiol.*, 109 (4):1253 – 1264, 2010.

[40] D P McGregor, S Forster, J Steven, J Adair, S E Leary, D L Leslie, W J Harris, and R W Titball. Simultaneous detection of microorganisms in soil suspension based on PCR amplification of bacterial 16S rRNA fragments. *Biotechniques*, 21(3):463–6, 468, 470–1, 1996.

[41] G. J. Jansen, M. Mooibroek, J. Idema, H. J. M. Harmsen, G. W. Welling, and J. E. Degener. Rapid Identification of Bacteria in Blood Cultures by Using Fluorescently Labeled Oligonucleotide Probes. *J. Clin. Microbiol.*, 38(2):814–817, 2000.

[42] A M Prescott and C R Fricker. Use of PNA oligonucleotides for the in situ detection of Escherichia coli in water. *Mol. Cell. Probes*, 13(4):261–268, 1999.

[43] P Lebaron, P Catala, C Fajon, F Joux, J Baudart, and L Bernard. A New Sensitive, Whole-Cell Hybridization Technique for Detection of Bacteria Involving a Biotinylated Oligonucleotide Probe Targeting rRNA and Tyramide Signal Amplification. *Appl. Envir. Microbiol.*, 63(8): 3274–3278, 1997.

[44] D Naumann, D Helm, and H Labischinski. Microbiological characterizations by FT-IR spectroscopy. *Nature*, 351(6321):81–82, 1991.

[45] L C Thomas and J E S Greenstreet. The identification of micro-organisms by infrared spectrophotometry. *Spectrochim. Acta*, 6(4):302–319, 1954.

[46] Jackson W Riddle, Paul W Kabler, Bernard A Kenner, Robert H Bordner, Sue W Rockwood, and Heber J R Stevenson. Bacterial Identification by Infrared Spectrophotometry. *J. Bacteriol.*, 72(5):593–603, 1956.

[47] J D S Goulden and M Elisabeth Sharpe. The Infra-Red Absorption Spectra of Lactobacilli. *J. Gen. Microbiol.*, 19(1):76–86, 1958.

[48] K P Norris. Infra-Red Spectroscopy and Its Application to Microbiology. *J. Hyg. (Lond).*, 57 (3):326–345, 1959.

[49] A W Scopes. The Infrared Spectra of Some Acetic Acid Bacteria. *J. Gen. Microbiol.*, 28(1): 69–79, 1962.

[50] Kenzo Nakamura, D N Ostrovsky, Tatsuo Miyazawa, and Shoji Mizushima. Infrared spectra of outer and cytoplasmic membranes of Escherichia coli. *Biochim. Biophys. Acta - Biomembr.*, 332(3):329–335, 1974.

[51] L Mariey, J P Signolle, C Amiel, and J Travert. Discrimination, classification, identification of microorganisms using FTIR spectroscopy and chemometrics. *Vib. Spectrosc.*, 26(2):151–159, 2001.

[52] Michael Beekes, Peter Lasch, and Dieter Naumann. Analytical applications of Fourier transform-infrared (FT-IR) spectroscopy in microbiology and prion research. *Vet. Microbiol.*, 123(4):305–319, 2007.

[53] A Alvarez-Ordóñez, D J M Mouwen, M López, and M Prieto. Fourier transform infrared spectroscopy as a tool to characterize molecular composition and stress response in foodborne pathogenic bacteria. *J. Microbiol. Methods*, 84(3):369–378, 2011.

[54] Jun Wang, Kyung Ho Kim, Sungkyun Kim, Yong Soo Kim, Qing X Li, and Soojin Jun. Simple quantitative analysis of Escherichia coli K-12 internalized in baby spinach using Fourier Transform Infrared spectroscopy. *Int. J. Food Microbiol.*, 144(1):147–151, 2010.

[55] Xiaonan Lu, Qian Liu, Di Wu, Hamzah M Al-Qadiri, Nivin I Al-Alami, Dong-Hyun Kang, Joong-Han Shin, Juming Tang, Jamie M F Jabal, Eric D Aston, and Barbara A Rasco. Using of infrared spectroscopy to study the survival and injury of Escherichia coli O157:H7, Campylobacter jejuni and Pseudomonas aeruginosa under cold stress in low nutrient media. *Food Microbiol.*, 28(3):537–546, 2011.

[56] Jürgen Schmitt and Hans-Curt Flemming. FTIR-spectroscopy in microbial and material analysis. *Int. Biodeterior. Biodegradation*, 41(1):1–11, 1998.

[57] Denise L Doak and Janice A Phillips. In Situ Monitoring of an Escherichia coli Fermentation Using a Diamond Composition ATR Probe and Mid-infrared Spectroscopy. *Biotechnol. Prog.*, 15(3):529–539, 1999.

[58] Mustafa Kansiz, Philip Heraud, Bayden Wood, Frank Burden, John Beardall, and Don McNaughton. Fourier Transform Infrared microspectroscopy and chemometrics as a tool for the discrimination of cyanobacterial strains. *Phytochemistry*, 52(3):407 – 417, 1999.

[59] Henri Kornmann, Martin Rhiel, Christopher Cannizzaro, Ian Marison, and Urs von Stockar. Methodology for real-time, multianalyte monitoring of fermentations using an in-situ mid-infrared sensor. *Biotechnol. Bioeng.*, 82(6):702–709, 2003.

[60] J. C. Feo, M. A. Castro, L. C. Robles, and A. J. Aller. Fourier-transform infrared spectroscopic study of the interactions of selenium species with living bacterial cells. *Anal. Bioanal. Chem.*, 378(6):1601–1607, 2004.

[61] Mengshi Lin, Murad Al-Holy, Su-Sen Chang, Yiqun Huang, Anna G Cavinato, Dong-Hyun Kang, and Barbara A Rasco. Rapid discrimination of Alicyclobacillus strains in apple juice by Fourier transform infrared spectroscopy. *Int. J. Food Microbiol.*, 105(3):369–376, 2005.

[62] Erik Schleicher, Benedikt Hessling, Viktoria Illarionova, Adelbert Bacher, Stefan Weber, Gerald Richter, and Klaus Gerwert. Light-induced reactions of Escherichia coli DNA photolyase monitored by Fourier transform infrared spectroscopy. *FEBS J.*, 272(8):1855–66, 2005.

[63] Hamzah M Al-Qadiri, Murad A Al-Holy, Mengshi Lin, Nivin I Alami, Anna G Cavinato, and Barbara A Rasco. Rapid Detection and Identification of Pseudomonas aeruginosa and Escherichia coli as Pure and Mixed Cultures in Bottled Drinking Water Using Fourier Transform Infrared Spectroscopy and Multivariate Analysis. *J. Agric. Food Chem.*, 54(16):5749–5754, 2006.

[64] Hamzah M Al-Qadiri, Mengshi Lin, Anna G Cavinato, and Barbara A Rasco. Fourier transform infrared spectroscopy, detection and identification of Escherichia coli O157:H7 and Alicyclobacillus strains in apple juice. *Int. J. Food Microbiol.*, 111(1):73, 2006.

[65] Murad A Al-Holy, Mengshi Lin, Anna G Cavinato, and Barbara A Rasco. The use of Fourier transform infrared spectroscopy to differentiate Escherichia coli O157:H7 from other bacteria inoculated into apple juice. *Food Microbiol.*, 23(2):162–168, 2006.

[66] H Lamprell, G Mazerolles, A Kodjo, J F Chamba, Y Noël, and E Beuvier. Discrimination of Staphylococcus aureus strains from different species of Staphylococcus using Fourier transform infrared (FTIR) spectroscopy. *Int. J. Food Microbiol.*, 108(1):125, 2006.

[67] Chun Hu, Jian Guo, Jiuhui Qu, and Xuexiang Hu. Photocatalytic degradation of pathogenic bacteria with AgI/TiO2 under visible light irradiation. *Langmuir*, 23(9):4982–7, 2007.

[68] Jonas Schenk, Carla Viscasillas, Ian W Marison, and Urs von Stockar. On-line monitoring of nine different batch cultures of E. coli by mid-infrared spectroscopy, using a single spectra library for calibration. *J. Biotechnol.*, 134(1–2):93–102, 2008.

[69] Hamzah M Al-Qadiri, Nivin I Al-Alami, Murad A Al-Holy, and Barbara A Rasco. Using Fourier Transform Infrared (FT-IR) Absorbance Spectroscopy and Multivariate Analysis To Study the Effect of Chlorine-Induced Bacterial Injury in Water. *J. Agric. Food Chem.*, 56(19): 8992–8997, 2008.

[70] Xing Hu, Zunan Qiu, Yerui Wang, Zichao She, Guangren Qian, and Zhongming Ren. Effect of ultra-strong static magnetic field on bacteria: Application of Fourier-transform infrared spectroscopy combined with cluster analysis and deconvolution. *Bioelectromagnetics*, 30(6): 500 – 507, 2009.

[71] Reeta Davis, Joseph Irudayaraj, Bradley L Reuhs, and Lisa J Mauer. Detection of E. coli O157:H7 from Ground Beef Using Fourier Transform Infrared (FT-IR) Spectroscopy and Chemometrics. *J. Food Sci.*, 75(6):M340–M346, 2010.

[72] Stephen P Perfetto, Pratip K Chattopadhyay, and Mario Roederer. Seventeen-colour flow cytometry: unravelling the immune system. *Nat. Rev. Immunol.*, 4(8):648–55, 2004.

[73] ThermoFisher. Introduction to Flow Cytometry, 2016.

[74] K H Seo, R E Brackett, and J F Frank. Rapid detection of Escherichia coli O157:H7 using immuno-magnetic flow cytometry in ground beef, apple juice, and milk. *Int. J. Food Microbiol.*, 44(1-2):115–123, 1998.

[75] Nobuyasu Yamaguchi, Makoto Sasada, Mio Yamanaka, and Masao Nasu. Rapid detection of respiring Escherichia coli O157:H7 in apple juice, milk, and ground beef by flow cytometry. *Cytometry*, 54A(1):27–35, 2003.

[76] R G Clarke and A C Pinder. Improved detection of bacteria by flow cytometry using a combination of antibody and viability markers. *J. Appl. Microbiol.*, 84(4):577–584, 1998.

[77] Thusitha S Gunasekera, Paul V Attfield, and Duncan A Veal. A Flow Cytometry Method for Rapid Detection and Enumeration of Total Bacteria in Milk. *Appl. Environ. Microbiol.*, 66 (3):1228–1232, 2000.

[78] Daniel Hoefel, Warwick L Grooby, Paul T Monis, Stuart Andrews, and Christopher P Saint. Enumeration of water-borne bacteria using viability assays and flow cytometry: a comparison to culture-based techniques. *J. Microbiol. Methods*, 55(3):585–597, 2003.

[79] A S Lepeuple, S Gilouppe, E Pierlot, and M R de Roubin. Rapid and automated detection of fluorescent total bacteria in water samples. *Int. J. Food Microbiol.*, 92(3):327–332, 2004.

[80] F Hammes, M Berney, Y Wang, M Vital, O Koster, and T Egli. Flow-cytometric total bacterial cell counts as a descriptive microbiological parameter for drinking water treatment processes. *Water Res.*, 42(1-2):269–277, 2008.

[81] Michael Berney, Frederik Hammes, Franziska Bosshard, Hans-Ulrich Weilenmann, and Thomas Egli. Assessment and Interpretation of Bacterial Viability by Using the LIVE/DEAD BacLight Kit in Combination with Flow Cytometry. *Appl. Environ. Microbiol.*, 73(10):3283–3290, 2007.

[82] Harald B Steen and Erik Boye. Bacterial growth studied by flow cytometry. *Cytometry*, 1(1): 32–36, 1980.

[83] Christopher E Sims and Nancy L Allbritton. Analysis of single mammalian cells on-chip. *Lab Chip*, 7(4):423–440, 2007.

[84] David P Schrum, Christopher T Culbertson, Stephen C Jacobson, and J Michael Ramsey. Microchip Flow Cytometry Using Electrokinetic Focusing. *Anal. Chem.*, 71(19):4173–4177, 1999.

[85] M J Deen and P K Basu. *Silicon Photonics: Fundamentals and Devices*. Wiley, Chichester, West Sussex, UK ; Hoboken, N.J., 2012.

[86] Klaus B Mogensen, Jamil El-Ali, Anders Wolff, and J\org P Kutter. Integration of Polymer Waveguides for Optical Detection in Microfabricated Chemical Analysis Systems. *Appl.Opt.*, 42(19):4072–4079, 2003.

[87] Suz-Kai Hsiung, Chun-Hong Lee, and Gwo-Bin Lee. Microcapillary electrophoresis chips utilizing controllable micro-lens structures and buried optical fibers for on-line optical detection. *Electrophoresis*, 29(9):1866–1873, 2008.

[88] M Rosenauer and M J Vellekoop. Characterization of a microflow cytometer with an integrated three-dimensional optofluidic lens system. *Biomicrofluidics*, 4(4):43005, 2010.

[89] Matthew J Kennedy, Scott J Stelick, Lavanya G Sayam, Andrew Yen, David Erickson, and Carl A Batt. Hydrodynamic optical alignment for microflow cytometry. *Lab Chip*, 11(6): 1138–1143, 2011.

[90] Maxine A McClain, Christopher T Culbertson, Stephen C Jacobson, and J Michael Ramsey. Flow Cytometry of Escherichia coli on Microfluidic Devices. *Anal. Chem.*, 73(21):5334–5338, 2001.

[91] Canjun Mu, Feiling Zhang, Zhiyi Zhang, Min Lin, and Xudong Cao. Highly efficient dual-channel cytometric-detection of micron-sized particles in microfluidic device. *Sensors & Actuators: B.Chemical*, 151(2):402–409, 2011.

[92] Claire Simonnet and Alex Groisman. High-Throughput and High-Resolution Flow Cytometry in Molded Microfluidic Devices. *Anal. Chem.*, 78(16):5653–5663, 2006.

[93] M Waleed Shinwari, David Zhitomirsky, Imran A Deen, P R Selvaganapathy, M Jamal Deen, and D Landheer. Microfabricated reference electrodes and their biosensing applications. *Sensors (Basel).*, 10(3):1679–715, 2010.

[94] Zhiyun Li, M Jamal Deen, Qiyin Fang, and P R Selvaganapathy. Design of a flat field concave-grating-based micro-Raman spectrometer for environmental applications. *Appl. Opt.*, 51(28): 6855–6863, 2012.

[95] Zhiyun Li, M Jamal Deen, Shiva Kumar, and P Ravi Selvaganapathy. Raman Spectroscopy for In-Line Water Quality Monitoring — Instrumentation and Potential. *Sensors (Basel).*, 14 (9):17275–17303, 2014.

[96] Zhiyun Li and M Jamal Deen. Towards a portable Raman spectrometer using a concave grating and a time-gated CMOS SPAD. *Opt. Express*, 22(15):18736–18747, 2014.

[97] Brian C Smith. *Fundamentals of Fourier transform infrared spectroscopy*. CRC Press, Boca Raton, 1996.

[98] Christian Motzer and Michael Reichling. High resolution study of etch figures on CaF[sub 2] (111). *J. Appl. Phys.*, 105(6):064309, 2009.

[99] Tianyi Guo, M. Jamal Deen, Changqing Xu, Qiyin Fang, P. Ravi Selvaganapathy, and Haiying Zhang. Observation of ultraslow stress release in silicon nitride films on CaF2. *J. Vac. Sci. Technol. A Vacuum, Surfaces, Film.*, 33(4):041515, 2015.

[100] M. W. Moon, K. R. Lee, K. H. Oh, and J. W. Hutchinson. Buckle delamination on patterned substrates. *Acta Mater.*, 52(10):3151–3159, 2004.

[101] A Kinbara, S Baba, N Matuda, and K Takamisawa. Mechanical Properties of and Cracks and Wrinkles in Vacuum-deposited MgF2, Carbon and Boron Coatings. *Thin Solid Films*, 84: 205–212, 1981.

[102] N. Matuda, S. Baba, and A. Kinbara. Internal Stress, Young's Modulus and Adhesion Energy of Carbon Films on Glass Substrates. *Thin Solid Films*, 81:301–305, 1981.

[103] D Nir. Stress Relief Forms of Diamond-like Carbon Thin Films Under Internal Compressive Stress. *Thin Solid Films*, 112:41–49, 1984.

[104] G Gille and B Rau. Buckling Instability and Adhesion of Carbon Layers. *Thin Solid Films*, 120:109–121, 1984.

[105] A. Kinbara and S Baba. Growth process of wrinkles generated in deposited films. *J. Vac. Sci. Technol. A Vacuum, Surfaces, Film.*, 9:2494, 1991.

[106] M. W. Moon, H. M. Jensen, J. W. Hutchinson, K. H. Oh, and A. G. Evans. The characterization of telephone cord buckling of compressed thin films on substrates. *J. Mech. Phys. Solids*, 50(11):2355–2377, 2002.

[107] A Kinbara and S Baba. Internal Stress and Young's Modulus of TiC Coatings. *Thin Solid Films*, 107:359–364, 1983.

[108] C. Kim. Synthesis and structure of ion-beam sputtered multilayer Fe/Ni films. *J. Vac. Sci. Technol. A Vacuum, Surfaces, Film.*, 8(3):1407, 1990.

[109] Jean-Paul Eymery. Observation of Wavy Wrinkles on Stainless Steel Films. *Scr. Metall. Mater.*, 28:633–637, 1993.

[110] K Xiao, Z S Guan, G J Wang, L Jiang, D B Zhu, and Y R Wang. Laser-induced wavy pattern formation in metal thin films. *Appl. Phys. Lett.*, 85(11):1934–1936, 2004.

[111] Ned Bowden, Scott Brittain, Anthony G Evans, John W Hutchinson, and George M Whitesides. Spontaneous formation of ordered structures in thin films of metal supported on an elastomeric polymer. *Nature*, 393:146–149, 1998.

[112] Edwin P. Chan and Alfred J. Crosby. Spontaneous formation of stable aligned wrinkling patterns. *Soft Matter*, 2(4):324, 2006.

[113] Jan Genzer and Jan Groenewold. Soft matter with hard skin: From skin wrinkles to templating and material characterization. *Soft Matter*, 2(4):310, 2006.

[114] Christopher Harrison, Christopher M. Stafford, Wenhua Zhang, and Alamgir Karim. Sinusoidal phase grating created by a tunably buckled surface. *Appl. Phys. Lett.*, 85(18):4016–4018, 2004.

[115] Seok Chung, Jeong Hoon Lee, Myoung-Woon Moon, Jongyoon Han, and Roger D. Kamm. Non-Lithographic Wrinkle Nanochannels for Protein Preconcentration. *Adv. Mater.*, 20(16): 3011–3016, 2008.

[116] Edwin P. Chan, Erica J. Smith, Ryan C. Hayward, and Alfred J. Crosby. Surface wrinkles for smart adhesion. *Adv. Mater.*, 20(4):711–716, 2008.

[117] Malin Kölhed, Peter Hinsmann, Peter Svasek, Johannes Frank, Bo Karlberg, and Bernhard Lendl. On-Line Fourier Transform Infrared Detection in Capillary Electrophoresis. *Anal.*

*Chem.*, 74:3843–3848, 2002.

[118] Malin Kölhed, Peter Hinsmann, Bernhard Lendl, and Bo Karlberg. Micellar electrokinetic chromatography with on-line Fourier transform infrared detection. *Electrophoresis*, 24:687–692, 2003.

[119] Tao Pan, Ryan T. Kelly, Matthew C. Asplund, and Adam T. Woolley. Fabrication of calcium fluoride capillary electrophoresis microdevices for on-chip infrared detection. *J. Chromatogr. A*, 1027(1-2):231–235, 2004.

[120] P. Svasek, E. Svasek, B. Lendl, and M. Vellekoop. Fabrication of miniaturized fluidic devices using SU-8 based lithography and low temperature wafer bonding. *Sensors Actuators A Phys.*, 115(2-3):591–599, 2004.

[121] Blanca H Lapizco-Encinas, Blake a Simmons, Eric B Cummings, and Yolanda Fintschenko. Insulator-based dielectrophoresis for the selective concentration and separation of live bacteria in water. *Electrophoresis*, 25(10-11):1695–1704, 2004.

[122] Blanca H. Lapizco-Encinas, Rafael V. Davalos, Blake a. Simmons, Eric B. Cummings, and Yolanda Fintschenko. An insulator-based (electrodeless) dielectrophoretic concentrator for microbes in water. *J. Microbiol. Methods*, 62(3 SPEC. ISS.):317–326, 2005.

[123] Michael B. Sano, Roberto C. Gallo-Villanueva, Blanca H. Lapizco-Encinas, and Rafael V. Davalos. Simultaneous electrokinetic flow and dielectrophoretic trapping using perpendicular static and dynamic electric fields. *Microfluid. Nanofluidics*, 15(5):599–609, 2013.

[124] Kang-Cheng Lin and Si-Chen Lee. The structural and optical properties of a-SiNx:H prepared by plasma-enhanced chemical-vapor deposition. *J. Appl. Phys.*, 72(11):5474, 1992.

[125] A. A. Abdallah, D. Kozodaev, P. C P Bouten, J. M J Den Toonder, U. S. Schubert, and G. de With. Buckle morphology of compressed inorganic thin layers on a polymer substrate. *Thin Solid Films*, 503(1-2):167–176, 2006.

[126] Robert C. Cammarata. Surface and interface stress effects in thin films. *Prog. Surf. Sci.*, 46 (1):1–38, 1994.

[127] R. C. Cammarata, T. M. Trimble, and D. J. Srolovitz. Surface stress model for intrinsic stresses in thin films. *J. Mater. Res.*, 15(11):2468–2474, 2000.

[128] Jerrold A. Floro, Eric Chason, Robert C. Cammarata, and David J. Srolovitz. Physical Origins of Intrinsic Stresses in Volmer–Weber Thin Films, 2002. ISSN 0883-7694.

[129] E. Chason, B. W. Sheldon, L. B. Freund, J. A. Floro, and S. J. Hearne. Origin of Compressive Residual Stress in Polycrystalline Thin Films. *Phys. Rev. Lett.*, 88(15):156103, 2002.

[130] Zhiyi Zhang, Ping Zhao, Gaozhi Xiao, Benjamin R Watts, and Changqing Xu. Sealing SU-8 microfluidic channels using PDMS. *Biomicrofluidics*, 5(4):46503, 2011.

[131] B R Watts, T Kowpak, Z Zhang, C Q Xu, and S Zhu. Formation and characterization of an ideal excitation beam geometry in an optofluidic device. *Biomed Opt Express*, 1(3):848–860, 2010.

[132] Benjamin R Watts, Thomas Kowpak, Zhiyi Zhang, Chang-Qing Xu, and Shiping Zhu. Formation of bowtie-shaped excitation in a photonic-microfluidic integrated devices. *Microw. Opt. Technol. Lett.*, 53(11):2583–2586, 2011.

[133] Tianyi Guo, M. Jamal Deen, Changqing Xu, Qiyin Fang, P. Ravi Selvaganapathy, and Haiying Zhang. A High-accuracy Micro-flow Cytometer for Low Concentration Applications. *Submitt. to Sci. Reports*, 2016.

[134] J Lee, R A Deininger, and R M Fleece. Rapid determination of bacteria in pools. *J. Environ. Health*, 64(1):9–14, 2001.

[135] Jinyang Chung, Joon Sang Kang, Jong Soo Jurng, Jae Hee Jung, and Byoung Chan Kim. Fast

and continuous microorganism detection using aptamer-conjugated fluorescent nanoparticles on an optofluidic platform. *Biosens. Bioelectron.*, 67:303–308, 2015.

[136] J.P. Golden. Automated processing integrated with a microflow cytometer for pathogen detection in clinical matrices. *Biosens. Bioelectron.*, 40(1):10 – 16, 2013.

[137] Nobuyasu Yamaguchi, Masashi Torii, Yuko Uebayashi, and Masao Nasu. Rapid, semiautomated quantification of bacterial cells in freshwater by using a microfluidic device for on-chip staining and counting. *Appl. Environ. Microbiol.*, 77(4):1536–9, 2011.

[138] Tianyi Guo, Yin Wei, Changqing Xu, Benjamin R Watts, Zhiyi Zhang, Qiyin Fang, Haiying Zhang, P Ravi Selvaganapathy, and M Jamal Deen. Counting of Escherichia coli by a microflow cytometer based on a photonic-microfluidic integrated device. *Electrophoresis*, 36(2):298–304, 2015.

[139] Stanley G Schultz, Wolfgang Epstein, and A K Solomon. Cation Transport in Escherichia coli: IV. Kinetics of net K uptake. *J. Gen. Physiol.*, 1963.

[140] H E Kubitschek. Cell volume increase in Escherichia coli after shifts to richer media. *J. Bacteriol.*, 1990.

[141] M M R Howlader, P R Selvaganapathy, M J Deen, and T Suga. Nanobonding Technology Toward Electronic, Fluidic, and Photonic Systems Integration. *Sel. Top. Quantum Electron. IEEE J.*, 17(3):689–703, 2011.